Universidad de Valparaíso
Facultad de Ciencias
Instituto de Física y Astronomía

A momentum coupling between dark matter and dark energy:

consequences at small scales

Tesis para Optar al Grado de Magister en Astrofísica

Daniela Fernanda Palma Palma

Profesor Guía:
Graeme Candlish

Miembros de la Comisión:
Víctor Cárdenas
Nelson Padilla

Valparaíso, Chile
Mayo, 2021

Contents

List of Figures

List of Tables

Acknowledgements

Firstly, I would like to thank my guiding teacher Graeme Candlish for allowing me to carry out this research with him. Thank you for your dedication and patience in carrying out this project. It was definitely a very good experience to have chosen him.

I appreciate all the discussions and suggestions that came out of the Valparaíso Computational Astrophysics (VACA) group and the meetings with friends made in the pandemic, to keep talking about science even when confined. I especially thank Catalina, Greco, Javier, Nicolás, and Felipe for their advice which helped me to finish this thesis.

I also thank Danilo, Erick, Alejandra, Ramses and Domingo, who accompanied me and showed me a great part of Valparaíso, without any doubt, I will take with me beautiful memories of my stay in the port.

I thank my friends from Concepción, with whom I started my first stage in this long road. To Monserrat, Paulo, Ignacio and Carolina, thank you very much for the love and good memories I have with you. Undoubtedly, you were and continue to be an important part of my career, with whom I began to learn not only in the academic field but also to allow me to trust in my abilities. I am sure that wherever we go, we will continue to meet again in the world of science.

I want to thank Alejandro for appearing in my life right at the beginning of this stage, who accompanied me until the end. Thank you for your words and for being present even in my moments of maximum stress. Your unconditional support and your unexpected visits were many times a lifesaver in this process.

And finally, I want to thank my family, who have trusted me from day one and have always motivated me to follow my interests. To my grandmother, my mother and my siblings, whom I love with all my heart. Thank you for allowing me to continue forward.

Abstract

Dark energy is frequently modelled as an additional dynamical scalar field component in the Universe, referred to as "quintessence," which drives the late-time acceleration. Furthermore, the quintessence field may be coupled to dark matter and/or baryons, leading to a fifth force. In this thesis we explore the consequences for non-linear cosmological structure formation arising from a momentum coupling between the quintessence field and dark matter. The coupling leads to a modified Euler equation, which we implement in an N-body cosmological simulation. We then analyse the non-linear power spectrum, comparing with the standard ΛCDM cosmology, as well as the halo mass function, and various other dark matter halo properties. We find that, for certain quintessence potentials, a positive coupling leads to a large enhancement of structure formation at small scales.

Chapter 1

Introduction

1.1 The standard model of cosmology

The General Theory of Relativity, postulated in 1915 by Albert Einstein [27], introduced the Einstein field equations, which describe gravity in terms of spacetime curved by matter and energy. The solution to these equations gives us information about the evolution of our Universe, which, may be static, expanding or contracting. Current observations [4], have corroborated that we live in a spatially flat universe governed by a *cosmological constant* with an accelerated expansion. This constant, named Λ, was introduced into the field equations by Einstein two years after he postulated his theory, in order to accommodate what was believed to be a static Universe [28]. In 1922 Alexander Friedmann used the equations to find a theoretical solution that described an expanding universe, a study that was later carried out independently by Georges Lemaître in 1927. These postulates were finally confirmed by Edwin Hubble two years later [36], confirming the expansion of the Universe, leaving the cosmological constant forgotten for some years.
In 1964, with the discovery of the Cosmic Microwave Background (CMB) [52], the Big Bang model, in which our universe began in an extremely hot and dense state, was universally accepted. The adiabatic expansion cooled the Universe allowing the formation of stars and galaxies by gravitational collapse. This was followed years later by the study of Supernovae Type Ia where it was found that our Universe was expanding at an accelerated rate [54, 59], which was consistent with a solution of the Einstein equations with a cosmological constant. In the standard model of cosmology, this is assumed to be driving the late-time accelerated expansion and is one of the main components in the current standard cosmological model, comprising $\sim 70\%$ of the total matter/energy of the Universe. This component is often referred

to as dark energy (DE). The second most abundant component with $\sim 25\%$ of the total matter/energy is cold dark matter (DM), which is an invisible, pressureless and frictionless form of matter that can be detected only by gravitational effects. Dark matter was indirectly postulated in 1933 by Zwicky [82], who, from the motions of galaxies, discovered that the Coma cluster had a mass about 500 times greater than expected, compared to the amount of visible light emitted. This theoretical proposal was further supported observationally with the study of rotation curves in spiral galaxies by Vera Rubin in the early 1970s. The other $\sim 5\%$ of the matter/energy budget is made up of baryons.

Thus the current standard cosmological model, referred to as ΛCDM, is composed mainly of DE, in the form of a cosmological constant and cold DM, although it does not explain the nature of these components.

1.2 ΛCDM model

Standard cosmological models assume the cosmological principle which postulates at large scales ($\gg 100$ Mpc) the universe is homogeneous and isotropic, as described by the Friedmann-Lemaître-Robertson-Walker (FLRW) metric (we use units of $c = 1$), which is given by

$$ds^2 = g_{\mu\nu}dx^\mu dx^\nu = -dt^2 + a^2(t)d\sigma^2, \tag{1.1}$$

where $g_{\mu\nu}$ is the metric tensor, $a(t)$ is the scale factor in terms of time t, which in terms of the redshift is $a = 1/(1+z)$, and $d\sigma^2$ is the spatial, time-independent metric with curvature constant K:

$$d\sigma^2 = \gamma_{ij}dx^i dx^j = \frac{dr^2}{1 - Kr^2} + r^2(d\theta^2 + \sin^2\theta d\phi^2). \tag{1.2}$$

where K is directly related to the geometry of the Universe, taking values of $K = 1$, -1 or 0, i.e. (spatially) closed, open and flat Universe, respectively. For ΛCDM, observational evidence suggests that we live in a spatially flat Universe, so 1.2 becomes

$$d\sigma^2 = r^2 d\theta^2 + r^2 \sin^2\theta d\phi^2, \tag{1.3}$$

in spherical coordinates.

The coordinates x^i given in 1.2, are *comoving coordinates*, i.e., they are coordinates that follow the expansion flow of the Universe, called Hubble flow. Thus, to obtain the physical coordinates we need to include the scale factor in the comoving coordinates, i.e., $x^i_{phys} = a(t)x^i$, thus

$$v^i_{phys} \equiv v^i_{pec} + Hx^i_{phys} \tag{1.4}$$

where $H \equiv \dot{a}/a$ is the Hubble parameter, v^i_{pec} is peculiar velocity (velocity measured by a comoving observer) and Hx^i_{phys} is the Hubble flow.
To describe the mass/energy of a homogeneous and isotropic Universe, we use perfect fluids which are characterized by their density ρ and pressure p. Thus, the energy momentum tensor for a perfect fluid is

$$T^{\mu}_{\nu} = (\rho + p)u^{\mu}u_{\nu} + p\delta^{\mu}_{\nu}, \tag{1.5}$$

where $u^{\mu} = (-1, 0, 0, 0)$ is the four-velocity in the fluid rest-frame and δ^{μ}_{ν} is the Kronecker delta. Conservation of the total energy-momentum tensor is implied by the Bianchi identity, thus $\nabla_{\mu}T^{\mu}_{\nu} = 0$ which, when substituting (1.5) and considering the FLRW metric, becomes

$$\dot{\rho} + 3\frac{\dot{a}}{a}(\rho + p) = 0, \tag{1.6}$$

which is the *continuity equation*. In the absence of interactions between components (beyond the gravitational) this equation applies separately to each component. With an equation of state to relate the density and pressure, we can determine the evolution of ρ for different components:

$$w = \frac{p}{\rho} \Rightarrow \rho \propto a^{-3(1+w)} \tag{1.7}$$

For the case of non-relativistic matter, i.e., baryons and dark matter, we have $w = 0$ thus $\rho \propto a^{-3}$; for the case of relativistic matter (radiation), we have $w = 1/3$ thus $\rho \propto a^{-4}$, and for the case of dark energy as a cosmological constant, we have $w = -1$ thus $\rho \propto a^{0}$. According to the latest Planck results [4], assuming the ΛCDM model the parameter w for the equation of state of dark energy is $w = -1.03 \pm 0.03$.
We can calculate the evolution of the components of the Universe and its dynamical equations of motion using the Einstein field equations, which are defined as

$$G_{\mu\nu} = 8\pi G T_{\mu\nu}, \tag{1.8}$$

with an additional term $\Lambda g_{\mu\nu}$ added on the left-hand side of the equation, to account for the presence of a cosmological constant. Thus

$$R_{\mu\nu} - \frac{1}{2}g_{\mu\nu}R + \Lambda g_{\mu\nu} = 8\pi G T_{\mu\nu}. \tag{1.9}$$

where $G_{\mu\nu} = R_{\mu\nu} - \frac{1}{2}g_{\mu\nu}R$ is the Einstein tensor, $R_{\mu\nu}$ and R are the Ricci tensor and scalar, respectively. The left-hand side of the equation gives us the spacetime geometry, and the right-hand side describes all the matter/energy in the Universe. The Ricci scalar is defined as $R = R^{\mu}_{\mu} = g^{\mu\nu} R_{\mu\nu}$, where $g^{\mu\nu}$ is the inverse metric and the Ricci tensor is,

$$R_{\mu\nu} = \partial_{\lambda}\Gamma^{\lambda}_{\mu\nu} - \partial_{\nu}\Gamma^{\lambda}_{\mu\lambda} + \Gamma^{\lambda}_{\lambda\rho}\Gamma^{\rho}_{\mu\nu} - \Gamma^{\rho}_{\mu\lambda}\Gamma^{\lambda}_{\nu\rho} \tag{1.10}$$

where the Γ terms in the Ricci tensor are referred to as the *Christoffel symbols*, which in turn are defined as

$$\Gamma^{\mu}_{\nu\lambda} = \frac{1}{2} g^{\mu\alpha}(\partial_{\lambda} g_{\alpha\nu} + \partial_{\nu} g_{\alpha\lambda} - \partial_{\alpha} g_{\nu\lambda}). \tag{1.11}$$

Thus, using the Einstein equations for an FLRW metric with matter described by a perfect fluid we obtain

$$H^2 = \frac{8\pi G}{3}\rho, \qquad \frac{\ddot{a}}{a} = -\frac{4\pi G}{3}(\rho + 3p), \tag{1.12}$$

where $H \equiv \dot{a}/a$ is the Hubble parameter that describes the expansion rate of the Universe, G is the universal gravitation constant, ρ is the total density and p is the total pressure for all components. These are known as the Friedmann equations, and they give us information about the background homogeneous evolution of the Universe.

From the first equation of 1.12, we can derive the critical density of the universe, defined as $\rho_{c,0} = 3H_0^2/8\pi G$ for the present-day value, which is calculated to be $\rho_{c,0} = 2.8 \times 10^{11} h^2 M_{\odot} Mpc^{-3}$, where H_0 is the Hubble parameter today and $h \equiv H_0/100$. Given this parameter it is possible to define the density parameters in terms of the critical density, so $\Omega_{i,0} = \rho_{i,0}/\rho_{c,0}$, where, for ΛCDM, i runs with species as represents DM, DE and radiation components. Thus, we can rewrite the Friedmann equation as

$$H^2(t) = H_0^2 \left[\Omega_r \left(\frac{a_0}{a(t)} \right)^4 + \Omega_m \left(\frac{a_0}{a(t)} \right)^3 + \Omega_{\Lambda} \right], \tag{1.13}$$

or

$$H^2(z) = H_0^2[\Omega_r(1+z)^4 + \Omega_m(1+z)^3 + \Omega_{\Lambda}], \tag{1.14}$$

where $a_0 = 1$. From this equation we obtain the closure relation

$$1 = \Omega_r + \Omega_m + \Omega_{\Lambda}. \tag{1.15}$$

Thus only the dark energy density parameter is independent of the scale factor. The ΛCDM model can be described by a specific set of parameters varying according to taste. A commonly used set consists of $\Omega_b h^2$, $\Omega_c h^2$, H_0, τ, n_s and σ_8. These are: the baryon density Ω_b, the CDM density Ω_c, the present-day Hubble parameter H_0, the reionization optical depth τ, the scalar spectral index of the primordial perturbations n_s and the amplitude of the linear matter power spectrum on scales of $8h^{-1}$ Mpc, σ_8. The latter two parameters are related to the density perturbations which give rise to structure in our Universe. The density parameters are scaled using h. Concentrating on the density parameters, according to the Planck2018 results, $\Omega_m = 0.315 \pm 0.007$, $\Omega_b h^2 = 0.0224 \pm 0.0001$, $\Omega_c h^2 = 0.120\pm, 0.001$, $\Omega_\Lambda = 0.6847 \pm 0.0073$. The scalar spectral index $n_s = 0.965 \pm 0.004$ and $\sigma_8 = 0.811 \pm 0.006$.

1.3 Numerical cosmological simulations

Our aim is to study the evolution of perturbations in the Universe, which are mainly driven by the non-linear process of gravitational collapse. The resulting matter over and underdensities correspond to the large-scale structure (LSS) we know today, whose formation process in the fully non-linear regime can only be studied using numerical simulations.

In the last decades, N-body simulations have grown as a useful tool for cosmology, as they allow us to trace the motion of millions of particles representing the dark matter, which interact gravitationally, and whose clustering leads to the structures inferred to exist in our Universe today: the dark matter halos surrounding galaxies and galaxy clusters. Such simulations give us a picture of the large-scale structure (LSS) of our Universe, showing filamentary regions of high density, in which galaxies and galaxy clusters reside. The LSS can be observed in large galaxy surveys such as the 2dF Galaxy Redshift Survey [29], which is shown and compared with simulated data in Figure 1.1. It can be seen that the overall distribution of structure in numerical N-body simulations appears to match closely that inferred from astronomical observations. Such simulations therefore provide a means of running numerical experiments to test cosmological models and explore novel observational probes of the cosmological evolution.

One of the best-known simulations within the standard ΛCDM paradigm is the DM-only N-body simulation *Millenium* [67] (see right panel of Figure 1.1), in which $\sim 10^{10}$ particles were used in a cubic region of $500h^{-1}$Mpc. This simulation agree with the cosmological principle, with homogeneity and isotropy evident at scales $>$ 100 Mpc, while at smaller scales matter becomes structured in the form of filaments and voids. Later simulations, such as Illustris [33], have included hydrodynamical processes, introducing the contribution of baryonic matter and associated physical

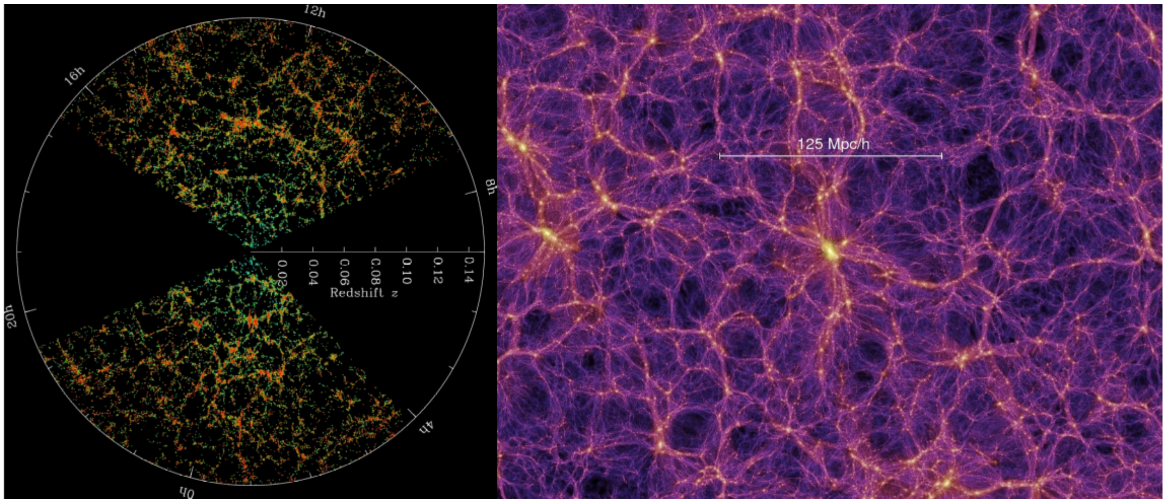

Figure 1.1: The large scale distribution of galaxies. The left panel is a slice of the observed galaxy distribution in our universe, gathered from the Sloan Digital Sky Survey [16]. Each dot represents a galaxy, and the slices are 2.5 degrees thick. The Earth is at the centre, and a redshift of 0.15 is approximately a distance of 2 billion light years. The right panel is a slice from the Millennium Simulation, which shows the computed dark matter halo distribution on large scales, assuming ΛCDM [67]. In both images one can clearly see galactic structures, which are often called the cosmic web due to the filaments resembling a spider's web.

processes, in particular supernovae and AGN feedback. Figure 1.2 taken from [67] shows some of the cosmological simulations that have been performed in recent years, the results of which are publically available in large databases.

From such simulations, we can obtain relevant information at both large and small scales, where the breadth of scales that may be studied depends on the resolution of the simulations. In particular by adjusting the number of particles and the size of the computational box we can determine the mass resolution and maximum length scale accessible, respectively. Furthermore the minimum accessible length scale is determined through the gravitational force resolution. Unfortunately the resolution of cosmological simulations is limited by computational cost, which increases as the number of particles increases, as well as the spatial resolution. Furthemore there are discreteness effects associated to the N-body method itself which can have an impact on the results of these simulations and therefore must be taken into account [66].

From the cosmological simulations, we can obtain information about the possible

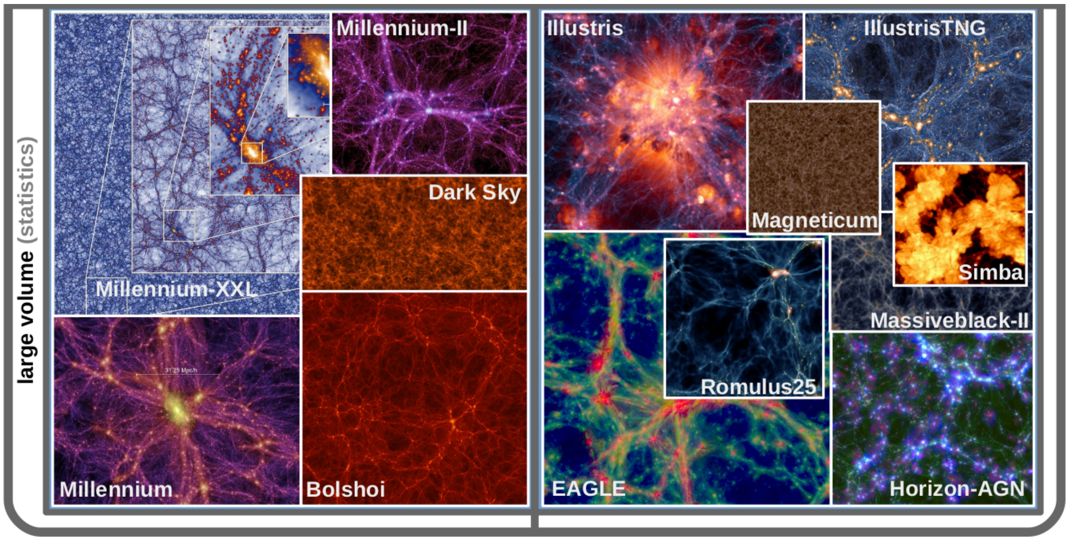

Figure 1.2: A selection of recent cosmological simulations. On the left we show N-body simulations which include only DM particles. On the right we show hydrodynamical simulations which include both DM particles and baryons [74].

mechanisms that have driven the evolution of the structure in the Universe, as well as constrain those parameters that define the cosmological model, which can be compared with observables. In the next section, we will investigate some ways to obtain this information, which we will then be used to study the results of our N-body simulations.

1.4 Power spectrum

One important way to statistically analyse the formation of structures in the Universe is through the power spectrum, which is the Fourier transform of the two-point correlation function. This very important tool allows us to analyse the growth of the matter perturbations on a very wide range of scales. This quantity is obtained in the following manner. If we consider the distribution of N points in a volume V, the number density will be $\rho_0 = N/V$. Now, if we consider two volume elements dV_a and dV_b, each with n_a and n_b particles, then the average number of particles in these two randomly chosen subvolumes will be

$$dN_{ab} = \langle n_a n_b \rangle \tag{1.16}$$
$$= \rho_0^2 dV_a dV_b (1 + \xi(r_{ab})) \tag{1.17}$$

where r_{ab} is the separation between dV_a and dV_b, and $\xi(r_{ab})$ is the correlation function. This relation defines the two-point correlation function in the limit of infinitesimal volumes. This is related to the power spectrum through the Fourier transform by

$$\xi(\vec{r}) = (2\pi)^{-3} \int P(\vec{k}) e^{i\vec{k}\cdot\vec{r}} d^3k. \tag{1.18}$$

We can write the density perturbations according to $\xi(r_{ab})$ in the form $1 + \xi(r_{ab}) = \langle(1 + \delta(r_a))(1 + \delta(r_b))\rangle$, being $\delta(r_a) = \frac{n_a}{(\rho_0 dV_a)} - 1$. Thus the power spectrum may be written in terms of the density perturbations as

$$\begin{aligned} P(\vec{k}) &= A|\delta(\vec{k})|^2 && (1.19) \\ &= A\delta_{\vec{k}}\delta_{\vec{k}} && (1.20) \\ &= \frac{1}{V}\int \delta(\vec{a})\delta(\vec{b}) e^{-i\vec{k}\cdot(\vec{a}-\vec{b})} dV_a dV_b. && (1.21) \end{aligned}$$

The correlation function allows us to spatially relate the density field in two positions

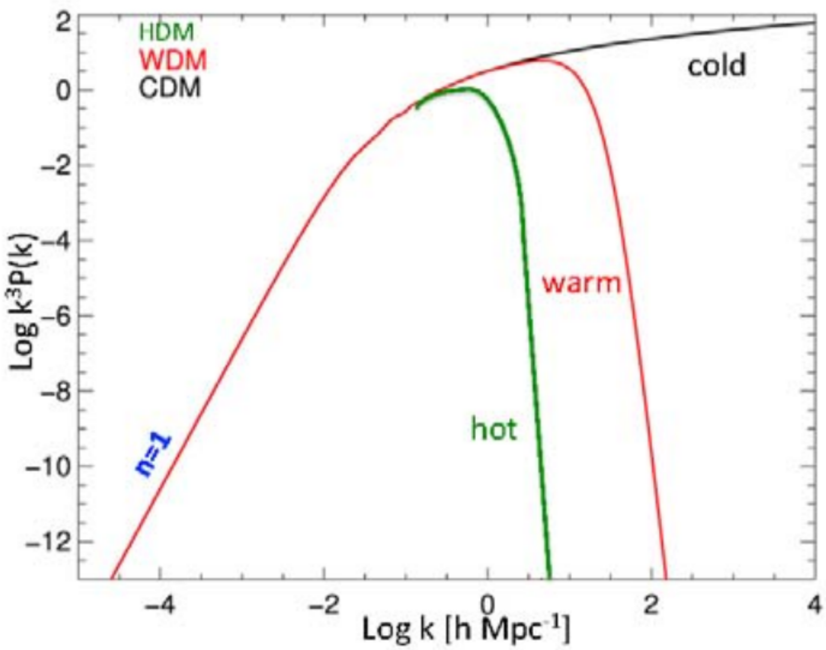

Figure 1.3: Linear power spectra for density perturbations in universes dominated by hot, warm and cold dark matter. The figure is taken from [32].

$(\delta(\vec{a}), \delta(\vec{b}))$ and determine the correlation between them. This tells us the degree of clustering on various scales, as the two-point correlation function for a homogeneous distribution of points will be very close to zero. Any deviation from such homogeneity will lead to non-zero contributions. The power spectrum clearly contains the same information but in Fourier space. Thus we refer to large and small scales with small and large values of k, where $\Delta(r) = \langle \frac{\rho(r)-\bar{\rho}}{\bar{\rho}} \rangle = \int dk P(k) \frac{sin(kr)}{kr}$, although the precise relationship is not so direct due to the properties of the Fourier transform.
The initial perturbations in the Universe (thought to be generated during a period referred to as *inflation*) may also be characterised using the power spectrum. This is usually referred to as the primordial power spectrum. In standard inflationary models this takes the form of a power law:

$$P_i(\vec{k}) \propto k^{n_s}, \tag{1.22}$$

where $n_s \simeq 0.96$, according to Planck. The power spectrum after the period of recombination and the non-linear processes linked to it may be written as

$$P_0(\vec{k}) = T^2(\vec{k}) P_i(\vec{k}) \tag{1.23}$$

where $T(\vec{k})$ is known as the transfer function and may be calculated from numerical Boltzmann solvers such as CAMB [41] or CLASS [40]. These codes calculate the full set of coupled perturbation equations arising from the Einstein equations considering all matter/energy components. The linear matter power spectrum at late times is then found by scaling the post-recombination power spectrum using the growth function, which depends on cosmology

$$P(\vec{k}, a) = D^2(a) P_0(\vec{k}). \tag{1.24}$$

The linear matter power spectrum for warm and hot dark matter models, as well as CDM, are shown in Figure 1.3, where the small-scale power in the WDM and HDM models is severely truncated, compared to CDM. Current observations appear to favour the CDM model, with structure forming hierarchically through the collapse and merger of small scales to form the large structures we know today.

1.5 Dark matter halos

The structure present in the cosmological simulations is formed by the clustering of dark matter in virialized overdensities referred to as dark matter halos. Thus a dark matter halo may be defined as a gravitationally bound object comprised of

dark matter particles which have fully decoupled from the cosmological expansion. Given the LCDM paradigm of bottom-up structure formation, halos may merge and be accreted into other halos, giving rise to the existence of subhalos within larger hosts. This is the essence of hierarchical structure formation. Thus, a massive halo of the order of $10^{14} M_{\odot}$ can contain about 10^5 particles. The ability to resolve DM halos in numerical simulations across the mass range from the most massive to low-mass substructures will depend on the resolution of the simulation. We now think that galaxies and galaxy clusters form within these halos [79]. The regions with the highest overdensity would be those that host galaxy clusters, whereas the lower-mass halo substructures would host galaxies.
We often distinguish between host halos and subhalos. Those halos that are gravitationally bound within the virial radius of a massive host halo, are referred to as subhalos. These substructures can be compared and tracked with the observed distribution of galaxies to compare theory with observations. In addition, with the information obtained from the halos, it is possible to study their properties, such as their abundance as a function of mass, known as the halo mass function, their clustering properties (such as the halo bias), their density profiles, and the phase space distribution of their substructures.

1.5.1 Halo mass function, density profiles & phase-space diagrams

The analysis of DM halos is very important for understanding the evolution of galaxies and galaxy clusters. The contribution of observational data and simulations has allowed us to constrain the parameters in cosmological models, as well as to determine the direct relationship between halos and galaxies. The galaxy-halo connection relates the distribution of dark matter halos to the abundance of galaxies as a function of stellar mass, known as the stellar mass function (SMF). A stellar-mass galaxy $M_{\star} = 10^8 M_{\odot}$ resides in a halo of $M_h = 10^{10-11} M_{\odot}$, and a massive galaxy (at the centre of a galaxy cluster) of $M_{\star} = 10^{12} M_{\odot}$, has a halo mass of $M_h = 10^{14} M_{\odot}$. Thus an important component in the study of galaxy evolution is information regarding the distribution of dark matter halo masses, such as that encapsulated in the halo mass function.

This function quantifies the abundance of DM halos of a given range of virial mass M_{vir}, which is often defined as M_{200}: the mass within a radius R_{200} at which the halo density is 200 times the critical density of the Universe, ρ_c. That is, $M_{200} = 200\rho_c(4\pi/3)R_{200}^3$.

From Press-Schechter theory the halo mass function has the following functional form:

$$\frac{dn}{d\ln(M)} = f(\sigma)\frac{\rho_0}{M}\frac{d\ln(\sigma^{-1})}{d\ln(M)}, \tag{1.25}$$

where ρ_0 is the mean density of the universe, $\sigma(M)$ is the variance of the linear density field and $f(\sigma)$ is a function that is determined empirically by fitting to simulations. In the literature, we can find several analytical expressions to define $f(\sigma)$. For this thesis we have used the definition given in [69], which was adjusted considering a large set of simulations with flat ΛCDM models as well as alternative models, with different box sizes and particle sets.

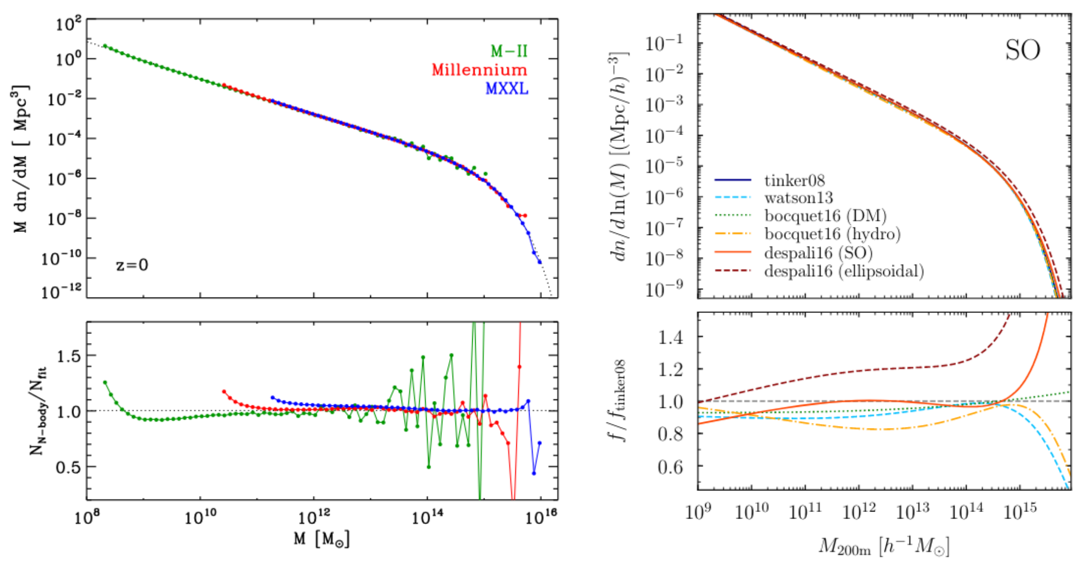

(a) (b)

Figure 1.4: Halo mass functions (HMF) for two halo finder methods: on the left we have the HMF for three runs of the Millenium simulation suite (Figure a) [32] using the Friends of Friends (FoF) method to allocate particles to halos. While Figure b [26] shows the HMF for different $f(\sigma)$ functions, using the 'Spherical Overdensity' (SO) method.

Figure 1.4 shows the HMF for the Millenium simulation (Figure a) [32], with particles allocated to halos using the 'Friends of Friends' (FoF) method, which selects neighbouring particles close to the host. While Figure (b) [26] shows the HMF for different $f(\sigma)$ functions given in the literature, where halos were found using the spherical overdensity (SO) method, using density contours defined by the virial radius of the host. As can be seen, both figures show similar behaviour in the shape of the HMF, with the accessed mass range depending on the resolution of the simulations. Given the high resolution of the Millenium-II run, substructures of the order of $10^8 M_\odot$ are formed, while the various simulations performed in the right panel of Fig. 1.4 only reach substructures of the order of $10^9 M_\odot$.

Another way to study the properties of halos is through their density profile, which has been shown, statistically, to follow a universal density profile, called the Navarro-Frenk-White profile (NFW) [48], which is given by

$$\frac{\rho(r)}{\rho_c} = \frac{\delta_c}{(r/r_s)(1+r/r_s)^2} \tag{1.26}$$

where r is the distance to the center of the halo, $\rho(r)$ is the density at r, ρ_c is the

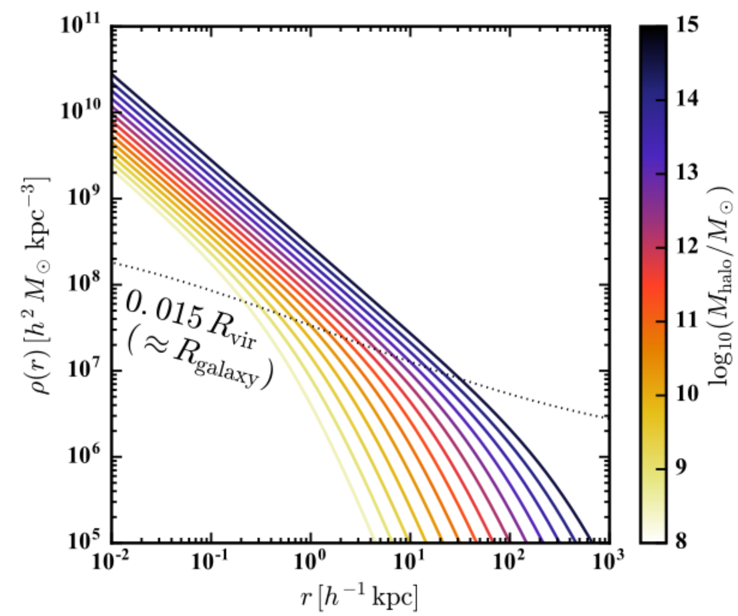

Figure 1.5: NFW profiles for DM halos and substructures in the ΛCDM model. Taken from [19]

critical density of the Universe, δ_c is the characteristic overdensity defined as

$$\delta_c = \frac{200}{3}\frac{c^3}{(\ln(1+c) - c/(1+c))}. \tag{1.27}$$

and $r_s = r_{200}/c$ is known as the scale radius, with c the concentration. This scale radius is related to the radius at which there is a change in the slope of the density profile: for $r \ll r_s$ we find $\rho \propto r^{-1}$, resulting in a central "cusp", whereas for $r \gg r_s$, the profile follows $\rho \propto r^{-3}$.

Figure 1.5, taken from [19], shows the NFW density profile for dark matter halos at z = 0, where the black line represents a galaxy cluster with $M_{vir} = 10^{15} M_{\odot}$, followed by density profiles of smaller structures, where the yellow line represents the smallest dwarf galaxies with $M_{vir} \approx 10^8 M_{\odot}$. As we can see, the NFW profile follows the same shape independent of the mass of the halos.

We finalise our discussion of tools that are useful for the analysis of DM simulations with the concept of phase-space diagrams, which have attracted much attention in the literature recently. These tools are very useful to study the formation history of galaxy clusters, and thus the build-up of large-scale structure. These plots comprise the position of a subhalo with respect to the host halo centre versus the velocity of that halo, again relative to the host. In order to stack plots for multiple clusters we can normalise the cluster-centric radius with the virial radius, and the velocity with the cluster velocity dispersion. It is important to note that simulations provide a means to construct the full phase-space of the cluster, while observations only permit the analysis of a projected phase-space.

Figure 1.6 shows a phase space for a massive cluster at z = 0 obtained in [58]. As can be seen, the populations of subhalos can be distinguished according to their position in phase space, which is related to the time of infall of the subhalo. We can distinguish distinct regions in the plot, with the right-hand side dominated by substructures that have not yet fallen into the virialised region (blue dots). In the case of substructures that have recently fallen into the potential well of the host, these achieve their maximum velocities when they pass pericentre (green dots), before they then move back out to apocentre, even surpassing in some cases R_{vir} (orange dots). Finally, we have the virialised region (lower left corner) populated by the oldest substructures that have fallen in (red dots).

In addition to obtaining information regarding their infall time into the host, these diagrams also indicate the likely contribution of dynamical friction for both massive and less massive halos. In the first case, this contribution drags structures closer to the center of the host, while in the second case, the large difference in mass would make dynamical friction ineffective. The contribution of this effect as well as the contribution of violent relaxation[1] leads to the build-up of the phase-space

[1] This is the process where the gravitational potential of the system, such as a galaxy cluster, evolves in time due to the changing mass content. This temporal evolution causes the potential

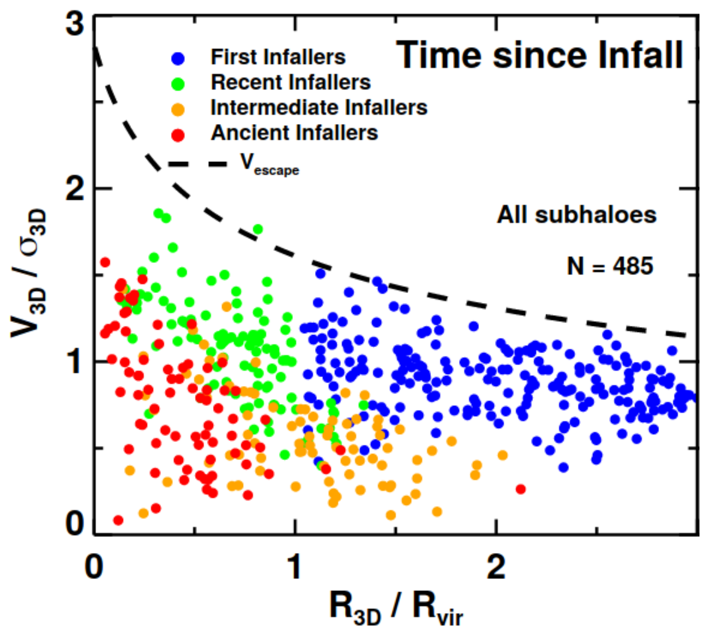

Figure 1.6: Phace space diagram for a massive cluster at z=0, taken from [58].

distribution, and thus provides clues as to the formation history of the cluster and the evolutionary history of the galaxies within.

As we have seen, these numerical studies have helped to build a better understanding of our Universe. While there is a wealth of observational evidence in support of the ΛCDM cosmological model, there remain some discrepancies with observations as well as theoretical issues. We will now discuss these.

1.6 Problems with the ΛCDM model

The cosmological constant may be interpreted as a homogeneous energy density that fills the Universe. A physical interpretation of this energy density from particle physics is as the vacuum energy density arising from zero-point quantum fluctuations. However, the predicted energy density due to these vacuum fluctuations differs from the observed value of the cosmological constant by at least around 60 orders of magnitude. This is known today as the *cosmological constant* problem

energy of the constituent galaxies within the cluster to change over time, and provides a mechanism for the cluster to reach dynamical (virial) equilibrium.

[78]. This fundamental problem has led to many proposals in particle physics that attempt to reconcile the discrepancy. Many of these proposals suggest that the cosmological constant, interpreted as the vacuum energy density, should in fact be equal to zero (perhaps due to some underlying symmetry mechanism), with the late-time accelerated expansion being caused by some other effect, either a modification of General Relativity or an additional matter/energy component. The latter option includes many possibilities (see the review [80]) of which the most studied is that of a scalar field referred to as quintessence, first postulated in [22]. In this thesis we will consider a quintessence field for the (dynamical) dark energy component, coupled to dark matter. Another problem associated with DE in the form of a cosmological constant is the *coincidence problem* (see Figure 6.1 of [8]) which makes us wonder if our current epoch is special or not, given that, in this model, the beginning of the DE dominated stage of the cosmological evolution occurred very recently, at a redshift of approximately $z \approx 0.3$. This problem redirects our attention to theories with a dynamical DE component, in particular those theories that include a coupling with DM, as this coupling may help explain the apparent coincidence.

According to observations of the Cosmic Microwave Background (CMB), Baryon Acoustic Oscillations (BAO) and Hubble parameter measurements H(z) [1],[3],[4], it has been proven that the ΛCDM model fits the data well. However, if we look deeper, we see that many of these data are model-dependent, which can make the analysis of these data somewhat questionable.

We can use Hubble's law, given by

$$v = H_0 D, \tag{1.28}$$

which gives the relationship between the distance D and the velocity v at which galaxies move away from each other by the Hubble flow. Since our universe is in a phase of accelerated expansion, this law is only valid at $z \ll 1$. Measurements of H_0 at scales $z > 1$ utilise methods that differ from those used at low redshift. These measurements, however, may be biased given that often the observational data on which they are based depends on a choice of cosmological model.
In Figure 1.7 we can see a comparison made by [73] of various measurements of H_0 for different data sets. As can be seen in the figure, the value of $H_0 \sim 67.4$ km $s^{-1} Mpc^{-1}$ in the early stage, and for the late Universe it reaches $H_0 = 76.5 \pm 4.0$ km $s^{-1} Mpc^{-1}$, showing differences in values between 4.0σ and 5.8σ. These discrepancies in the value of the constant are known as the *Hubble tension*. The tensions associated with H_0 have been addressed by several authors by referring to systematic errors in

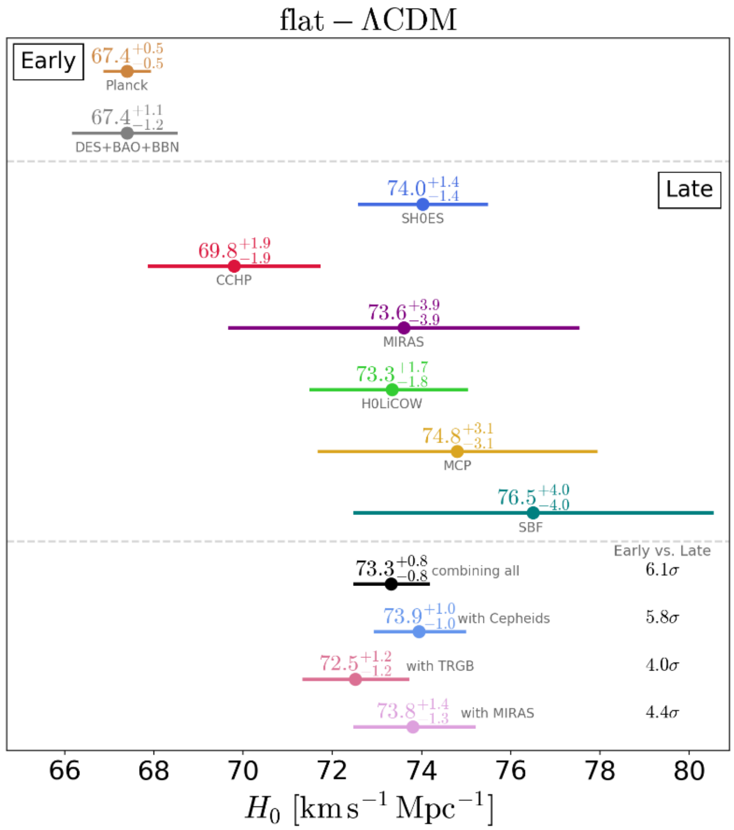

Figure 1.7: Comparison of H_0 measurements from different observational data compiled by Verde ([73] and references therein).

the measurements, however, the size of the discrepancies suggests that it cannot be explained by assuming these errors alone.

Within the cosmological parameters of the standard model, σ_8 provides us with an excellent tool to constrain matter formation as well as structure growth, so it is directly associated with the value of Ω_m. This is why any stress associated with 8 could have an impact on the model that governs it. The CMB and LSS observations have shown some discrepancies in this value, suggesting a tension between Ω_m and σ_8 as discussed in [2], indicating a lower structure growth rate than expected according to ΛCDM.

Associated with small scales, several studies, such as that of [49], have shown through rotation curves that the density profiles of satellite galaxies exhibit an inner

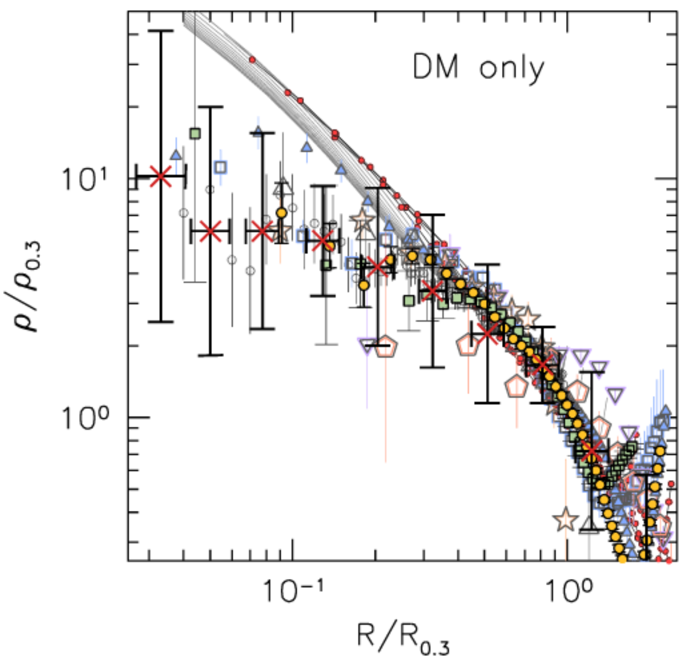

Figure 1.8: Observations of satellite galaxies [49] show an inner core of constant density, as opposed to the cusp in DM-only simulation halos. This is known as the "cusp-core problem".

core of nearly constant density, as shown in Figure 1.8. The situation is complex from the point-of-view of observations because as we know, these galaxies are dominated mainly by dark matter, making them difficult to observe. These observations contrast with the prediction from numerical simulations using the ΛCDM model that halos have a universal NFW density profile, which shows a "cuspy" behaviour in the innermost regions of the profile. This is another possible challenge of the model known as the *cusp core* problem. One possible solution to this problem comes from the contribution of feedback from the baryonic content of the halo, causing a redistribution of the dark matter and resulting in a cored profile [72]. It is not currently clear if such a mechanism is sufficient to resolve the problem, especially in very dark matter-dominated galaxies.

For a comprehensive review of the challenges to ΛCDM, particularly on large scales, see the review [53]. Another challenge is the problem associated with the number of observed satellite galaxies in the Milky Way compared to the number of low-mass DM halos obtained in simulations, known as the *missing satellites* problem. Figure 1.9 shows a comparison between a Milky Way-type halo, identified in a cos-

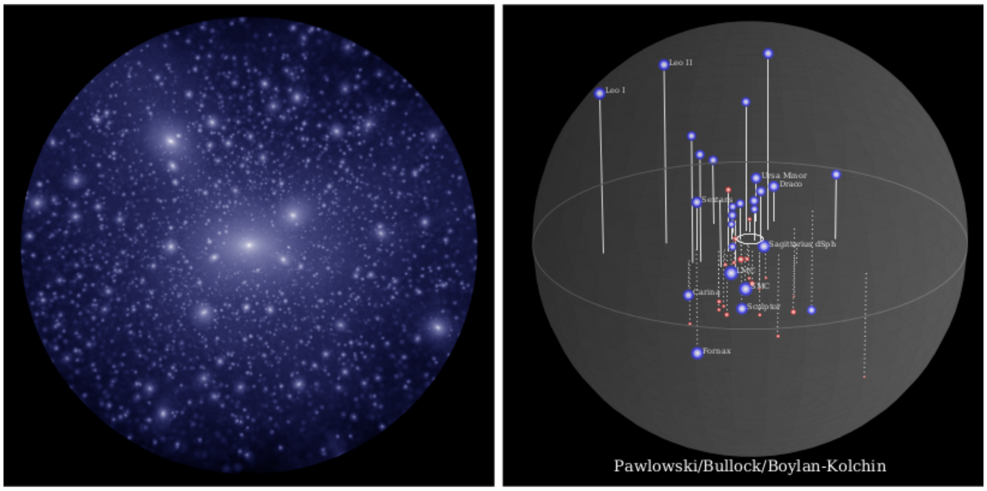

Figure 1.9: Taken from [19]. *Left panel:* a simulated Milky Way-type halo in the context of the ΛCDM model, showing a large number of satellites. *Right panel:* the known satellite galaxies around $\sim$ 250 kpc from the center of the Milky Way (outer sphere). The discrepancy between observations and simulations is known as the "missing satellites problem".

mological simulation (left panel) with its satellite galaxies predicted by the ΛCDM model. While the right-hand panel shows the known satellites observed around the Milky Way up to 2017. As can be seen, there is a big difference between these plots. The model predicts around 1000 subhalos (with $M_{sub} > 10^7 M_{\odot}$) that could host galaxies, while the number of satellite galaxies around the Milky Way within 300 kpc is only $\sim$ 50 known galaxies.

To address this problem, various solutions have been proposed. One possibility is that reionisation suppressed star formation in low mass halos [20]. It is also possible that tidal interactions stripped their baryonic material [18]. Again, a clearer understanding of baryonic processes inside the halos may provide a solution within the context of ΛCDM.

In addition, the study of the motion of satellite galaxies around the Milky Way has shown discrepancies concerning ΛCDM predictions. The expectation within the hierarchical structure formation scenario is that there would be an approximately isotropic distribution of these galaxies around their hosts. However, as studied in the Milky Way [51], in Andromeda [39] and the elliptical galaxy Centaurus A [47], it appears that their satellite galaxies are positioned in a planar distribution around the host galaxy, around which they have a coherent rotational motion. This structure is referred to as the "plane of satellites". There are some indications that this problem may not be as severe for ΛCDM as initially thought, due to the non-isotropic build-up of structure falling in through filaments [81]. However, given that observations suggest these satellite planes are ubiquitous [55] it is still not at all clear if this can be generally accommodated within the standard model.

Many authors, in order to alleviate the aforementioned tensions, have studied models beyond the standard cosmological model including models that do not even include a dark matter component [23]. To address the problems associated to Λ, many alternative models propose that the dark energy component is dynamical, rather than a cosmological constant. In addition, due to the issues at small scales that we have just discussed, it is worth considering the effect of a coupling between dark energy (as a dynamical field) and dark matter for the growth of structure in the Universe. We now consider numerical simulations in such models.

1.7 Beyond the standard model

There are two principal methods to build models beyond the ΛCDM model. The first is to modify the right-hand side of the Einstein equations by considering exotic matter components in the energy-momentum tensor $T_{\mu\nu}$, such as quintessence [22], K-essence [10] and Chaplygin gas models [37] amongst many others. The second method is to modify the left-hand side of Einstein's equations, known as modified gravity theories. There are many such theories, thus we only mention a few, such as $f(R)$ gravity [24], scalar-tensor [15] and braneworld theories [61].

1.7.1 Coupled DM-DE models

There are also models in which an interaction between the matter/energy components is proposed, when DE is considered as a dynamical quantity. This interaction may be exclusively in the dark sector, or may include interactions with the baryons and radiation. In our case, we will focus in this work on coupled models, where the coupling occurs only in the dark sector and is only at the level of a momentum exchange.

The coupling between the dark sector components can strongly influence both the background evolution and perturbations depending on the form of the coupling. In [6], a model with linear coupling was studied, considering a quintessence scalar field with exponential potential. It was found that the effect of the coupling on the power spectrum reduced and increased (very slightly) the value of σ_8 for large and small couplings, respectively. It was further shown that this type of model could approach solutions where $\Omega_\phi \simeq 0.67$ by imposing a constraint on the dimensionless beta coupling parameter to be $\beta < 0.1$, with this constraint arising from consideration of WMAP data [7]. In [75], the authors studied a coupled model in the dark sector, where the DM and DE components are expressed as a fluid. This type of coupling generated instabilities within the model, which, according to the same authors, could be avoided if the DE were considered as quintessence. In [62], they proposed that if there is an interaction at the level of the densities, the observational data favour that it is activated in the later stages of the evolution of the Universe, for example, $z \sim 0.9$. In the majority of studies, the coupling is usually introduced at the level of the continuity equations for DM and DE

$$\begin{aligned} \dot{\rho}_c + 3H\rho_c &= Q, \\ \dot{\rho}_{de} + 3H(1+\omega_{de})\rho_{de} &= -Q, \end{aligned} \tag{1.29}$$

where Q represents the coupling. Thus energy is conserved only for the total energy-momentum tensor, i.e., $\nabla_\mu T^\mu_\nu = 0$. This type of coupling described in [76] as $Q = \xi H \rho_c$ and $Q = \xi H(\rho_c + \rho_{de})$, can modify the background evolution of matter/energy, so that the parameter Q must be very small (see [76], e.g. $\xi = 0.01$), in order not to deviate excessively from the ΛCDM background predictions. In addition to these, one can also find theories, whose modification does not alter the background evolution, leaving it as a pure momentum transfer theory.

In [63] "dark scattering" models are discussed, which consider a momentum exchange between DM and DE. In this model, where the dark energy is treated as a fluid, a drag term in the velocity perturbation arises,

$$\dot{\theta}_Q = 2H\theta_Q - a n_D \sigma_D \triangle\theta + k^2\phi + k^2 \frac{\delta_Q}{1+w} \tag{1.30}$$

here they used the physical time where n_D is the proper number density of dark matter, σ_D is the scattering cross-section between DM-DE (denoted in the paper with subscript "c" and "Q", respectively), δ_Q and θ_Q are the density and velocity perturbations, and $\triangle\theta \equiv \theta_Q - \theta_c$ is the velocity contrast for both components. In [17], they analysed such models using various DE equations of state, as well as ξ-interaction parameter given by $\xi \equiv \sigma_D/m_{CDM}$, where m_{CDM} is the cold DM particle mass. They found that the effect of ξ on linear perturbations acts efficiently to suppress/increase the amplitude of the power spectrum for low and high values of k respectively.
This type of model is somewhat similar to the Type-3 model proposed in [56]. This momentum transfer model considers the dark energy component as a scalar field,

where there is also a modification of the cosmological friction term, as well as additional terms in the momentum transfer equation, these being proportional to the DE density contrast (δ_{DE}), which is absent in the dark scattering models. The presence of these additional terms thus implies that the Type-3 model of [56] is not reducible to the dark scattering model of [63], as discussed in [64]. This model was subsequently studied in [57], with a negative coupling constant, where it was found that this interaction showed suppression in structure growth, pointing to a reconciliation of CMB and LSS observations. These results are encouraging for this type of model, so we will focus this thesis on the Type-3 model, which we will introduce later. These theoretical studies have been complemented by multiple numerical investigations using N-body simulations, to which we will now turn.

1.8 N-body simulations of coupled models

In the literature, we can find a wide range of theoretical studies of alternative models, some of which have been further studied in cosmological simulations. In the vast majority of these studies the coupling appears at the level of the continuity equations for the DM-DE components, thus giving rise to an energy (density) exchange between these components and a coupling that is relevant at the background level, as discussed above.

Macciò et al. ([44]) studied such models of coupled dark matter-dark energy using N-body simulations, with a simplified treatment of the coupling. It was found that, for strong coupling, the DM density profiles tended towards higher concentrations, exacerbating the cusp core problem. However, the study of [11] found conflicting results for a similar coupling, showing a change in the slope of the density profile in the other direction, with a decrease in the central densities of the innermost regions of the DM halos.

A thorough study by Li et al. ([42], [43]) undertook a complete analysis of the consequences of these density-coupled DM-DE models. To begin with, the linear power spectrum was analysed where the contribution of baryons and DM was separated, observing that the presence of the coupling in the power spectrum at small scales shows an increase in the number of structures compared to ΛCDM, with this increase starting at a very early stage, even being relevant at $z = 49$ as shown in Figure 1.10. Thus, for these kinds of models, it is necessary to use initial conditions for the N-body simulations that differ from those of ΛCDM but are consistent with CMB measurements.

In addition it was found that the coupling effect leads to a modified non-linear matter power spectrum and mass function. As regards halo profiles it was shown that it is possible to see a reduction in the inner density profile, as compared to ΛCDM, although this suppression of the inner density is reduced for large couplings. In [43] the contributions of various effects in the coupled model are examined: (i) the modified background expansion, (ii) the varying particle mass, (iii) the fifth force, (iv) the velocity dependent force. It was found that the first effect, the modified background expansion, is by far the most consequential for structure formation in these models. Note that the coupling in the models examined in this thesis does not explicitly affect the background evolution except through a rescaling of the background quintessence field, leading to a modified w parameter, as we will see later.

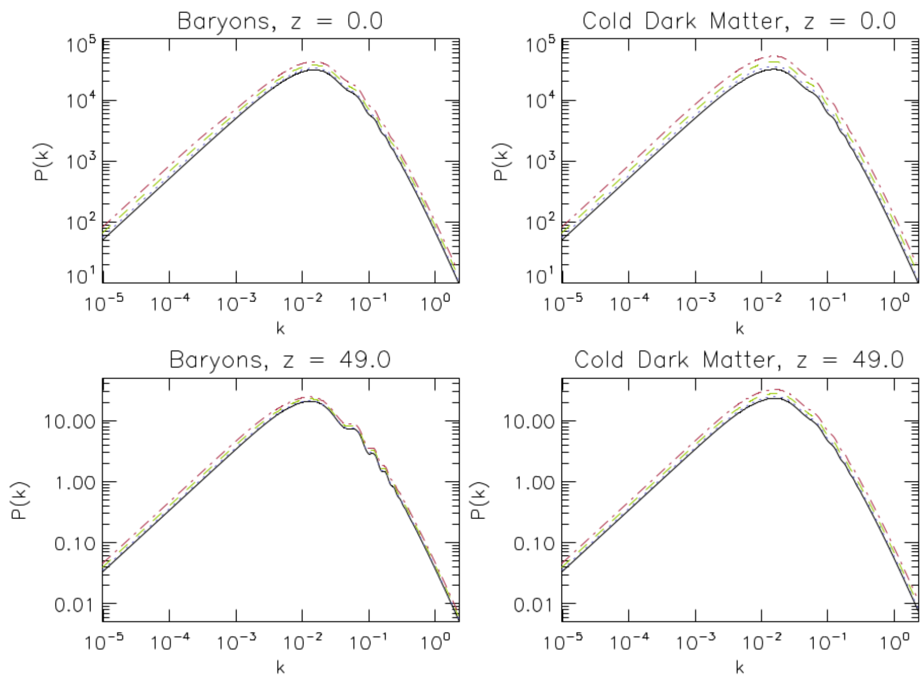

Figure 1.10: Taken from [42]. Linear power spectra for baryons (*left panel*) and DM (*right panel*) for coupled DM-DE models at z = 0 and z = 49. The black (solid line), blue (dotted line), green (dashed line) and red (dot-dashed) lines represent the values of the coupling parameter with $\gamma = 0.05, 0.10, 0.15$ and 0.20 respectively.

In [12] the CODECs project is discussed, which significantly extends the explored parameter space of such models, with both large-scale (L-CoDECS) and small-scale (H-CoDECS) models of dark matter density-coupled to dark energy, with the scalar field ϕ evolving according to a potential $V(\phi)$ of the exponential form. For all cases, they used the same initial conditions to make a comparison between the models, finding that the coupling effects could break the degeneracy between DE and σ_8 at linear scales, given that the linear power spectrum exhibits a faster decrease in amplitude compared to ΛCDM. It was further found that for many coupled DM-DE models there is significant enhancement in structure formation in the non-linear regime leading to a modification of the halo mass function. While there is degeneracy, again, with σ_8, this can again be broken by the redshift dependence of the HMF. The HMF at $z = 0$ for several models is shown in Figure 1.11.

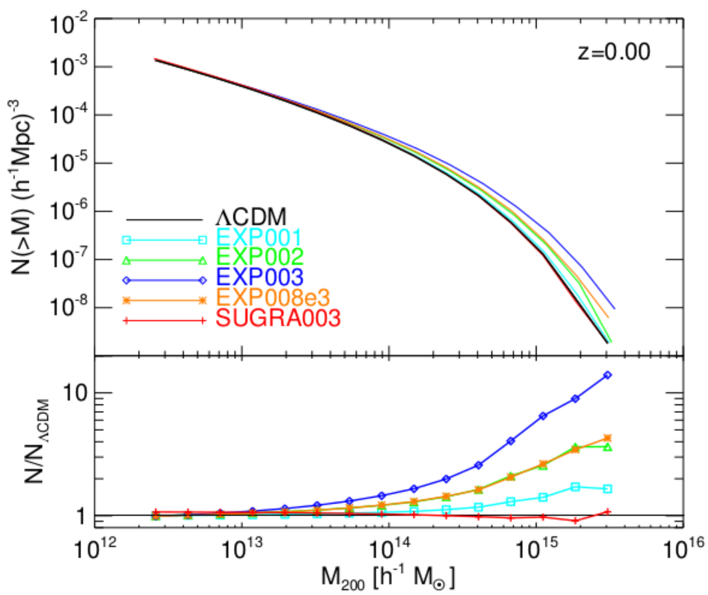

Figure 1.11: Taken from [12]. The halo mass function for various coupled DM-DE models.

In [13], they developed N-body simulations for the dark scattering models proposed by Simpson [63], for $w > -1$ and $w < -1$, where they found that the effect of DE-DM scattering on the linear power spectrum suppresses the power for $w > -1$ and increases it for $w < -1$. While in the nonlinear case, the effect is reversed, showing an increase for $w > -1$ and a 12% suppression for $w < -1$ at z = 0, as shown in Figure 1.12. They further analysed the HMF, finding that the effect of scattering results in a significant increase (decrease) of the halo abundance over the whole mass range for $w > -1$ ($w < -1$). In addition, they analysed the velocity dispersion of the halos, finding that an increase in the scattering parameter (ξ) leaves an increase in the velocity dispersion for all mass ranges when $w > -1$. While for $w < -1$, they did not find significant deviations attributed to the increase of ξ. In [14] the same

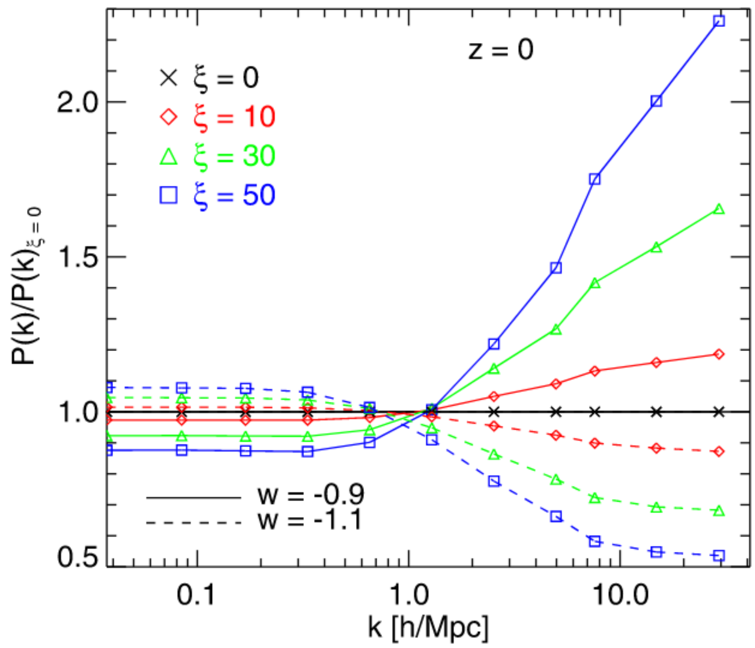

Figure 1.12: The nonlinear power spectrum for dark scattering models at z = 0 taken from [13].

authors again performed N-body simulations, this time considering a time-evolving equation of state for the dark energy w_{DE}, the results of which were compared with [13], with the time-dependent equation of state leading to a weaker impact of the coupling at non-linear scales. Thus the amplification found in the power spectrum in the previous study [13] is significantly suppressed in this case. These results, like those obtained for the type-3 model in [57], point to reconciliation between measurements at low z and the CMB.

In this thesis, we will focus on the study of the type-3 model given in [56], which has exhibited interesting properties in the theoretical studies we have mentioned, and may be able to alleviate some of the problems of the standard model of cosmology. We will analyze, using N-body simulations, the impact of this coupling on the growth of structures, the influence (if any) on the shape of the power spectrum and the properties of the halos, all by comparing with simulations of the ΛCDM model. We will now discuss the theory underlying the type-3 model, and our method for studying this model in the context of N-body simulations.

Chapter 2

Theory and Method

2.1 Quintessence

As mentioned earlier, we can consider a dynamical dark energy component of the Universe in the form of a quintessence field [22] to explain the accelerated expansion at late times. This canonical scalar field is denoted by ϕ, which is minimally coupled to gravity and whose acceleration occurs as a consequence of the trajectory of the field along a slowly varying potential $V(\phi)$.

The action describing the quintessence field coupled to gravity is given by

$$S = \int d^4x\sqrt{-g}\left[\frac{1}{2\kappa^2}R - \frac{1}{2}g^{\mu\nu}\partial_\mu\phi\partial_\nu\phi - V(\phi)\right] + S_m, \tag{2.1}$$

where $\kappa^2 = 8\pi G$, g is the determinant of the metric $g_{\mu\nu}$, R is the Ricci scalar and we include other matter components in the action S_m. The energy-momentum tensor for ϕ is obtained by a functional derivative of the scalar field sector of the above action with respect to the metric, and is given by

$$T^{(\phi)}_{\mu\nu} = \partial_\mu\phi\partial_\nu\phi - g_{\mu\nu}\left[\frac{1}{2}g^{\alpha\beta}\partial_\alpha\phi\partial_\beta\phi + V(\phi)\right]. \tag{2.2}$$

By using the FLRW line element 1.1 we can derive the dynamical equations of the ϕ field evolving in a background FLRW metric. In such a background the scalar field density and pressure may be obtained directly from the energy-momentum tensor as $\rho_\phi = \dot{\phi}^2/2 + V(\phi)$ and $p_\phi = \dot{\phi}^2/2 - V(\phi)$, respectively. The equation of state for ϕ then becomes

$$w_\phi \equiv \frac{p_\phi}{\rho_\phi} = \frac{\dot{\phi}^2/2 - V(\phi)}{\dot{\phi}^2/2 + V(\phi)}. \tag{2.3}$$

For the evolution of the background to be similar to that observed in ΛCDM, we have to consider that the density of ρ_ϕ, ρ_ϕ is larger than the density of matter at this epoch, i.e. when the dark energy domain begins. For this, the condition to be satisfied for a late accelerated expansion is given by $w < -1/3$, which translates very roughly into $\dot{\phi}^2 < V(\phi)$, where the dominance of the potential can only occur when the potential varies slowly, which ensures that the scalar field does not accelerate too much and thus the kinetic term remains small. This allows us to restrict the forms of the potential in the study of the quintessence field to explain dark energy.

The scalar field satisfies the continuity equation $\dot{\rho}_\phi + 3H(\rho_\phi + p_\phi) = 0$, i.e.,

$$\ddot{\phi} + 3H\dot{\phi} + V'(\phi) = 0, \tag{2.4}$$

where $V'(\phi) \equiv dV/d\phi$. Equation 2.4 is known as the Klein-Gordon equation (in this background). The equations of motion that determine the rate of expansion of the Universe (the Friedmann equations) are given by

$$H^2 = \frac{\kappa^2}{3}\sum_i \rho_i, \tag{2.5}$$

$$\dot{H} = -\frac{\kappa^2}{2}\sum_i (\rho_i + p_i). \tag{2.6}$$

where the sum is over all the matter-energy components of the Universe, including the quintessence field. The evolution of the scalar field is determined by the potential $V(\phi)$, of which many types are given in the literature. For this work, we will use the form of an exponential potential multiplied by a polynomial term, as discussed in [5], given by

$$V(\phi) = ((\phi - B)^\alpha + A)e^{-\lambda\phi}, \tag{2.7}$$

where A, B, α and γ are constants. The evolution of this type of potential we will discuss later.

2.2 Perturbed equations

To study structure formation we must consider the presence of inhomogeneities in the Universe. This is done by considering perturbations of the background homogeneous model and analysing the evolution of those perturbations. We will work to linear (first) order in those perturbations. This procedure is discussed in many works (see e.g. [8] and references therein). As we are interested only in the process of structure formation due to gravitational collapse, we will consider only the (coupled) quintessence field and cold dark matter. To begin with, we first perturb the metric $g_{\mu\nu}$ in the following manner

$$g_{\mu\nu} = g^{(0)}_{\mu\nu} + \delta g_{\mu\nu}, \tag{2.8}$$

where $g^{(0)}_{\mu\nu}$ is the background FLRW metric. Due to the general coordinate invariance of GR, the perturbed metric $\delta g_{\mu\nu}$ may include non-physical coordinate transformations (these are known as *gauge transformations*). Thus we must either work with gauge-invariant quantities or choose a specific gauge to ensure that we only consider the relevant physical perturbations. We follow the second route, choosing the so-called *Newtonian gauge*, given that it is straightforward to recover the Newtonian limit in this case, which will be necessary for our simulations. Thus, the line element 1.1 in this gauge can be rewritten as

$$ds^2 = a^2(\tau)[-(1+2\Psi)d\tau^2 + (1+2\Phi)\delta_{ij}dx^i dx^j], \tag{2.9}$$

where Φ and Ψ are spatial scalars and δ_{ij} is the 3-dimensional Kronecker delta (we always assume flat space). As we will see, these are related to the Newtonian gravitational potential in the Newtonian limit. Furthermore, we use conformal time τ, defined as

$$\tau = \int a^{-1} dt. \tag{2.10}$$

The Hubble parameter in terms of conformal time is

$$\mathcal{H} \equiv \frac{1}{a}\frac{da}{d\tau} = Ha. \tag{2.11}$$

To write the field equations at first order in the perturbations, we need to separate both the Einstein tensor $G_{\mu\nu}$ and the energy-momentum tensor $T_{\mu\nu}$ into background and perturbed parts: $G_{\mu\nu} = G^{(0)}_{\mu\nu} + \delta G_{\mu\nu}$ and $T_{\mu\nu} = T^{(0)}_{\mu\nu} + \delta T_{\mu\nu}$. Thus,

$$\text{order} \quad 0: \quad G^{(0)}_{\mu\nu} = 8\pi G T^{(0)}_{\mu\nu} \tag{2.12}$$

$$\text{order} \quad 1: \quad \delta G_{\mu\nu} = 8\pi G \delta T_{\mu\nu}. \tag{2.13}$$

Therefore, the background cosmological evolution is obtained by solving the zeroth-order Einstein equations, as discussed earlier. The first-order Einstein equations depend on the perturbed Christoffel symbols given by

$$\delta\Gamma^{\mu}_{\nu\lambda} = \frac{1}{2}\delta g^{\mu\alpha}(\partial_\lambda g_{\alpha\nu} + \partial_\nu g_{\alpha\lambda} - \partial_\alpha g_{\nu\lambda}) + \frac{1}{2}g^{\mu\alpha}(\delta\partial_\lambda g_{\alpha\nu} + \delta\partial_\nu g_{\alpha\lambda} - \delta\partial_\alpha g_{\nu\lambda}). \tag{2.14}$$

which depends on the perturbed metric, whose form is given above. The form of the perturbed energy-momentum tensor will depend on the matter-energy content in the Universe. We therefore now describe the details of the coupled DM-DE model we will study in this thesis.

2.3 Momentum coupled DM-DE model

The present thesis will focus on the study of the so-called Type-3 model discussed in [56], which deals with a quintessence model coupled to the dark matter fluid through a momentum-only coupling. This differs from the majority of the DM-DE coupled models discussed in the literature in that there is no coupling at the background level, i.e. there is no energy exchange at the level of the continuity equation. This coupling is introduced into the equations at the level of the Lagrangian, rather than being added in *ad hoc* to the fluid equations of motion, as commonly done in other studies. The presence of the coupling ultimately leads to a modified Euler equation, in the Newtonian limit, as we will demonstrate. This type of coupling keeps the background evolution similar (apart from a field rescaling) and only changes the perturbed motion of the fluid, causing an additional force to act on the dark matter, which we will see in more detail in later sections. From now on the only matter/energy components of the Universe we will consider will be the quintessence field and the dark matter.

The scalar field action of a general coupled model is given in [56] by

$$S_\phi = \int d^4x\sqrt{-g}\,(L(Y, Z, \phi, n))\,. \tag{2.15}$$

where

$$Y = \frac{1}{2}\phi_\mu\phi^\mu \qquad\qquad Z = u^\mu\phi_\mu. \tag{2.16}$$

The dark matter fluid 4-velocity is given by u^μ, $\phi_\mu \equiv \partial_\mu\phi$ and n is the dark matter particle number density. The form of L determines the specific model being considered. The Type-3 model of a general scalar field coupled to DM through a momentum coupling is given by

$$L = F(Y, Z, \phi) + f(n). \tag{2.17}$$

Given this, the energy-momentum tensor of the scalar field may be separated from that of the dark matter fluid, and is given by

$$T^{(\phi)}_{\mu\nu} = F_Y\phi_\mu\phi_\nu - Fg_{\mu\nu} - ZF_Z u_\mu u_\nu. \tag{2.18}$$

The energy-momentum tensor of the dark matter fluid may then be written in the standard perfect pressureless fluid form:

$$T_{\mu\nu} = \rho u_\mu u_\nu \tag{2.19}$$

The energy density and pressure of the scalar field are given as

$$\rho^{(\phi)} = Z^2 F_Y - Z F_Z + F, \tag{2.20}$$

$$p^{(\phi)} = \frac{1}{3} F_Y (Z^2 + 2Y) - F. \tag{2.21}$$

The equations of motion for the scalar field and the dark matter fluid are given by

$$\nabla_\mu (F_Y \phi^\mu + F_Z u^\mu) - F_\phi = 0, \tag{2.22}$$

and

$$u^\nu \nabla_\nu \rho + \rho \nabla_\nu u^\nu = 0, \tag{2.23}$$

Note that this is the standard uncoupled equation of motion for the dark matter fluid. Thus the coupling has no effect at the level of the DM density. The momentum transfer equation is given by

$$(\rho - Z F_Z) u^\beta \nabla_\beta u_\mu = \nabla_\beta (F_Z u^\beta) \tilde{\phi}_\mu + F_Z D_\mu Z, \tag{2.24}$$

where $D_\mu = q^\nu_\mu \nabla_\nu$ is the spatial derivative operator given in terms of the projection operator q^ν_μ, and $\tilde{\phi}_\mu = q^\nu_\mu \nabla_\nu \phi = D_\mu \phi = \partial_\mu \phi + u^\nu u_\mu \partial_\nu \phi$ is the spatial projection of the derivative of the scalar field. Note that this equation, in the absence of a coupling, is simply the standard geodesic equation for the dark matter fluid which reduces to the standard Euler equation for this fluid in the Newtonian limit.

To connect with the Newtonian limit, as is relevant for our N-body simulations, we must now apply the Newtonian gauge (in [56] the *synchronous gauge* is used) described by the line element given in 2.9 and the 4-velocities which are,

$$\begin{aligned} u_0 &= -a(1 + \Psi), \\ u_i &= a v_i, \end{aligned}$$

where v_i is the velocity perturbation of the fluid and Ψ is one of the previously defined scalar components of the perturbed metric. Applying this to the model equations we can obtain the cosmological equations that will allow us to describe the evolution of both the scalar field and the dark matter fluid. These equations will then be introduced into the code to generate the simulations.

In order to proceed further at this point we now specialise to a coupled quintessence model, where the function $F = Y + V(\phi) + \gamma(Z)$. The scalar field is written as the sum of a background part and a perturbed part:

$$\phi = \bar{\phi} + \varphi \tag{2.25}$$

We will also make use of the dark matter velocity divergence $\theta \equiv \nabla_i v_i$ where ∇_i is the usual 3 dimensional gradient operator on flat space.

To first order in perturbations, we obtain for the Einstein equations [8]

$$\begin{aligned} 3\mathcal{H}(\mathcal{H}\Psi - \dot{\Phi}) + \nabla^2\Phi &= -4\pi G\bar{\rho}\delta a^2 && (2.26)\\ \nabla^2(\dot{\Phi} - \mathcal{H}\Psi) &= 4\pi G\bar{\rho}\theta a^2 && (2.27)\\ \Psi &= -\Phi && (2.28)\\ \ddot{\Phi} + 2\mathcal{H}\dot{\Phi} - \mathcal{H}\dot{\Psi} + (\mathcal{H}^2 - 2\dot{\mathcal{H}})\Psi &= 0, && (2.29) \end{aligned}$$

Since we want to take our analysis to small scales, we will pass the equations to Fourier space considering the Newtonian limit, i.e., when $k \gg \mathcal{H}$, so each perturbed quantity ϕ and its derivatives can be substituted as follows,

$$\begin{aligned} \phi(x,\tau) &\to \phi(\tau), && (2.30)\\ \nabla\phi(x,\tau) &\to k\phi(\tau), && (2.31)\\ \nabla^2\phi(x,\tau) \equiv \nabla_i\nabla^i\phi(x,\tau) &\to k^2\phi(\tau). && (2.32) \end{aligned}$$

Thus, the Einstein equations in Fourier space can be written as

$$\begin{aligned} k^2\Phi + 3\mathcal{H}(\dot{\Phi} - \mathcal{H}\Psi) &= 4\pi G\bar{\rho}\delta a^2, && (2.33)\\ k^2(\dot{\Phi} - \mathcal{H}\Psi) &= -4\pi G\bar{\rho}\theta a^2, && (2.34)\\ \Psi &= -\Phi, && (2.35)\\ \ddot{\Phi} + 2\mathcal{H}\dot{\Phi} - \mathcal{H}\dot{\Psi} + (\mathcal{H}^2 - 2\dot{\mathcal{H}})\Psi &= 0. && (2.36) \end{aligned}$$

The combination of equations 2.33 and 2.34 reduces to $k^2\Phi = 4\pi G\bar{\rho}a^2\delta$ in the large k limit which is the usual Poisson equation.

The evolution of the cold dark matter fluid at the background level is given by the standard equation 2.23:

$$\dot{\rho} + 3\mathcal{H}\rho = 0, \tag{2.37}$$

and the evolution of the CDM fluid perturbations are

$$\dot{\delta} + \nabla_i v_i + 3\dot{\Phi} = 0. \tag{2.38}$$

where the dot denotes a derivative with respect to conformal time. Again, we see that the density evolution is unaffected by the presence of the coupling. On the other hand, the background evolution of the scalar field, using 2.22 at order zero is given by

$$\ddot{\phi} - \gamma_{ZZ}\ddot{\phi} + 2\mathcal{H}\dot{\phi} + \gamma_{ZZ}\mathcal{H}\dot{\phi} - 3a\mathcal{H}\gamma_Z + a^2 V_\phi = 0. \tag{2.39}$$

We thus see that the coupling is present for the background scalar field, as a field rescaling. For the perturbations at first order, from equation 2.22 we obtain

$$\begin{aligned} V_{\phi\phi}\varphi a^2 &+ 3\gamma_Z \Psi a \mathcal{H} + 3\gamma_Z a\dot{\Phi} - \gamma_Z a \nabla^2\theta - \gamma_{ZZZ}\frac{\ddot{\bar{\phi}}}{a}\dot{\varphi} + \gamma_{ZZZ}\frac{\dot{\bar{\phi}}}{a}\dot{\varphi}\mathcal{H} \\ &+ 2\gamma_{ZZ}\Psi\ddot{\bar{\phi}} - 2\gamma_{ZZ}\Psi\dot{\bar{\phi}}\mathcal{H} + \gamma_{ZZ}\dot{\Psi}\dot{\bar{\phi}} - \gamma_{ZZ}\ddot{\varphi} - 2\gamma_{ZZ}\dot{\varphi}\mathcal{H} - 2\Psi\ddot{\bar{\phi}} \\ &- 4\Psi\dot{\bar{\phi}}\mathcal{H} - 3\dot{\Phi}\dot{\bar{\phi}} - \dot{\Psi}\dot{\bar{\phi}} + \ddot{\varphi} - \nabla^2\varphi + 2\dot{\varphi}\mathcal{H} = 0 \end{aligned} \tag{2.40}$$

In Fourier space, in the limit of large k (small scales), this simplifies to $\varphi = a\gamma_z\theta$.

Using the large k limit solution for φ we can now write the momentum transfer equation (2.24) as

$$\begin{aligned} \dot{\theta} + \mathcal{H}\theta + \Psi =& \frac{1}{a\bar{\rho} - \gamma_Z\dot{\bar{\phi}}}\left[2\gamma_Z\dot{\bar{\phi}}\theta\mathcal{H} + 3a\gamma_Z^2\theta\mathcal{H} - \gamma_Z\Psi\dot{\bar{\phi}} + \gamma_Z\ddot{\bar{\phi}}\theta + a\gamma_Z^2\mathcal{H}\theta + a\gamma_Z\gamma_{ZZ}\dot{\bar{Z}}\theta + a\gamma_Z^2\dot{\theta}\right] \\ &- \frac{1}{a^2\bar{\rho} - a\gamma_Z\dot{\bar{\phi}}}\left[\gamma_{ZZ}\dot{\bar{\phi}}^2\theta\mathcal{H} - \mathcal{H}\gamma_Z\gamma_{ZZ}\dot{\bar{\phi}}\theta + \gamma_{ZZ}\dot{\bar{\phi}}\ddot{\bar{\phi}}\theta + \gamma_Z\gamma_{ZZ}\dot{\bar{\phi}}\theta\right] \end{aligned} \tag{2.41}$$

where $\dot{\bar{Z}} = 1/a(\ddot{\phi} + \mathcal{H}\dot{\phi})$. This is the modified Euler equation and as we can see, the coupling modifies the force acting on the dark matter fluid, with an additional contribution to the gravitational force as well as the cosmological friction term. In the absence of the coupling i.e. for $\gamma = 0$, we recover the standard Euler equation for the dark matter fluid. This equation must now be implemented in our N-body simulations.

2.4 Method

We now discuss our numerical implementation of the modified Euler equation in a gravitational N-body simulation.

2.4.1 RAMSES code

The RAMSES code is an adaptive mesh refinement (AMR) open-source N-body/hydrodynamics code used for collisionless N-body dynamics to model the cold dark matter component as well as a Godunov-type finite volume hydrodynamics solver to model the baryonic component [68]. The software allows us to solve the Euler equation of the dark matter fluid (as represented with particles) in the presence of self-gravity. Furthermore, the code is parallelised with MPI to take advantage of large-scale computing facilities.

The gravitational dynamics of the particles are calculated using the particle mesh (PM) method, where the Poisson equation is solved on the grid and then used to calculate forces which are interpolated to the particle positions. This method, valid for collisionless systems, allows for a reduced integration time compared to other methods such as direct particle-particle (PP) solvers.

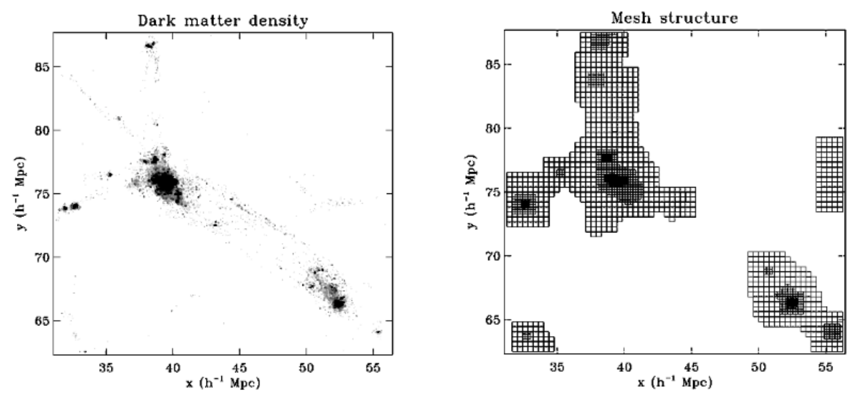

Figure 2.1: Visualisation of the adaptive mesh refinement in the spatial distribution of dark matter.

In Fig. 2.1 we see how the adaptive mesh refinement procedure places high resolution grids in regions of high DM density. On the left of the figure we see a DM particle distribution, and on the right the AMR grids that have been generated to cover the high density regions. The advantage of using an AMR scheme (in the N-body solver) is that the force calculation achieves a higher resolution in regions where particle velocities are highest, precisely where the determination of the particle trajectories requires more precision. Furthermore, the use of spatially limited regions of high resolution grids reduces the computational cost considerably, when compared with the cost of using such a high resolution grid throughout the entire computational volume.

The code calculates the motion of the N-body system by applying to each particle the standard Newtonian equations of motion for particles moving in the presence of a gravitational field:

$$\frac{dx_p}{dt} = v_p, \qquad \frac{dv_p}{dt} = -\nabla_x \phi, \qquad \text{where } \nabla_x \phi = 4\pi G \rho, \tag{2.42}$$

where the subscript "p" indicates particles, such that v_p and x_p are the velocity and position of each particle, and $\nabla_x \phi$ is the gravitational acceleration. We will discuss later the form of these equations relevant for an expanding cosmological background.

2.4.2 Modified Euler equation

We follow [56] and define the coupling as

$$\gamma(Z) = \gamma_0 Z^2 \tag{2.43}$$

where γ_0 is a constant whose value is assumed to be in the range $0 \leq \gamma_0 < 1/2$. Note that a negative value for γ_0 may in fact lead to more favourable observational consequences, as discussed in [57]. We leave this for future work. The equation 2.41 becomes

$$(1 + h_1)\dot{v}_i + (1 + h_2)\mathcal{H} v_i + (1 + h_3)\nabla_i \Psi = 0 \tag{2.44}$$

where the coefficients h_1, h_2 and h_3 are

$$\begin{aligned} h_1 &= \frac{4\gamma_0^2 \dot{\phi}^2}{a^2\rho - 2\gamma_0 \dot{\phi}^2}, \\ h_2 &= \frac{(8\gamma_0^2 - 2\gamma_0)\dot{\phi}^2 + (8\gamma_0^2 - 4\gamma_0)\dot{\phi}\ddot{\phi}\frac{1}{\mathcal{H}}}{a^2\rho - 2\gamma_0 \dot{\phi}^2}, \\ h_3 &= \frac{2\gamma_0 \dot{\phi}^2}{a^2\rho - 2\gamma_0 \dot{\phi}^2}. \end{aligned} \tag{2.45}$$

In the h_2 term, we can replace $\ddot{\phi}$ using the evolution equation of the background field[1], given by equation 2.39, with

$$\ddot{\phi}(1 - 2\gamma_0) + 2\mathcal{H}\dot{\phi}(1 - 2\gamma_0) + a^2 V_\phi = 0., \tag{2.46}$$

[1]Here we can see the presence of a strong coupling problem, as discussed in [56], when $\gamma_0 = 1/2$. The largest value of γ_0 that we consider is $\gamma_0 = 0.3$.

where we have used equation 2.43. Note that the coupling constant appears in this equation for the background evolution of the scalar field as an effective rescaling of ϕ. Thus, h_2 can be written as

$$h_2 = \frac{4\gamma_0(\frac{3}{2} - 2\gamma_0)\dot{\phi}^2 + 4\gamma_0\dot{\phi}a^2V_\phi/\mathcal{H}}{a^2\rho - 2\gamma_0\dot{\phi}^2}. \tag{2.47}$$

From this, we can see that in the absence of the coupling we have $h_1 = h_2 = h_3 = 0$, and the Euler equation reduces to its standard form.

With the Euler equation written in this form, we can immediately see in what circumstance we would have modified dynamics, as compared with the uncoupled case. As the denominator $a^2\rho - 2\gamma_0\dot{\phi}^2$ approaches zero the values of h_i will grow without bound. Due to the positivity of all quantities in both terms in the denominator we can therefore state that there will be a significant modification to the dynamics when

$$a^2\rho \approx 2\gamma_0\dot{\phi}^2. \tag{2.48}$$

Given that the dark matter density evolves as for the standard case, we can write the condition for large deviations from the standard dynamics as

$$2a\gamma_0\dot{\phi}^2 \approx \rho_0 \tag{2.49}$$

where ρ_0 is the present-day dark matter density. As we will see later, this condition is satisfied at late times for all of our models.

To write our equation in the code, we must first take into consideration the *supercomoving coordinates* [45] used in RAMSES, which are defined as

$$\begin{aligned} \vec{v} &= H_0 L \frac{1}{a}\tilde{\vec{u}}, \\ \vec{x} &= \frac{1}{a}\frac{\tilde{\vec{x}}}{L}, \\ dt &= a^2\frac{d\tilde{t}}{H_0}, \\ \Psi &= \frac{L^2H_0^2}{a^2}\tilde{\Phi}, \end{aligned} \tag{2.50}$$

where L is the length of the simulation box. The coordinates denoted with a tilde are the supercomoving coordinates. To simplify the notation, we will apply the transformation and then remove the tildes. Thus, using 2.50 in equation 2.44 we get

$$\frac{d\vec{u}}{dt} = -\frac{h_2 - h_1}{1 + h_1}a^2\frac{H}{H_0}\vec{u} - \frac{1 + h_3}{1 + h_1}\vec{\nabla}\Phi. \tag{2.51}$$

Thus when $h_1 = h_2 = h_3 = 0$, we return to the standard form $\frac{d\vec{u}}{dt} = -\vec{\nabla}_x \Phi$, which is simply Newton's second law for a conservative force given by a potential Φ. We can therefore see that transforming the Euler equation to supercomoving coordinates, in the uncoupled case, eliminates the cosmological friction term, simplifying the calculations in the code. In the presence of the coupling, however, the cosmological friction term is explicitly present, even in supercomoving coordinates. Note that 2.51 uses the Hubble parameter with respect to physical time.

2.4.3 Modification in RAMSES

We now have the modified Euler equation 2.51 in a form in which it may be discretised and solved numerically. In RAMSES, a finite difference approximation is used to resolve the equations of motion, using a predictor-corrector scheme. Given an acceleration $-\nabla\phi^n$ at a time t^n, with particle positions x_p^n, the values of x_p^n and v_p^n are updated first by the predictor step

$$\begin{aligned} v_p^{n+1/2} &= v_p^n - \nabla\phi^n \Delta t^n/2, \\ x_p^{n+1} &= x_p^n + v_p^{n+1/2}\Delta t^n/2, \end{aligned} \tag{2.52}$$

which is then followed by the corrector step, using the updated gravitational potential:

$$v_p^{n+1} = v_p^{n+1/2} - \nabla\phi^{n+1}\Delta t^n/2. \tag{2.53}$$

Note that the time-step in RAMSES is adaptive, thus we write Δt^n. To connect with the implementation of the modified Euler equation in the code, we write the finite difference update of the velocity as

$$\frac{v_p^{n+1/2} - v_p^n}{(1/2)\Delta t^n} = F, \tag{2.54}$$

where F is the force acting on the particle. This is simply a finite difference approximation to the differential equation 2.51 in the absence of coupling. Thus, we can easily modify the velocity update as required to implement equation 2.51 in the following way:

$$v_p^{n+1/2} = v_p^n - \frac{h_2 - h_1}{1 + h_1} a^2 \frac{H}{H_0} v_p^n \Delta t^n/2 + \frac{1 + h_3}{1 + h_1} F\Delta t^n/2. \tag{2.55}$$

We now define two new coefficients ϵ_1 and ϵ_2 to simplify the expression,

$$\epsilon_1 = 1 - \frac{h_2 - h_1}{1 + h_1} a^2 \frac{H}{H_0} \Delta t^n/2 \tag{2.56}$$

$$\epsilon_2 = \frac{1 + h_3}{1 + h_1} \tag{2.57}$$

so finally equation 2.55 becomes

$$v_p^{n+1} = \epsilon_1 v_p^n + \epsilon_2 F \Delta t/2. \tag{2.58}$$

This is the equation we have implemented in RAMSES. The standard dynamics is recovered by setting $\epsilon_1 = \epsilon_2 = 1$ which is equivalent to having all the h_i equal to zero.

2.4.4 Obtaining the background values

Going back to the modified Euler equation (2.44), we can see that the h_i values (or, equivalently, the ϵ_1 and ϵ_2 coefficients in RAMSES) depend on background quantities such as ρ, ϕ, and $\mathcal{H}$. To solve the evolution of these values we used a modified version of the Cosmic Linear Anisotropy Solving System (CLASS) code[2], which calculates the evolution of linear perturbations in the Universe [40]. CLASS includes the option to add a quintessence field to the matter-energy components of the Universe. Our modifications of the code were to include the coupling term in the Klein-Gordon equation (2.39), the scalar field perturbation equation (2.40) and the momentum transfer equation (2.41), although in practice for the N-body simulations we only require the modified background Klein-Gordon equation. We use the perturbation equations only momentarily to confirm that there is a minimal impact on the CMB power spectrum. We also used the form of the potential, given in eq. 2.7, which is already included in CLASS. The parameter values for the potentials we have considered are given in Table 3.1. CLASS therefore calculates the background evolution equations for all components of the Universe (including baryons and radiation), giving us tabulated values for all background quantities at a large number of redshifts. Obtaining these values, we then transform the conformal time given in the table calculated by CLASS to the *superconformal time* used in RAMSES using a `Python` code.

For each model we obtain the background evolution (shown in §3.1). The table of background values generated by CLASS is then read by RAMSES in order to calculate the values of the ϵ_1 and ϵ_2 coefficients in the modified Euler equation. The values are determined at the appropriate redshift by linear interpolation of neighbouring values in the table.

[2]`https://lesgourg.github.io/class_public/class.html`

2.4.5 Initial conditions and parameters for the N-body simulation

The initial conditions for the simulations were generated using MUSIC (MUlti Scale Initial Conditions) [35], which uses second order Lagrangian cosmological perturbation theory to displace the particles from a regular ordered grid to their starting positions, given a value for the initial redshift of the N-body simulation. These displacements are determined from the density perturbations at that redshift, which are calculated using a transfer function applied to the primordial power spectrum of density fluctuations, thus ensuring the appropriate matter power spectrum is represented in the initial conditions. The transfer function used in MUSIC was obtained

Parameter	Value
H_0	70 km s^{-1} Mpc^{-1}
Ω_m	0.3
Ω_Λ	0.7
Ω_b	0.04
σ_8	0.88
n_s	0.96

Table 2.1: The set of cosmological parameters used to generate the initial conditions in MUSIC.

using CAMB (Code for Anisotropies in the Microwave Background [41]), assuming a standard ΛCDM cosmology. Given that the background evolution of the dark matter fluid is unaffected by the coupling in our models, the transfer function at high redshift is effectively identical to the uncoupled case and very similar to that of ΛCDM. In addition, leaving the transfer function fixed allows us to generate identical initial conditions for all models, thus simplifying the process of comparing the low-redshift results. In MUSIC we define various parameters of the simulation, such as the physical box size, which is taken to be 32 Mpc h^{-1}, the number of particles $N_p = 128^3$ and the initial redshift z_{ini}, which was chosen as $z_{ini} = 50$.

While these parameters correspond to a small box size with limited resolution, this is sufficient for a first exploration of the effect of the coupling.

As for the generation of the transfer function, the cosmological parameters in MUSIC were chosen as for a standard ΛCDM simulation (see table 2.1). Again, we made this choice to be able to compare all models (those with a coupled scalar field, an uncoupled scalar field and the standard model) using the same initial conditions.

We leave for future work the use of fully consistent simulations with appropriately modified initial conditions.

Chapter 3

Results

Below we present the results obtained from our simulations using the CLASS and RAMSES codes. All the simulations are summarized in Table 3.1 with three additional cases given in Table 3.2, which consider the individual contributions of each Euler coefficient: ϵ_1 and ϵ_2. In total we ran 12 simulations with a total time of ~ 42 hours using the KOSMOS computer from Instituto de Física y Astronomía of the Universidad de Valparaíso.

3.1 Background evolution

We used the CLASS code to obtain the evolution of the background quantities, considering a form for the potential that is capable of producing a background evolution similar to that of ΛCDM. Our idea is not to deviate excessively from the background evolution of the standard model, because it has been well constrained by observational data, as we have mentioned in previous sections. For the analysis we considered three models with exponential potentials which we have summarized in Table 3.1. The density parameters Ω_i, we have obtained, with i corresponding to DM, DE, baryons and radiation, are broadly consistent with those of ΛCDM. Figure 3.1 shows the evolution of Ω_ϕ and a comparison with Ω_Λ. For each model we consider several values of γ_0, with $\gamma_0 = 0.3$ being the strongest coupling case that we consider. As we can see in the figure, the values obtained for Ω_ϕ are in broad agreement with the evolution of Ω_Λ in the standard case. For models A (blue lines) and B (green lines) we do not find major deviations when comparing the evolution for each γ_0 value. For the case of model C, we find some deviations which become more significant for $\gamma_0 = 0.3$ (orange dotted line), this being the model that most deviates from ΛCDM (black line). This deviation arises because a higher value of

Model	Potential	γ_0	A	B	λ	α	ϕ	$\dot{\phi}$
	$e^{-\lambda\phi}$	0	-	-	1.597723e-1	-	100	10
A	$e^{-\lambda\phi}$	0.15	-	-	1.597723e-1	-	100	10
	$e^{-\lambda\phi}$	0.3	-	-	1.597723e-1	-	100	10
ΛCDM	-	-	-	-	-	-	-	-
	$[(\phi-B)^\alpha+A]e^{-\lambda\phi}$	0	0.001	34.8	2.432815e-1	2.0	100	10
B	$[(\phi-B)^\alpha+A]e^{-\lambda\phi}$	0.15	0.001	34.8	2.432815e-1	2.0	100	10
	$[(\phi-B)^\alpha+A]e^{-\lambda\phi}$	0.3	0.001	34.8	2.432815e-1	2.0	100	10
	$[(\phi-B)^\alpha+A]e^{-\lambda\phi}$	0	20.0	3.8	9.347720e-1	17.0	100	10
C	$[(\phi-B)^\alpha+A]e^{-\lambda\phi}$	0.15	20.0	3.8	9.347720e-1	17.0	100	10
	$[(\phi-B)^\alpha+A]e^{-\lambda\phi}$	0.3	20.0	3.8	9.347720e-1	17.0	100	10

Table 3.1: We summarize all the N-body simulations performed with the RAMSES code for Type-3 coupled models.

Model	γ_0	ϵ_1	ϵ_2
C*	0.3	1	1
C*1	0.3	$1-\frac{h_2-h_1}{1+h_1}a^2\frac{H}{H_0}\Delta t^n/2$	1
C*2	0.3	1	$\frac{1+h_3}{1+h_1}$

Table 3.2: The two additional simulations C*1 and C*2 consider each coefficient in the Euler equation separately, using the background evolution of model C for $\gamma_0 = 0.3$. The model C* has the background evolution of model C with $\gamma_0 = 0.3$ and $\epsilon_1 = \epsilon_2 = 1$.

γ_0 corresponds to a greater coupling, with the potential chosen for model C leading to a larger deviation from the ΛCDM case. Note that the background scalar field is effectively rescaled by the coupling term, leading to modifications of the scalar field evolution even at the background level, as seen in equation 2.39.

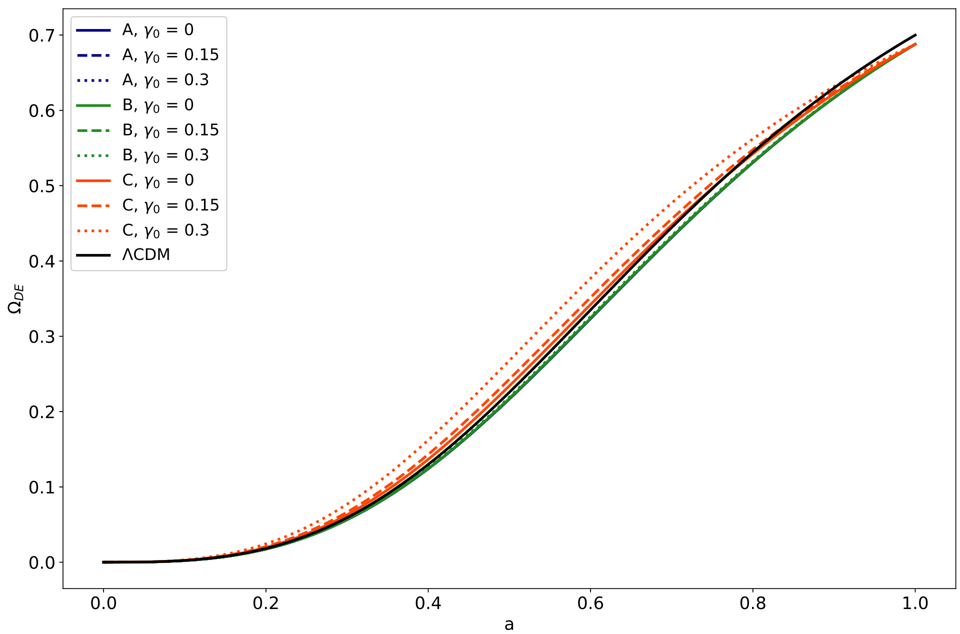

Figure 3.1: Evolution of Ω_ϕ for three coupled models summarized in Table 3.1. The models A (blue lines), B (green lines) and C (orange lines) are compared with the evolution of Ω_Λ (black line) for several values of γ_0.

The equation of state parameter w_ϕ for a quintessence model is given by equation 2.3, and is shown in Figure 3.2. For all models, w_ϕ begins with a value equal to 1, which then decays rapidly to values close to -1. This transition between $w_\phi(z \to \infty)$ and $w_\phi(z = 0)$ occurs at very high redshift, well before the starting redshift of our N-body simulations, and occurs because of the form of the chosen potential. If we observe the evolution for each value of γ_0, we see an almost identical behaviour, with separation of the models as we approach z = 0. The values of $w_\phi(z = 0)$ are given in Table 3.3. For all models we can see that a larger value of γ_0 leads to a greater deviation from ΛCDM. Within the context of ΛCDM observations are consistent with $w = -1$ [4] but this is model dependent. In our case, the evolution is given by a dynamical equation of state whose final value $w(z = 0)$, for all our models, is $w > -1$. Model C with $\gamma_0 = 0.3$ is the model that deviates the most from the ΛCDM model. This dynamical evolution of the equation of state indicates the relation between the pressure and density of dark energy, which we know dominates the present epoch. So deviations in its evolution could lead to a change in the future expansion profile. Future measurements of this parameter (from LSST for example) at higher redshift will allow us to estimate its time dependence and to distinguish between a cosmological constant or a quintessence field.

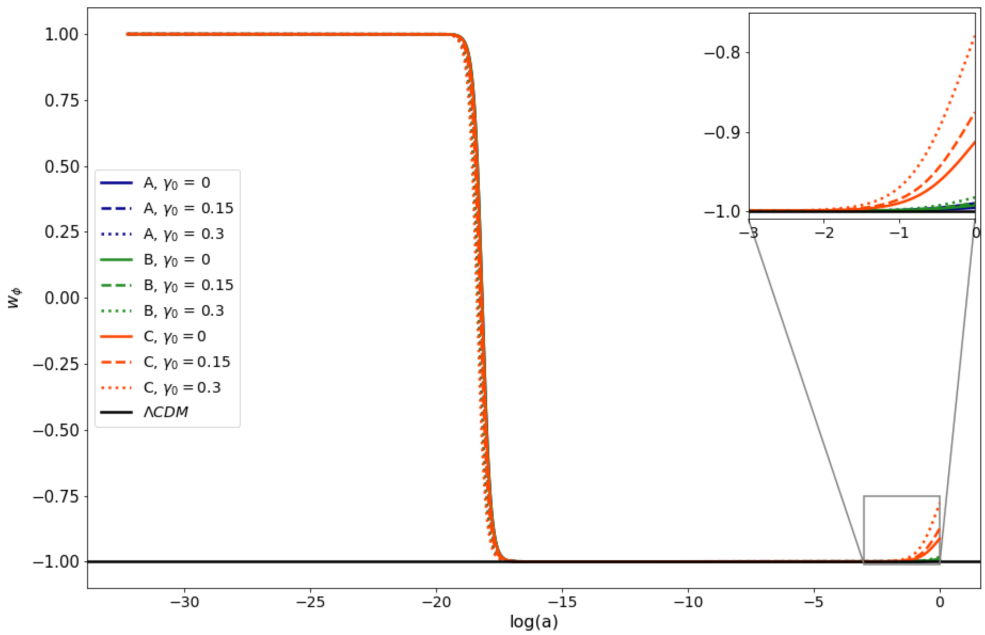

Figure 3.2: The equation of state parameter w_ϕ for models A (blue lines), B (green lines) and C (orange lines), compared with the evolution of w_Λ (black line).

To check that our models are consistent with CMB observations, we now compare the CMB temperature fluctuation power spectrum, as determined by Planck [4], assuming ΛCDM, with our models in Figure 3.3. As we can see in the figure, there are only very minor deviations in the peaks of the power spectrum, when comparing with ΛCDM, due to the slightly modified background evolution. It is worth noting, however, that the coupled quintessence models that we consider lead to CMB power spectra that are essentially identical, regardless of the potential or the coupling.

$w_\phi(z=0)$	A	B	C
$\gamma_0 = 0$	-0.996 $\pm$ 0.0	-0.993 $\pm$ 0.0	-0.913 $\pm$ 0.0
$\gamma_0 = 0.15$	-0.994 $\pm$ 0.0	-0.990 $\pm$ 0.0	-0.875 $\pm$ 0.0
$\gamma_0 = 0.3$	-0.984 $\pm$ 0.0	-0.971 $\pm$ 0.0	-0.778 $\pm$ 0.0
ΛCDM model	$w(z=0) = -1.03 \pm 0.03$		

Table 3.3: Equation of state $w_\phi(z=0)$ for our models A, B and C with different values of γ_0.

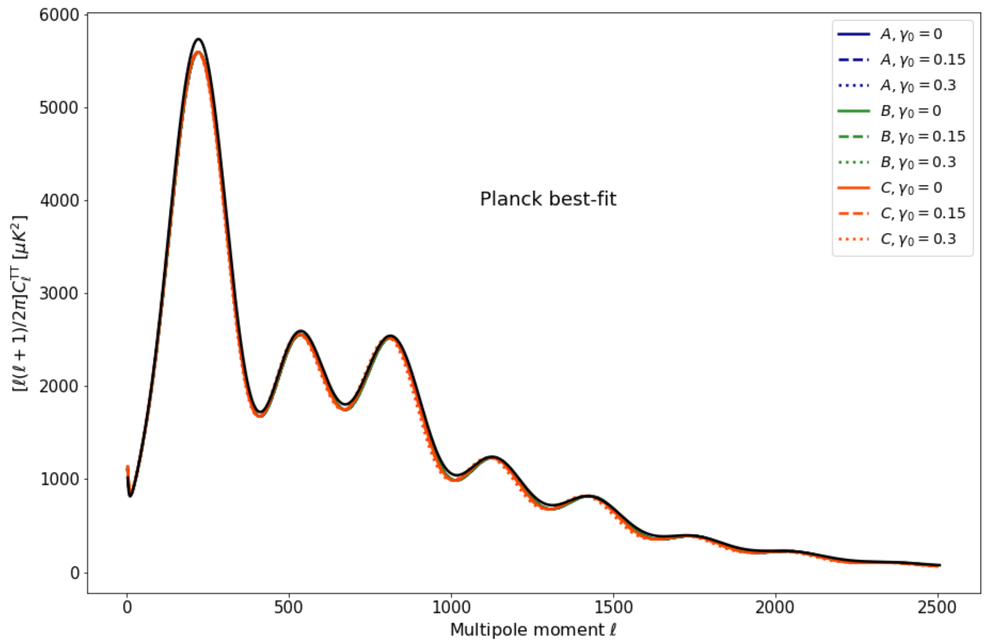

Figure 3.3: The angular power spectrum of the CMB temperature fluctuations for the best fit of the LCDM (black line) and our models (colour lines).

In order to quantitatively understand the deviation in our modified Euler equation from the uncoupled case, we focus on equation 2.44. From this equation we can directly estimate the magnitude of our modifications and how these might affect the movement of the particles. Dividing equation 2.44 throughout by the coefficient of the acceleration term, we can refer to the coefficient of the cosmological friction term as c_1 and the coefficient of the gravitational force term as c_2, that is $c_1 = \frac{1+h_2}{1+h_1}$ and $c_2 = \frac{1+h_3}{1+h_1}$.

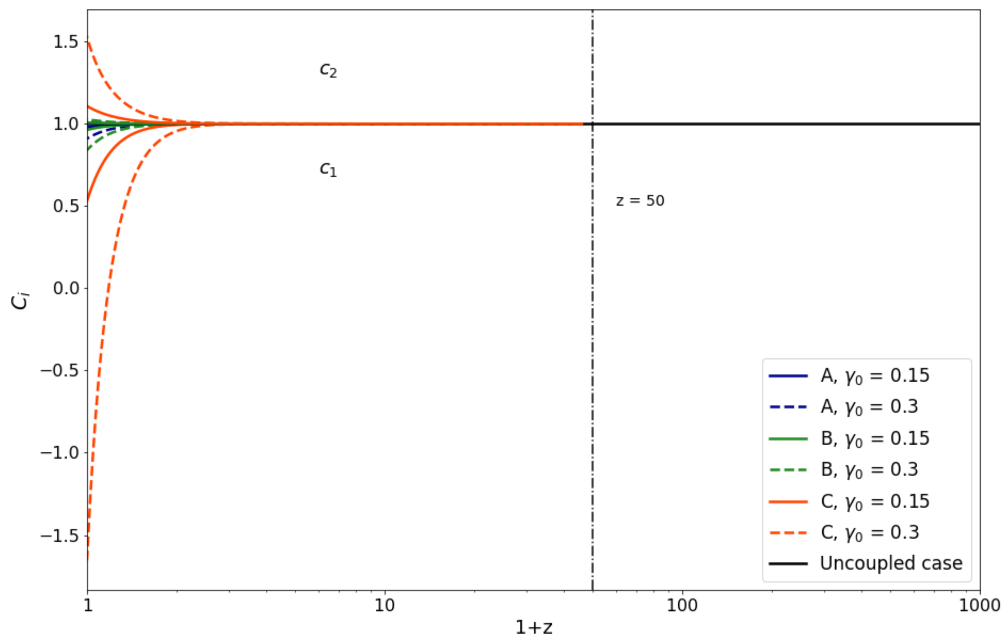

Figure 3.4: Variation of the cosmological friction (Coefficient 1) and gravitational force (Coefficient 2) coefficients.

Figure 3.4 shows the evolution of these coefficients for all our models, which we compare with the uncoupled case (i.e., with $c_1 = c_2 = 1$). We plot models A (blue lines), B (green lines) and C (orange lines), distinguishing for each value of γ_0. We summarize the deviations of our models from the standard case in Table 3.4. The cosmological friction and effective gravitational force in our models remains the same as the uncoupled case until z $\sim$ 1, indicating that the presence of the coupling only becomes relevant at low redshift. As we approach z = 0, we see a reduction in the cosmological friction, which is particularly pronounced for $\gamma_0 = 0.3$ in model C (orange dotted line) with a change to negative values and a deviation of $\sim$ 67%. Negative values of this coefficient indicate that the cosmological friction term in this model becomes a kind of forcing. For model A we see that the deviation is much smaller for all γ_0 values, being 9% for $\gamma_0 = 0.3$, while for model B the deviation reaches $\sim 16\%$ at the present time for $\gamma_0 = 0.3$. As for the evolution of c_2, we see that the general behavior is an increase in the coefficient of the gravitational force term. The variation for A reaches 0.4% for $\gamma_0 = 0.15$ and 1.5% for $\gamma_0 = 0.3$, this being the model that exhibits a smaller variation with respect to the standard case. For model B we see that the gravitational force increases by 0.7% and 2.7% for $\gamma_0 = 0.15$ and 0.3, respectively, while for model C, we see that the deviation rises significantly, reaching 53.3% for $\gamma_0 = 0.3$, being the case that most deviates from the uncoupled case. We will see later that, despite the large variation in the contribution of the cosmological friction term, it is the modified gravitational force term that has much more impact in modifying the evolution of structure.

Model	c_1 (z = 0)	% c_1	c_2 (z = 0)	% c_2
A				
$\gamma_0 = 0.15$	0.978 ± 0.0	2.2	1.004 ± 0.0	0.4
$\gamma_0 = 0.3$	0.909 ± 0.0	9.1	1.015 ± 0.0	1.5
B				
$\gamma_0 = 0.15$	0.963 ± 0.0	3.7	1.007 ± 0.0	0.7
$\gamma_0 = 0.3$	0.837 ± 0.0	16.3	1.027 ± 0.0	2.7
C				
$\gamma_0 = 0.15$	0.529 ± 0.0	47.1	1.108 ± 0.0	10.8
$\gamma_0 = 0.3$	-1.673 ± 0.0	67.3	1.533 ± 0.0	53.3

Table 3.4: Values of the coefficients of the modified Euler equation at z = 0 with the percentage of deviation from the uncoupled case ($c_1 = c_2 = 1$).

Taking into account the modifications for each model, we can analyse the consequences of these deviations on the movement of particles, as well as their possible consequences on the distribution of matter.

3.2 RAMSES runs

For all our simulations, we use the same parameters for the computational box, which are summarised in Table 3.5. From the RAMSES runs we obtain the final particle distributions for all our models. Because we used the same initial conditions, we find a similar final distribution at $z = 0$ for all our models. The projected particle density distributions at $z = 0$ for all our models are shown in Figure 3.5.

N_{part}	$M_{part}[M_\odot h^{-1}]$	Box size [Mpc h^{-1}]	Maximum spatial resolution [kpc h^{-1}]
128^3	$\sim 1.3 \times 10^9$	32	1.95

Table 3.5: Technical properties of all our simulations.

The colorbar represents the projected density in $[g/cm^3]$, thus white colors signify overdensities, while dark blue colors signify less dense regions. In all cases we observed that a large filamentary structure forms in one corner of the box, this being the largest overdense region in our simulations.

We see that there is no noticeable variation in the density distribution of our models, thus we will use the power spectrum to statistically analyze the two-point correlation of the particles, both for large and small scales.

3.3 Power spectrum analysis

We use the public code POWMES[1] [25] to measure the power spectrum of our models. This code gives us a fast and very accurate estimate of the Fourier power spectrum of a particle distribution. It is worth remembering that for all cases we have considered the same value of σ_8 in our initial conditions setup in order to analyze only the change arising from varying the coupling constant.

In Figures 3.6 and 3.7, we have plotted the power spectrum for all models, normalised by the power spectra of ΛCDM and the uncoupled models (i.e. those with the same potential but with $\gamma_0 = 0$), respectively, to analyse the effects of the coupling over a wide range of scales. We also plot in Figure 3.8 the power spectra of the models C*1, C*2 and C (all with $\gamma_0 = 0.3$) normalised by the model C* which has $\epsilon_1 = \epsilon_2 = 1$ (i.e. enforcing a standard Euler equation) but the same background evolution as the coupled model.

Our predictions on large scales may be limited by the size of the box, however, we can see in Figure 3.6 that the different background evolution in our quintessence models leads to reduced power on large scales. The fact that this is seen for all values of the coupling tells us that this effect is indeed almost entirely due to the modified background evolution as compared with ΛCDM. If we compare this behaviour with Figure 3.7, we notice that the reduced power on large scales is not present when compared to the uncoupled case. The only case that shows a reduction (although

[1] `http://www.projet-horizon.fr/article345.html`

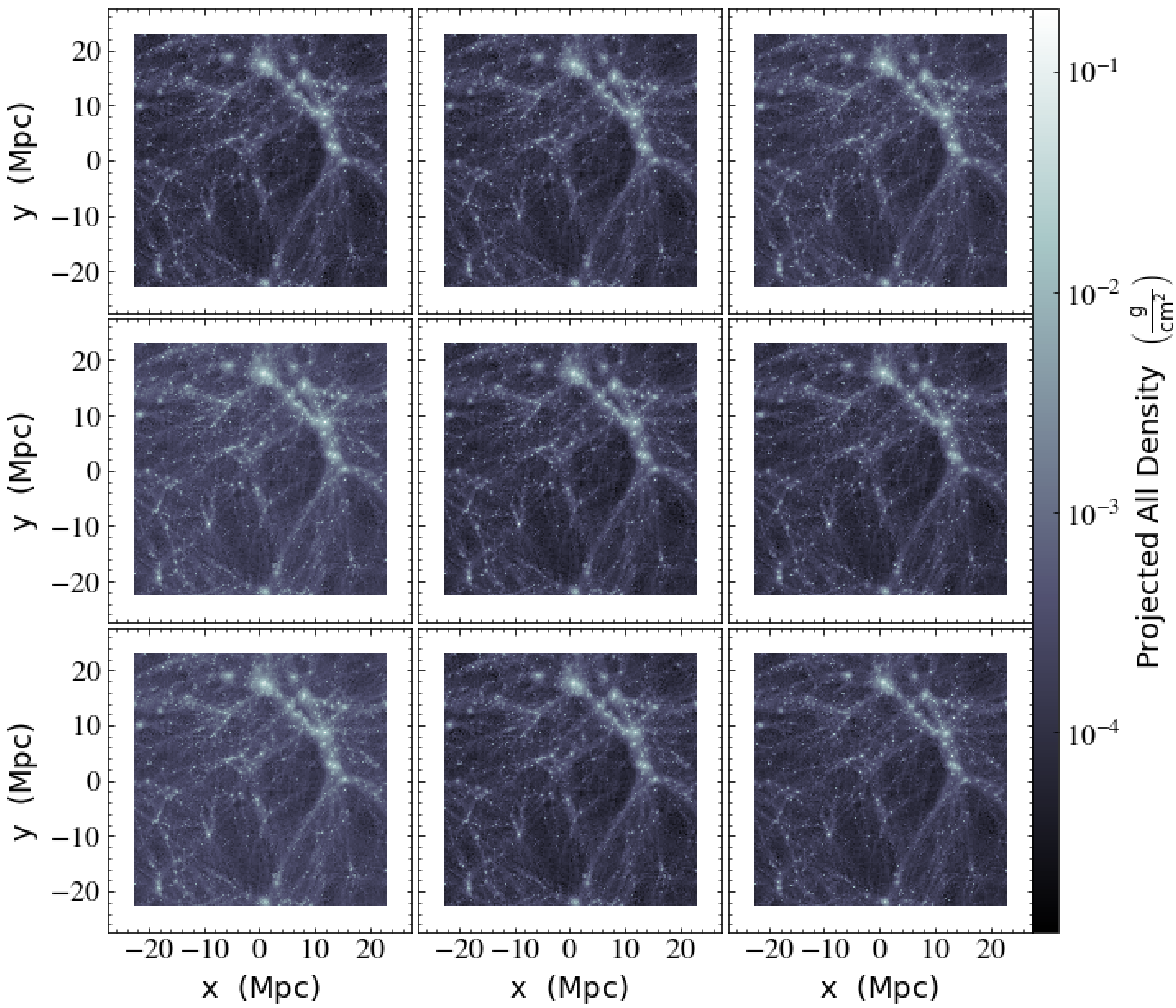

Figure 3.5: Final projected particle distribution for models A (left column), B (middle column) and C (right column) at $z = 0$. The coupling is $\gamma_0 = 0$, 0.15 and 0.3 in the top, middle and bottom rows..

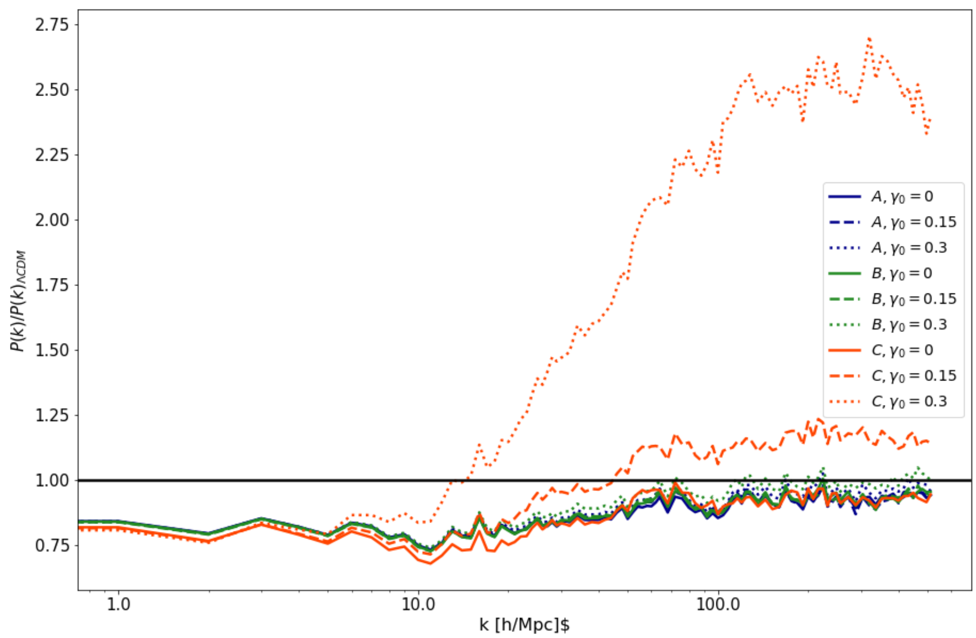

Figure 3.6: Ratio of the power spectrum of models A (blue lines), B (green lines) and C (orange lines) with respect to ΛCDM.

very minimal), is for model C with $\gamma_0 = 0.3$. This again tells us that the presence of the coupling has very little effect on these scales.

It is important to note, however, that for all our models the coupling parameter γ_0 appears in the equation of motion for the background quintessence field (2.22) and so the background evolution is modified when the coupling takes different values. This is also clear from the evolution of w_ϕ (see Figure 3.2). Therefore, we fully separate the consequences of the coupling in the Euler equation from the background evolution in Figure 3.8. In all cases shown in this figure the background evolution is identical. It is clear that the modified cosmological friction term (model C*1) plays no role in our results at large scales, with only a very small effect at smaller scales. The modified gravitational term, however, (model C*2) causes a slight increase in power at large scales, and is almost entirely responsible for the enhanced structure at smaller scales. Thus we can confirm that the reduced power on large scales for all models, compared with ΛCDM is entirely due to the modified background evolution.

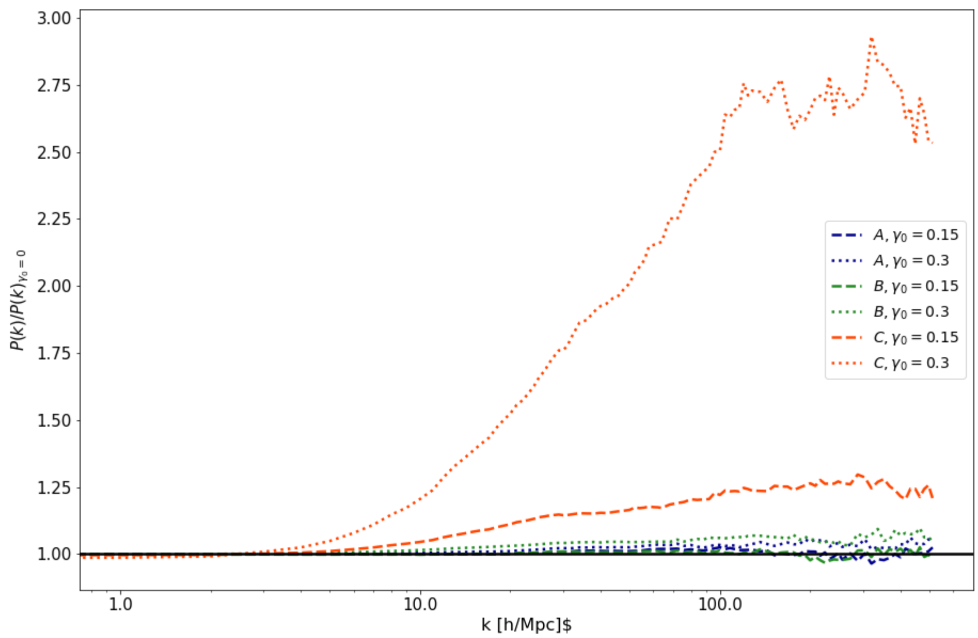

Figure 3.7: Ratio of the power spectrum of models A (blue lines), B (green lines) and C (orange lines) with respect to uncoupled case.

On small scales, comparing with ΛCDM, we see that there is enhanced structure only for model C. For models A and B there is a reduction of structure when compared with ΛCDM, most likely due to the modified background evolution, although this reduction is less notable at smaller scales, due to the increased effective gravitational force. Comparing our results for all models with those same models in the absence of coupling (Figure 3.7) we can see that at smaller scales there is an increase in the structures, becoming more pronounced for larger values of γ_0. The most significant cases are again for model C, with $\gamma_0 = 0.15$ (dashed orange line) and 0.3 (dotted orange line). In this case, the increased effective gravitational force is the key driver. This is made most clear again in Figure 3.8, where the background evolution is identical in all cases. The large increase in power on smaller scales is therefore almost entirely due to the increased effective gravitational force, with a very slight suppression of this effect coming from the modified cosmological friction. It is worth noting that the friction term is proportional to particle velocity, thus higher velocities

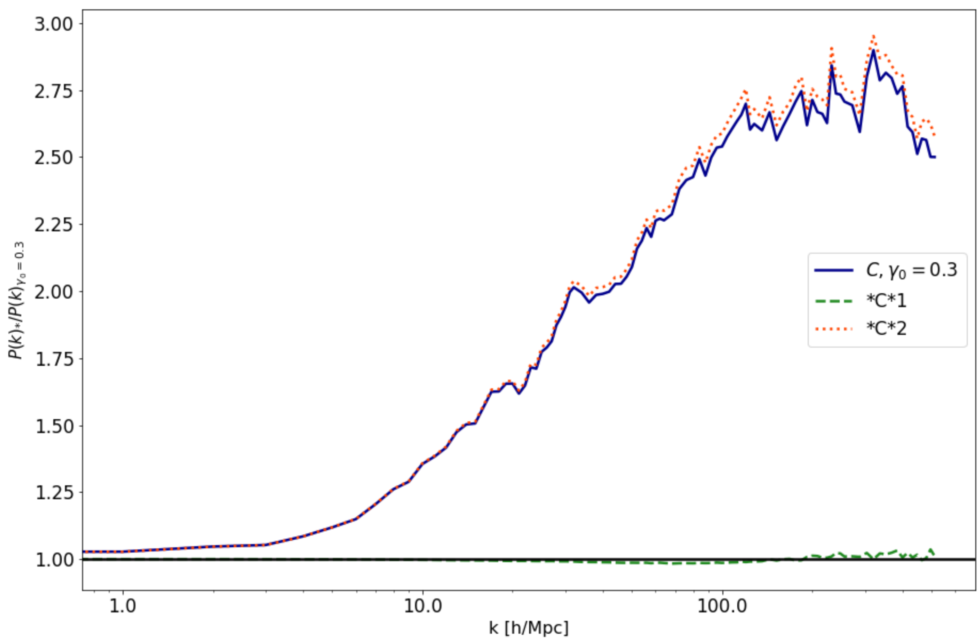

Figure 3.8: Power spectrum rate for each Euler coefficient.

due to the modified effective gravitational force lead to a larger friction effect, which, in our models, is *suppressed* relative to the uncoupled case. This explains why the model C power spectrum is somewhat more reduced at smaller scales relative to the C*2 model (gravitational coefficient only) than might be expected from the results for C*1.

It is worth noting, however, that even given the modified gravitational force term in our models, our results show that there is only a significant modification to the amount of structure formed (as summarised by the power spectrum) if the increase in the effective gravitational force is significant, on the order of 10% (as in model C with $\gamma_0 = 0.15$) or more.

Although a direct comparison is difficult, due to the different nature of the models, our results appear to be consistent with the study of [13] of a momentum transfer model that only includes a modified cosmological friction term. Specifically, we can attempt to compare with their case of a constant dark energy equation of state $w = -0.9$ (the case of phantom dark energy with $w < -1$ shows opposite behaviour and is not comparable to our study). In this case our models are roughly comparable at the background level in the sense that they all have $w > -1$ at all times. In the study of [13], for $w = -0.9$, they observe a reduction in power as compared to ΛCDM at large scales with an increase at small scales arising purely from a modified cosmological friction term and the modified background evolution. The effect in their models, however, is substantially larger than in our case. It is likely that the much reduced impact of the modified cosmological friction term in our case is due to the difference in the coupling itself, which in their model acts to *enhance* the cosmological friction, while in our case it acts to *suppress* this effect.

3.4 Dark matter halos

For the analysis of the matter distribution in our simulations, we used the Amiga Halo Finder (AHF) code [34] [38], which allows us to find gravitationally bound objects in cosmological simulations. To select which particles are inside the halo, the code applies density contours to determine the radius at which the density equals some user-defined factor of the background value (we take this to be $200\rho_c$). This radius is referred to as the virial radius R_{vir} of the halo. All gravitationally bound particles within R_{vir} are assigned to the halo, whose mass is referred to as M_{vir}. For our simulations we achieve a mass resolution of $\sim 2.59 \times 10^{10} M_\odot$, where we assign at least 20 particles to define a dark matter halo.

Since we are modifying the gravitational force in our models, we modified AHF considering an effective Gravitation constant G*, which comes from the multiplication of G with our values of c_2 at z = 0, given in Table 3.6.

Model	G* [A]	G* [B]	G* [C]
$\gamma_0 = 0.15$	4.319 $\times 10^{-9}$	4.333 $\times 10^{-9}$	4.765 $\times 10^{-9}$
$\gamma_0 = 0.3$	4.366 $\times 10^{-9}$	4.419 $\times 10^{-9}$	6.594 $\times 10^{-9}$
ΛCDM model	4.300 $\times 10^{-9}$		

Table 3.6: The effective Gravitational constant G* of our models. All these quantities are expressed in Mpc km^2/M$_\odot s^2$.

The fact that we are considering a model with the presence of momentum exchange, with a decrease in the cosmological friction term and an increase in the gravitational force indicates a modification of the velocity with which the particles move. These particles will belong to a halo if their velocity is lower than the escape velocity, i.e. $v < v_{esc}$, where

$$v_{esc} = \sqrt{2|\varphi|} \tag{3.1}$$

and

$$\frac{d\varphi}{dr} = \frac{GM(r)}{r^2} \tag{3.2}$$

with r the radius from the halo center and $M(r)$ the mass inside the halo. This way the code uses the Newton force law. In our case, equation 3.2 includes the modification of the gravitational force term in our models given in Table 3.6.

3.4.1 Halo mass function

We calculate the halo mass function using the M_{vir} of all dark matter halos for each value of γ_0 in our models, which we show in Figure 3.9. We have used the *colossus*[2] package to compare our results with an analytical HMF fitting function defined in [69]. This definition is derived from halos identified in simulations using the spherical overdensity (SO) method, which agrees with the method used by the AHF code.

We can infer from Fig 3.9, that a variation in the value of the coupling constant γ_0 does not directly affect the general behaviour of the mass function of the halos, showing a good fit in the mean mass range. Due to the limited volume and mass resolution of our simulations, we can only effectively resolve halos in the mass range of 10^{11} - 10^{13} $M_\odot$, which leaves us without information about structures with smaller masses ($< 10^{10} M_\odot$). At higher mass scales we also do not match the reference halo mass function due to the small sample of massive halos present in our models. An increase in the box size and an increase in the mass resolution, would allow us to resolve halos for a wider range of masses. The disagreements with the halo mass function at low and high masses appear to be largely unrelated to the coupling, with reasonable agreement in the HMF for all models in the intermediate mass range. We also consider simply the total number of halos found at z = 0 given in Table 3.7. For models A and B we find that for both $\gamma_0 = 0.15$ and $\gamma_0 = 0.3$ the difference compared to the uncoupled case is less than 1%, showing no variance due to the coupling constant. While for model C, there is a variation of about 1% and 5% for $\gamma_0 = 0.15$ and 0.3 respectively. This increase, although small, is produced as a consequence of the modified gravitational force experienced by the dark matter particles, showing greater efficiency in the formation of bound structures, as for model C there is an increase of 53% in the effective force compared to the uncoupled case.

[2] `https://bdiemer.bitbucket.io/colossus/cosmology_cosmology.html`

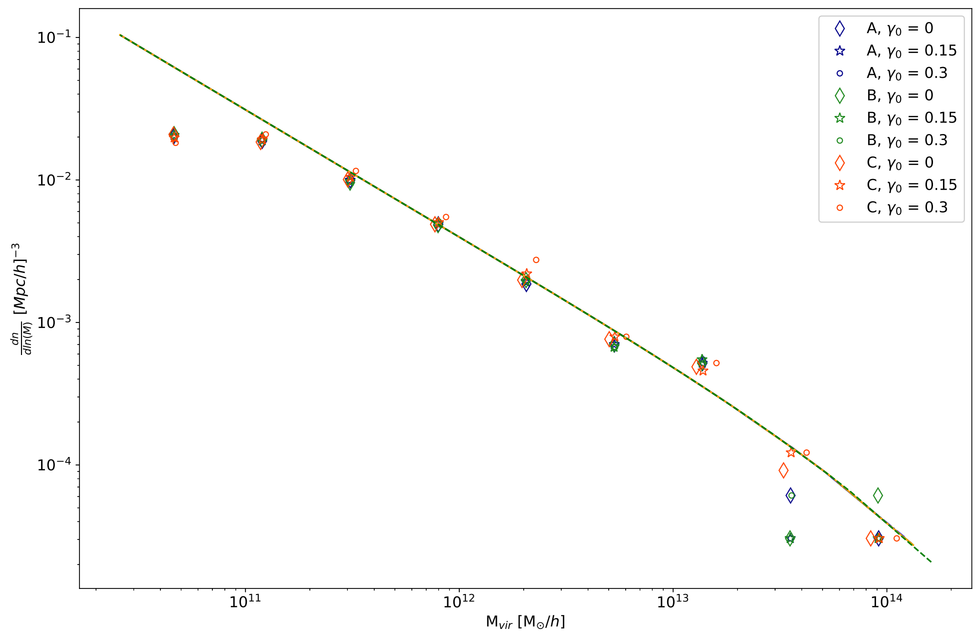

Figure 3.9: Halo mass functions for models A (blue), B (green) and C (orange).

3.4.2 Halo density profiles

To analyse the density profile we consider 2 halos with different masses (of the order of 10^{14} and 10^{13} $M_\odot$) for each model, identifying the particles inside each one, being a total of 18 halos which are summarized in the Table 3.8. This selection was made in order to analyse the density profile for both massive and less massive halos. The halo we refer to as halo 1 represents the most massive halo of each simulation which has a number of particles of about $\sim 10^5$, while halo 2, represents a less massive halo with a total of $\sim 1.3 \times 10^4$ particles. The selection of these halos across the simulations was based on them having similar masses and positions within the computational volume.

The Figures 3.10 and 3.11 show the density profile for halo 1 and halo 2 respectively, separated into three panels: in the left panel we have model A with $\gamma_0 = 0$, 0.15 and 0.3; and the same for model B (middle), and model C (right panel).

As we can see in Figures 3.10 and 3.11, models A and B do not show any difference in their density profiles with a change in the coupling constant. In fact,

Models	γ_0	A	B	C
Number of halos at z=0	0	1875	1894	1888
	0.15	1886	1884	1905
	0.3	1884	1876	1979

Table 3.7: Total number of halos at z = 0 obtained with AHF.

Halo ID	Model	γ_0	N_{subs}	N_{part}	M_{halo} $[M_\odot/h]$
Halo 1	A	0	26	101927	1.319×10^{14}
		0.15	22	101594	1.315×10^{14}
		0.3	26	102318	1.324×10^{14}
Halo 1	B	0	24	101218	1.310×10^{14}
		0.15	22	101271	1.310×10^{14}
		0.3	27	103161	1.335×10^{14}
Halo 1	C	0	25	93331	1.208×10^{14}
		0.15	22	102655	1.328×10^{14}
		0.3	36	124598	1.612×10^{14}
Halo 2	A	0	7	13281	1.719×10^{13}
		0.15	6	13343	1.727×10^{13}
		0.3	6	13382	1.732×10^{13}
Halo 2	B	0	6	13124	1.698×10^{13}
		0.15	7	13067	1.691×10^{13}
		0.3	6	13497	1.747×10^{13}
Halo 2	C	0	3	13478	1.744×10^{13}
		0.15	6	13150	1.702×10^{13}
		0.3	3	16069	2.080×10^{13}

Table 3.8: Halos selected for density profile analysis.

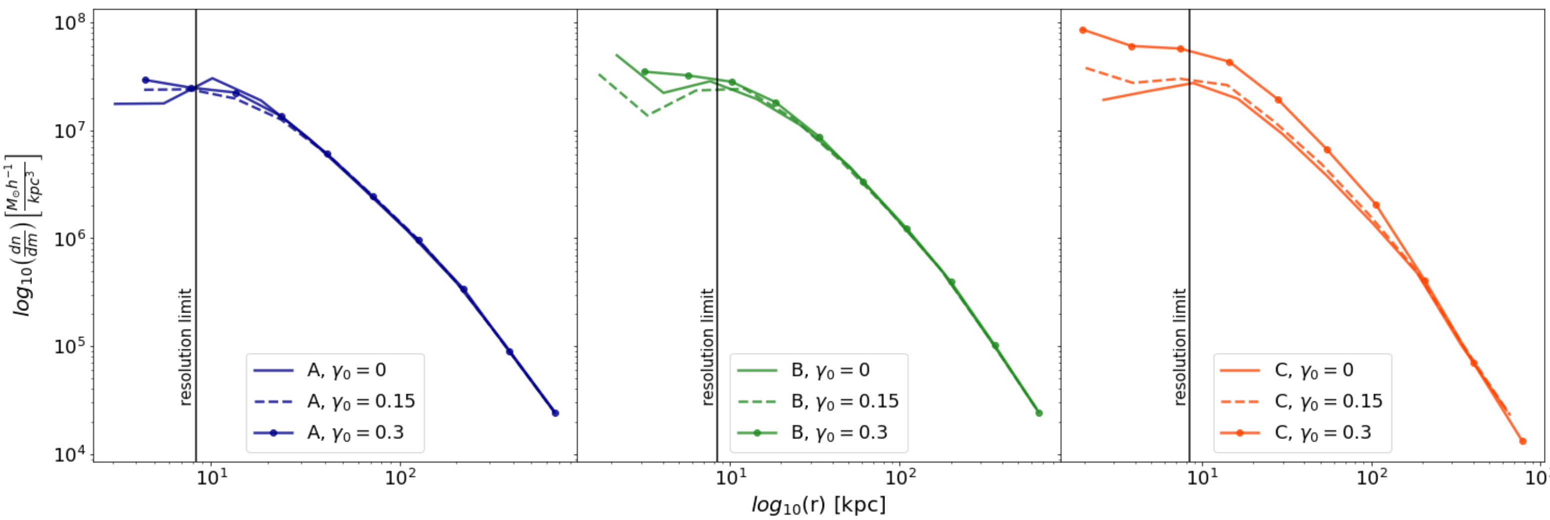

Figure 3.10: Density profile for halo 1.

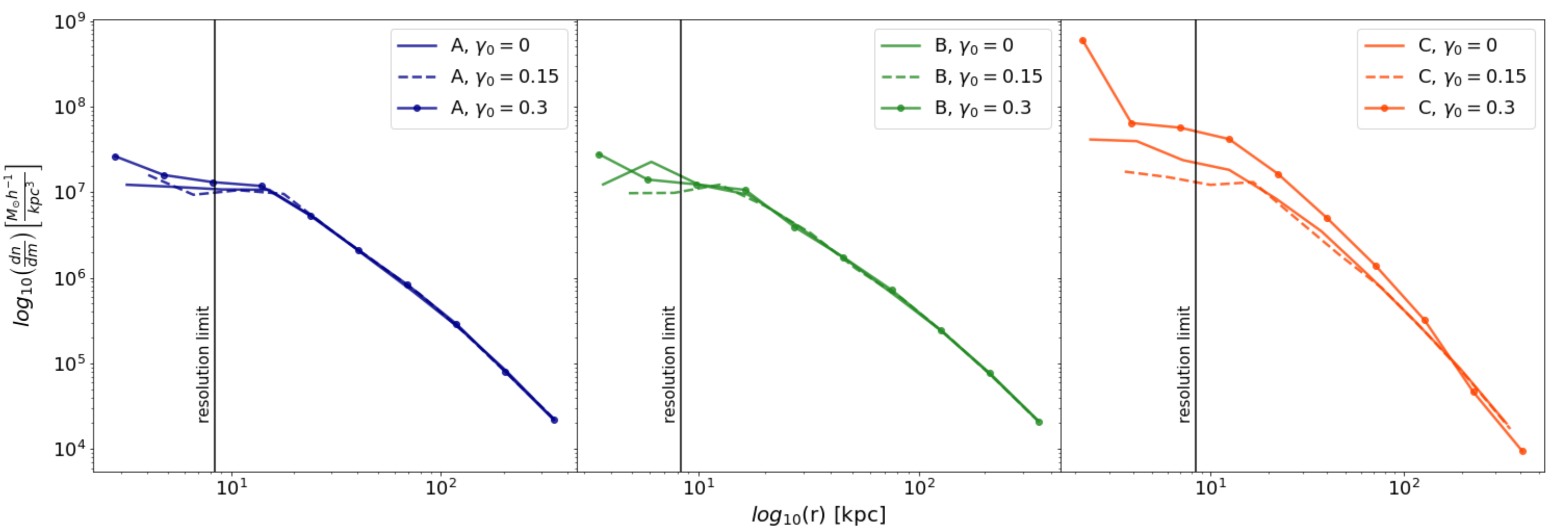

Figure 3.11: Density profile for halo 2.

at radii greater than $\sim$ 50 kpc, the density profiles for each value of γ_0 seem to be almost identical. For model C instead, we see that an increase in the coupling constant causes an increase in the inner density of the halos, leading to more cuspy halos as γ_0 increases. As in models A and B, we also observe coincidence in the profile of the three values of γ_0, however for model C, we find this similarity only in the outer regions of the halo. The fact that we have an increase for $\gamma_0 = 0.3$ may also be in part attributed to the halo selection, because both the halos selected in this case are more massive than those selected for smaller values of γ_0. The increased slope of the profile in the inner regions is, however, not simply a result of the increased mass of the halo.

We can see from Figure 3.12 the individual behaviour of each coefficient on the density profiles. For this plot we have again selected the most massive halos, this time from the simulations described in Table 3.2. The density profile for the model C*2 (orange solid line) is significantly enhanced in the inner region as compared with the other models. There is no such obvious difference in the profiles for the models C*1 and C*. This shows that the modified gravitational force term alone is responsible for the increased inner halo density. In Figure 3.12 we also show the fitted NFW halo profiles using the parameters determined by AHF. Using these fitted profiles we see a slight increase in the inner density for the model C*1, which only includes the modified cosmological friction term (suppressed in our models, relative to the uncoupled case). Physically this makes sense as a suppression of cosmological friction allows the background expansion to more effectively counteract the gravitational collapse.

Comparing our density profile results with those of the power spectrum, we see that the increased small-scale structure of model C is consistent with these increased halo densities.

In the case of radii smaller than ~ 10 kpc, we see for the three models the same flatness of the density profiles. We attribute this behaviour to the resolution of our simulations, as the maximum refinement level corresponds to grid cells with a size of 1.95 kpc h^{-1}. Increasing the resolution in our simulations would help us to better investigate the behaviour in the inner region of the density profile.
In the case of halo 2, we see the same behavior shown above for the models A and B where the density profile for each value of γ_0 seems to be the same, at least for radii greater than ~ 50 kpc. For model C, we see differences for different values of γ_0 as for halo 1, nevertheless, if we compare the density profiles for $\gamma_0 = 0$ and 0.15 we see that these profiles are not easily separated (as was also seen for halo 1), indicating that these values of the coupling have little effect on the halo profile. For $\gamma_0 = 0.3$, we see a significant increase in the halo density profile (again we note that the mass of halo 2 for this value of γ_0 is larger, but there is agreement in the outer profile).

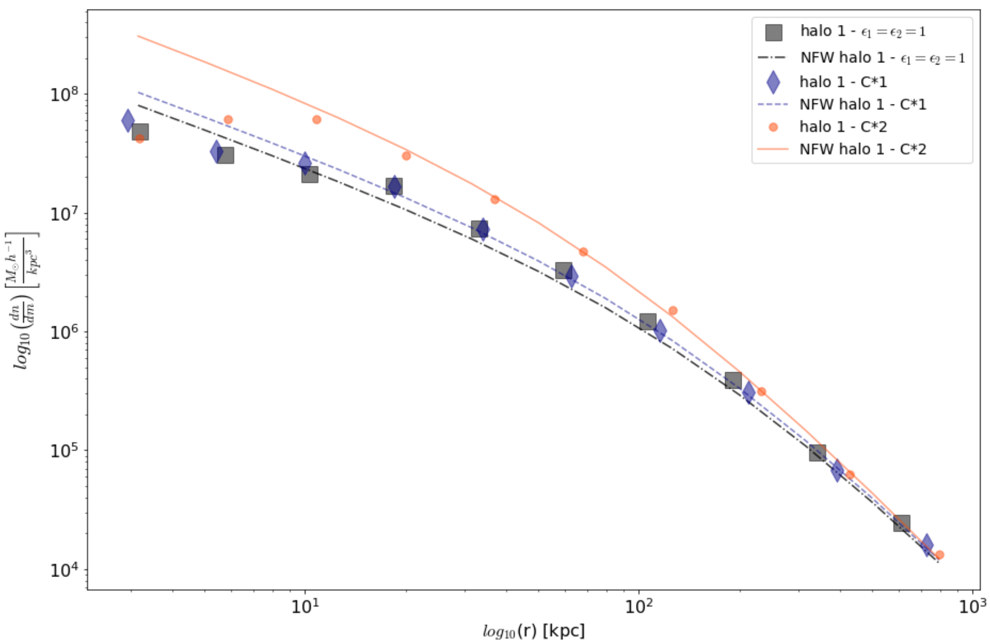

Figure 3.12: Density profile for halo 1 from each Euler coefficient contribution.

As described earlier, we now compare the density profiles shown above with an NFW profile, using the virial mass and concentration parameter obtained from AHF for each halo.

The Figure 3.13 shows the models A (blue), B (green), and C (orange), for each value of γ_0, being $\gamma_0 = 0$, 0.15, and 0.3 from left to right, where the dashed and dotted lines represent the NFW density profile for halo 1 and halo 2 respectively. As we can see in the figure, models A and B show some deviation from the NFW profile over intermediate radii, which can be seen for both halo 1 and halo 2. In the very center of the halos, where resolution effects become relevant, there is no agreement with the analytic NFW fit. For model C, we see a good fit for $\gamma_0 = 0$ and 0.15, with deviations only near the center of the halo, due to the aforementioned resolution effects. For $\gamma_0 = 0.3$ we see that for both halo 1 and halo 2, the fit of the NFW profile deviates from our model over a wider range of radii reaching a good fit only at the edge of the halo, further supporting our previous results that the large coupling in this model appears to increase the central density and leads to a more

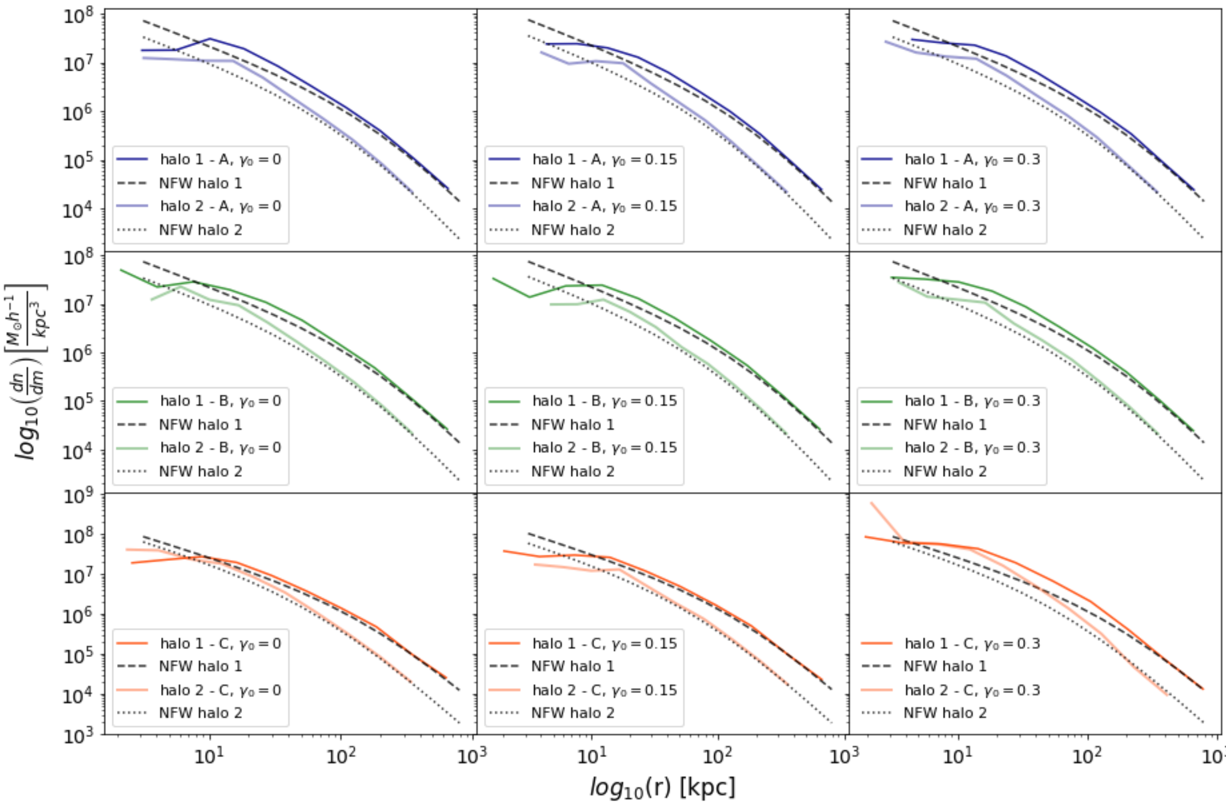

Figure 3.13: NFW profiles for selected halos from Table 3.8.

cuspy profile.

3.5 Velocity dispersion

The velocity dispersions (σ_v) for each model are shown in Figures 3.14, 3.15 and 3.16, for models A, B and C, respectively. Each figure is separated by mass range: low mass (left panel), medium mass (middle panel) and high mass (right panel) as defined by the axis ranges in the plots. We have also separated by values of γ_0, leaving the uncoupled case in the upper panel, $\gamma_0 = 0.15$ in the middle panel and $\gamma_0 = 0.3$ in the lower panel. The red line in the figures represents the linear regression best fit which are compared across models in Figure 3.17. The errors of these fits are given in the Table 3.9.

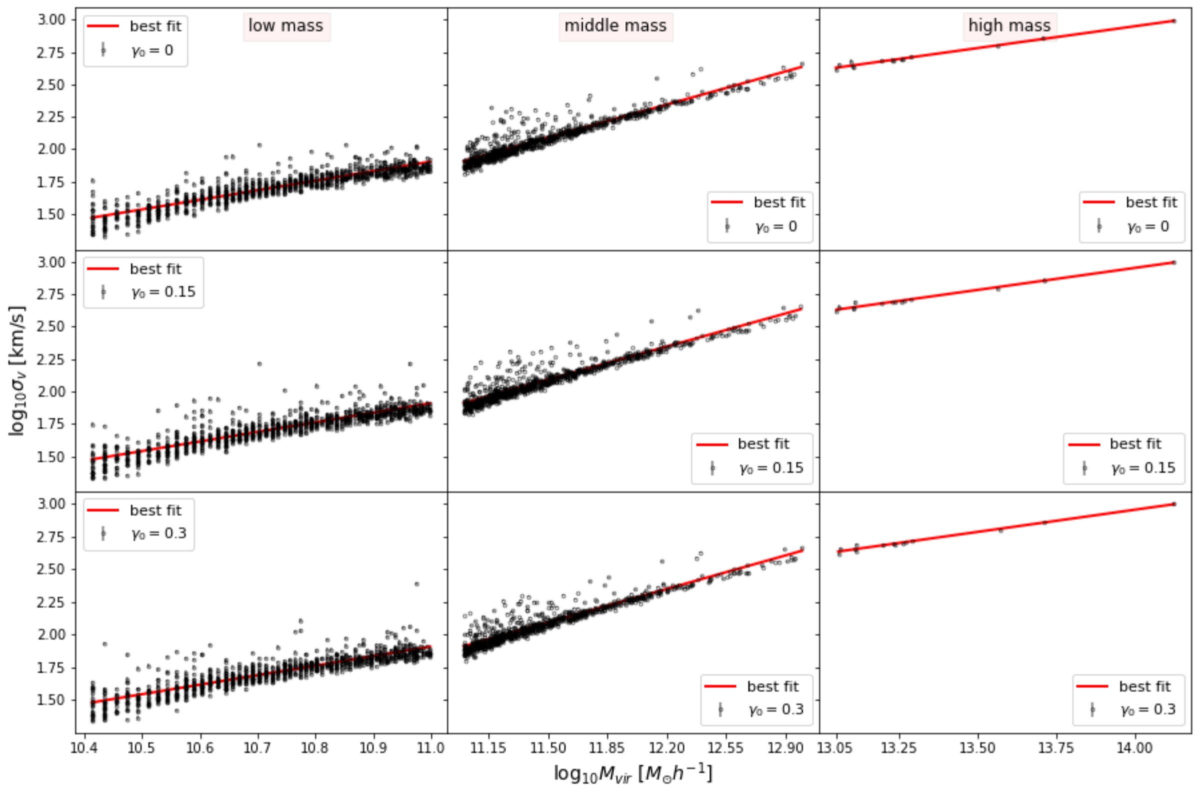

Figure 3.14: Velocity dispersion for model A.

We find no significant differences in the plots for models A and B because the variations in σ_v between the values of $\gamma_0 = 0$ and 0.15 are below 1%, while for $\gamma_0 = 0.3$, the increase in velocity dispersion due to coupling is just around 1% for low, medium and high masses. For model C, on the other hand, it is evident that the largest velocity dispersion occurs for $\gamma_0 = 0.3$ (green line). The coupling produces a higher average velocity dispersion than the uncoupled case, with an increase of 19%, 24% and 27% for low, medium and high masses, respectively. While for $\gamma_0 = 0.15$ (red line), the increase is only 4.3%, 4.37% and 5.3%. We have already seen that it is

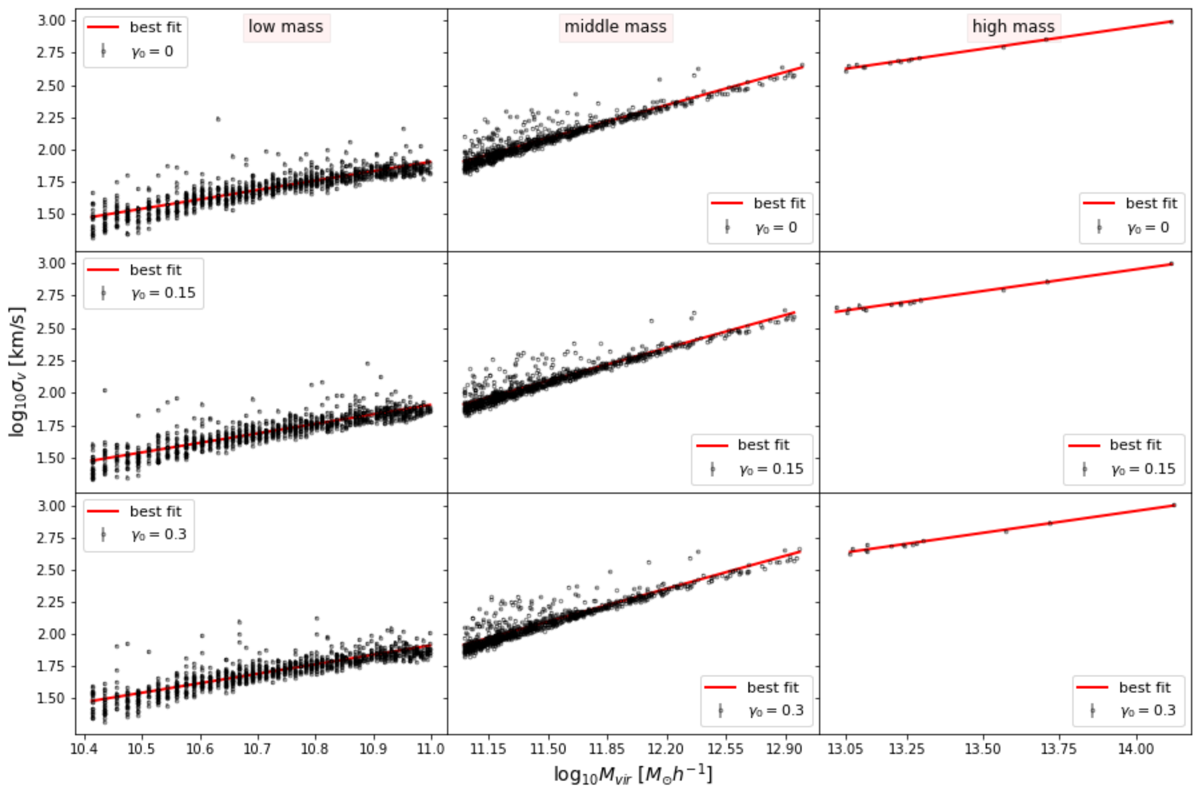

Figure 3.15: Velocity dispersion for model B.

the modified gravitational force term that is primarily responsible for the differences in our models at large coupling. This term deviates from the uncoupled case by $< 3\%$ for models A and B, whereas for model C the deviation exceeds 10% and 50% for $\gamma_0 = 0.15$ and 0.3. Thus we expect a larger increase in the velocity dispersion as a function of mass in these models.

To determine the statistical significance of the deviations in the velocity dispersions, with respect to the uncoupled case, we apply a Welch's t-test which is summarized in Table 3.10. To do this we assume the null hypothesis that the variances are equal. For the A and B models we found that in all the mass ranges, there is no significant variation that allows us to distinguish one sample from another.

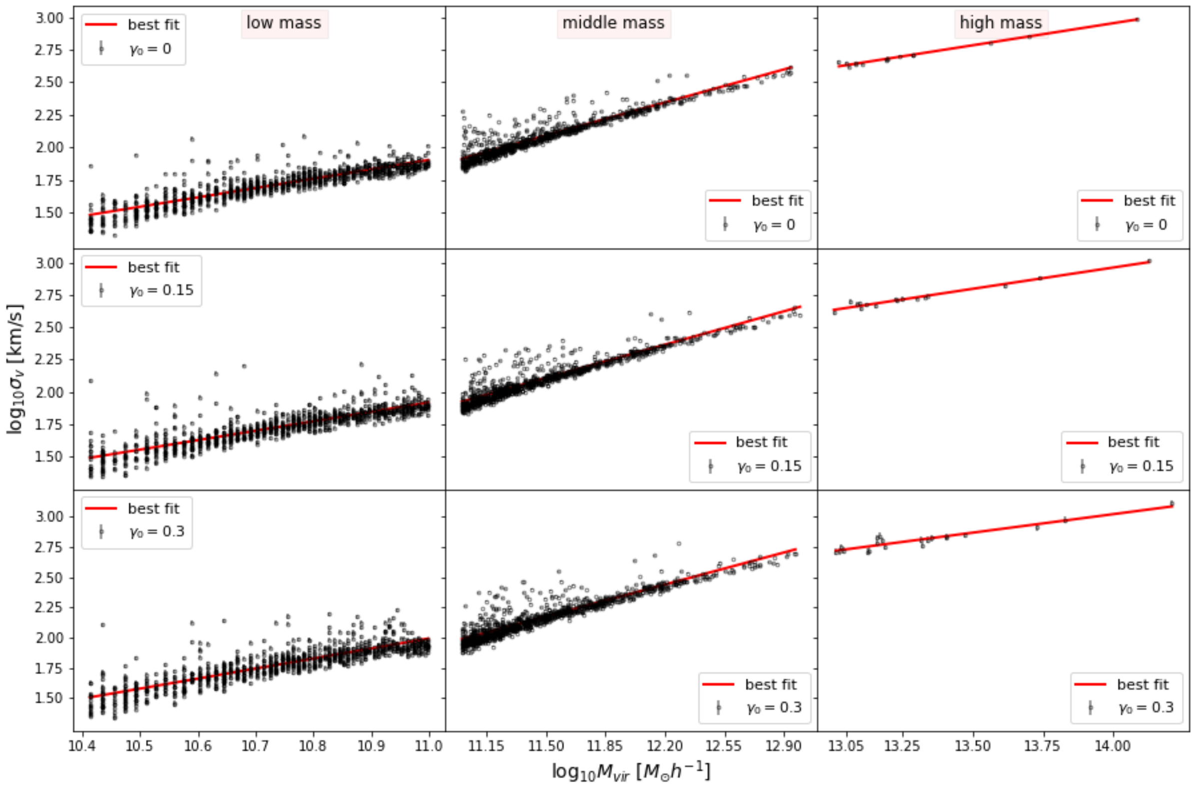

Figure 3.16: Velocity dispersion for model C.

In fact, reviewing the velocity dispersions given in the Table 3.9, we see that the variances for each case do not vary enough to show a significant statistical difference. For model C instead, we see that for both low and medium masses the data show that these samples are statistically different within 90% confidence for $\gamma_0 = 0.15$ and 99.8% for $\gamma_0 = 0.3$. For high masses, we found that for $\gamma_0 = 0.3$ the samples are statistically different within 90% confidence, which does not occur for $\gamma_0 = 0.15$, where we see an increase in the t-test value, which indicates that these samples are not statistically different, however, we had seen that the average velocity dispersion increased by 5.3% with respect to the uncoupled case.

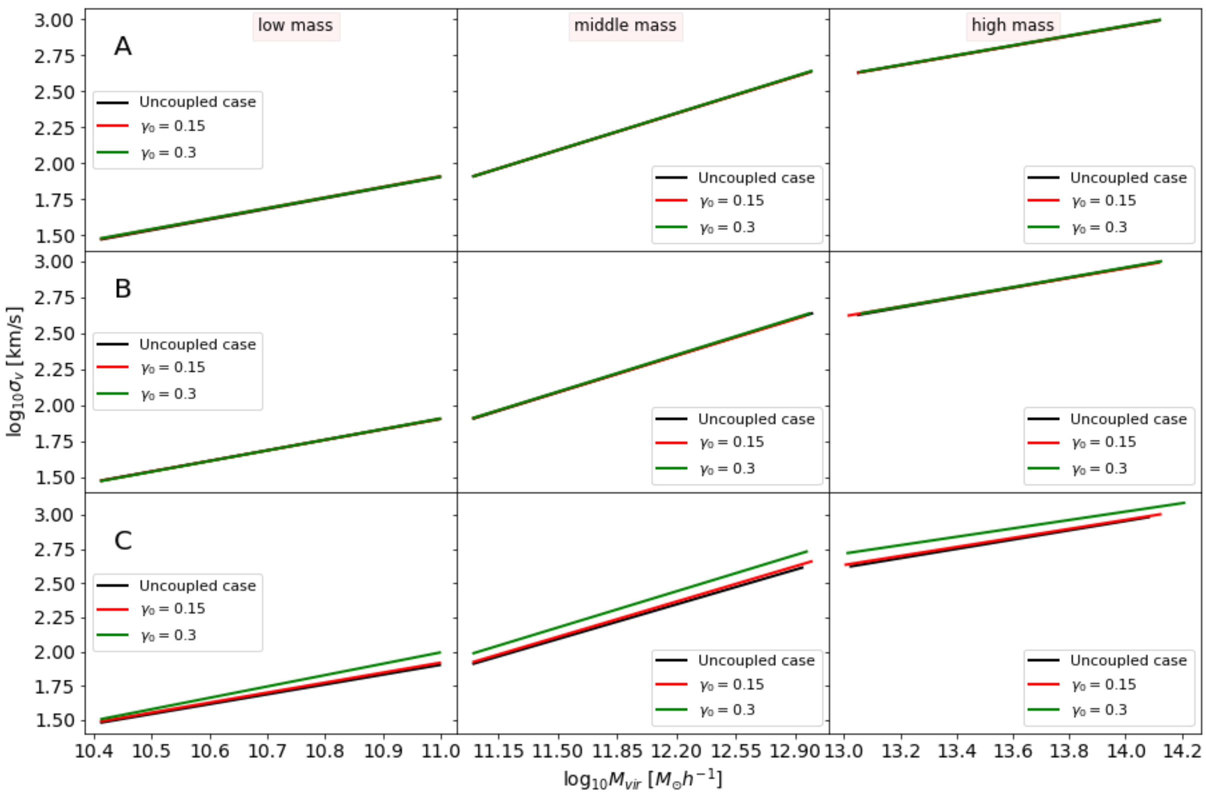

Figure 3.17: Linear regression comparison for velocity dispersion.

3.6 Particle velocity distribution

We have studied the velocity distribution of dark matter halos, both the hosts and the subhalos, giving us an idea of the effect of the coupling on virialised structures. However, this effect can be studied in more detail by analysing the velocity distribution of the particles within the halos. For this, we have selected three halos from model C (considering $\gamma_0 = 0$ and 0.3) with different masses to see the consequences of the coupling on their constituent particle velocity distributions. The information of the halos is summarized in Table 3.11.

As we can see in Figure 3.18, the distribution within the low mass halo (left

Model		$f(x)$								
		i.- $< 10^{11} M_\odot$			ii.- $10^{11} - 10^{13} M_\odot$			iii.- $> 10^{13} M_\odot$		
		m	σ_i	σ^2	m	σ_i	σ^2	m	σ_i	σ^2
A	γ_0	0.739	0.011	20.376	0.365	0.004	22.201	0.338	0.012	28.082
	$\gamma_{0.15}$	0.738	0.012	20.357	0.364	0.004	22.209	0.340	0.012	28.087
	$\gamma_{0.3}$	0.729	0.012	20.355	0.366	0.004	22.195	0.340	0.012	28.090
B	γ_0	0.727	0.012	20.354	0.365	0.004	22.195	0.343	0.009	28.082
	$\gamma_{0.15}$	0.732	0.012	20.358	0.362	0.004	22.193	0.332	0.014	27.999
	$\gamma_{0.3}$	0.738	0.012	20.359	0.365	0.004	22.184	0.340	0.013	28.100
C	γ_0	0.718	0.012	20.363	0.362	0.004	22.195	0.340	0.011	27.969
	$\gamma_{0.15}$	0.730	0.014	20.311	0.368	0.004	22.124	0.329	0.016	27.964
	$\gamma_{0.3}$	0.830	0.016	20.103	0.378	0.004	21.842	0.306	0.024	27.622

Table 3.9: The table shows the best fits for models A, B and C separated by mass range, using a linear regression fit of the form $y = mx + c$, where m is the slope, σ_i is the standard error at the intercept (c) and σ^2 is the variance.

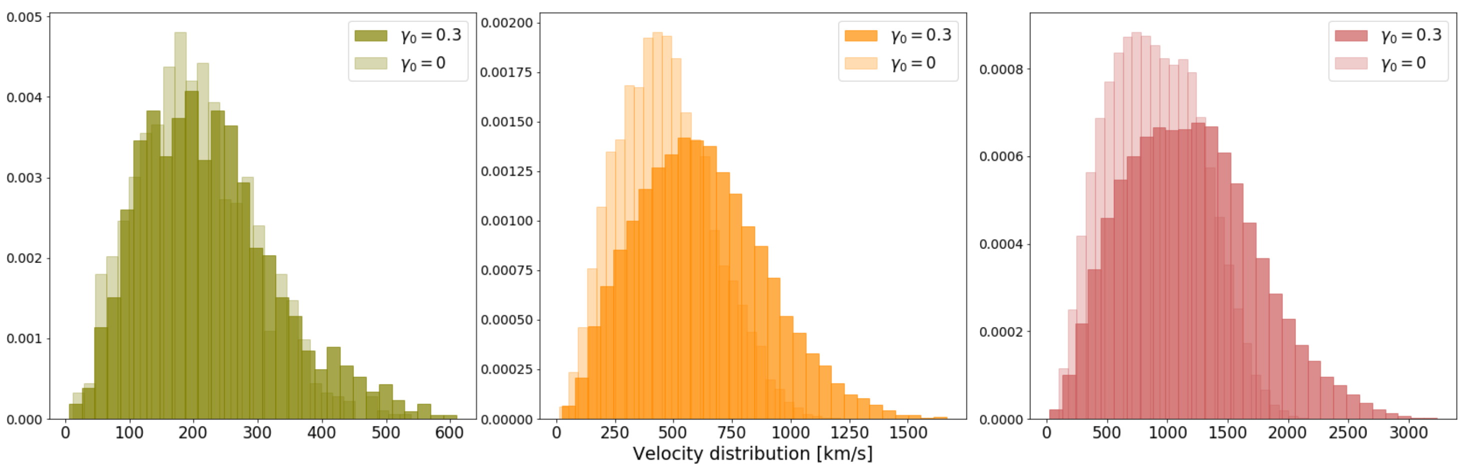

Figure 3.18: Particle velocity distribution.

panel) seems to be similar when comparing coupled to uncoupled, while for the medium (middle panel) and high mass halos (right panel), an increase in the coupling constant leads to a shift of the distribution to higher velocities.
For the selection of this sample, we have considered those halos with similar masses

Model A	t-test	p-value	DF	CL 60%	CL 90%	CL 98%	CL 99.8%
i.- $\gamma_0/\gamma_{0.15}$	0.993	0.321	1969	1.282	1.96	2.576	3.291
i.- $\gamma_0/\gamma_{0.3}$	1.009	0.313	1941	1.282	1.96	2.576	3.291
ii.- $\gamma_0/\gamma_{0.15}$	0.280	0.780	1755	1.282	1.96	2.576	3.291
ii.- $\gamma_0/\gamma_{0.3}$	0.254	0.800	1769	1.282	1.96	2.576	3.291
iii.- $\gamma_0/\gamma_{0.15}$	0.032	0.975	26	1.315	2.056	2.779	3.707
iii.- $\gamma_0/\gamma_{0.3}$	0.108	0.915	26	1.315	2.056	2.779	3.707
Model B	t-test	p-value	DF	CL 60%	CL 90%	CL 98%	CL 99.8%
i.- $\gamma_0/\gamma_{0.15}$	0.613	0.540	1983	1.282	1.96	2.576	3.291
i.- $\gamma_0/\gamma_{0.3}$	0.876	0.381	1959	1.282	1.96	2.576	3.291
ii.- $\gamma_0/\gamma_{0.15}$	0.144	0.885	1761	1.282	1.96	2.576	3.291
ii.- $\gamma_0/\gamma_{0.3}$	0.728	0.467	1776	1.282	1.96	2.576	3.291
iii.- $\gamma_0/\gamma_{0.15}$	-0.026	0.980	27	1.314	2.052	2.771	3.689
iii.- $\gamma_0/\gamma_{0.3}$	0.201	0.842	26	1.315	2.056	2.779	3.707
Model C	t-test	p-value	DF	CL 60%	CL 90%	CL 98%	CL 99.8%
i.- $\gamma_0/\gamma_{0.15}$	3.080	0.002	1888	1.282	1.96	2.576	3.291
i.- $\gamma_0/\gamma_{0.3}$	11.693	2.45e-30	1560	1.282	1.96	2.576	3.291
ii.- $\gamma_0/\gamma_{0.15}$	2.100	0.036	1813	1.282	1.96	2.576	3.291
ii.- $\gamma_0/\gamma_{0.3}$	10.656	8.48e-26	1921	1.282	1.96	2.576	3.291
iii.- $\gamma_0/\gamma_{0.15}$	0.519	0.610	29	1.311	2.045	2.756	3.66
iii.- $\gamma_0/\gamma_{0.3}$	2.595	0.014	34	1.31	2.042	2.75	3.646

Table 3.10: Welch's t- test for velocity dispersion. lm: low mass, mm: middle mass, hm: high mass, DF: degree of freedom.

and similar locations within the dark matter halo distribution, in order to be able to make a better comparison between each simulation. For the case of the halo of mass $\sim 10^{12}$ $M_\odot$, we found an increase of 0.7% in both mass and number of particles in the coupled case, compared to the uncoupled model. For the medium mass halo, the increase was 23%, while for the high mass halo we saw an increase of 25% compared to the uncoupled case. Although these differences in mass will also lead to differences in the velocity distribution, the effects we see here are considerably larger than that expected from the mass variation, and are fully consistent with the increased velocity dispersion discussed in the previous section. This thus indicates that an increase in coupling leads to an increase in particle velocity, which in turn leads to enhanced structure formation as well as a population of higher velocity particles within those

Halo ID	γ_0	N_{subs}	N_{part}	M_{halo} $[M_\odot/h]$
Halo 1	0	0	1042	1.35×10^{12}
	0.3	1	1050	1.36×10^{12}
Halo 2	0	4	14956	1.94×10^{13}
	0.3	5	19639	2.54×10^{13}
Halo 3	0	25	93331	1.21×10^{14}
	0.3	36	124598	1.61×10^{14}

Table 3.11: Halos selected from model C for analysis of their velocity distributions.

structures.
Regarding the low mass halo, it is worth keeping in mind that this result could be due to the number of particles composing the halo, which is possibly too low for clear analysis of the coupling effects. An increase in the resolution and number of particles could help us to study this effect in more detail at low mass scales.

From the simulations where we have separated the effects of each Euler coefficient (3.2), we have selected the most massive halo from each one (see 3.12) and analysed the velocity distribution of the particles within each halo, which we show in Figure 3.19.

Model	N_{subs}	N_{part}	M_{halo} $[M_\odot/h]$
C	36	124598	1.612×10^{14}
C*1	29	94263	1.220×10^{14}
C*2	37	124411	1.610×10^{14}

Table 3.12: Selected halos for each Euler coefficient contribution to model C.

We found that the velocity distribution for the full model C (grey) which contains the contribution of both coefficients, is almost identical to the case containing only the contribution of the modified effective gravitational force (purple). This scenario reinforces the idea that this term is the predominant one in the model, leading to an increase in particle velocities. The velocity distribution for the model C*1 (light blue) shows a smaller dispersion compared to the full model C, indicating that the cosmological friction term does not affect the velocity distribution, whose behaviour is very similar to that obtained for the model C* (yellow), where no coupling is present in the Euler equation. This lower dispersion leaves velocities in the range $0 - 2000$ km/s, the mean being 822 km/s. For the C*2 model instead, we see that the particle velocity distribution has a wider range of $0 - 3000$ km/s (as in the full model C) with a mean of 1193 km/s, slightly higher than the mean of the halo of the full model, which has a mean of 1189 km/s.

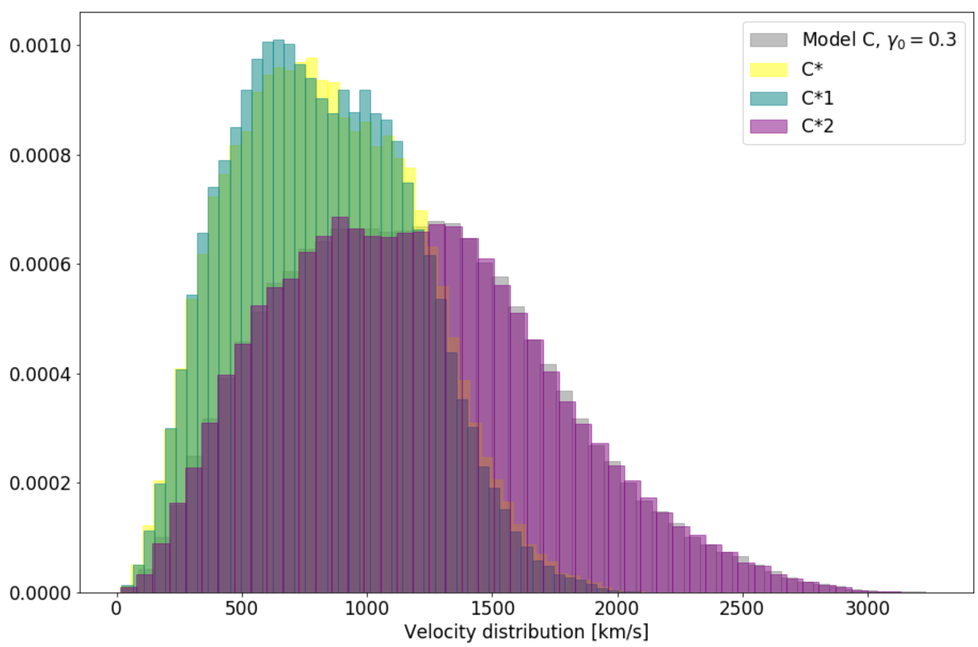

Figure 3.19: Velocity distribution for the most massive halo selected from the models C with $\gamma_0 = 0.3$, C*, C*1 and C*2.

Thus we can see that with only the modified cosmological friction term included, the velocity dispersion and mean value is not significantly different from that of model C without any coupling. With the inclusion of the modified gravitational force term only we see a clear shift in the velocity distribution, matching that of the full model C. This further demonstrates that all the consequences from the coupling seen in our results are due to the modified gravitational force term. As far as the mass of the selected halos is concerned, we can see that the masses of the halos from the models C*1 and C*2 are ~75% and ~ 99% of the model C mass for γ_0= 0.3, respectively. Note that this mass difference is again a consequence of the enhanced structure formation resulting from the modified effective gravitational force. It is important to note, however, that the lower mass of the C*1 halo will result in a narrower velocity distribution with a lower mean, but the mass difference alone is not sufficient to explain the differences in the velocity distributions shown here.

3.7 Halo velocity distribution

We have so far analysed the velocity dispersion and distribution of the dark matter within the halos. Now we examine the velocity distribution of the halos themselves. To do so, we have selected the host halos of each model, for each value of γ_0, considering those with and without substructures and all the subhalos of the sample, both over the whole mass range. We analyse their velocity distributions, which are shown in Figures 3.20 and 3.21. As we can see in the figures, models A, B and C (from left to right) do not show any significant variation in the velocity distributions of the host halos between the models. This also does not seem to be affected by the variation in the change of the coupling constant. This behaviour of the host halo velocity distributions with respect to the coupling does not seem to be affected by the increase of the gravitational force in our models. For the subhalos, on the other hand, we see that the behaviour seen in the host halos is repeated for models A and B, showing no significant differences between each value of γ_0. For model C on the other hand, we see a slight deviation in the velocity distribution for $\gamma_0 = 0.3$, showing a shift towards higher velocities. This result (which is not seen for the host halos), suggests that the presence of the coupling does not lead to a global change in the velocities of the host halos, but rather its presence seems to be more influential on smaller scales.

To better understand the velocity distribution of the host halos and subhalos, we have performed a cumulative histogram of the host halos of model C (without considering the substructures) and an analysis of the subhalos considering the most massive host halo of model C, which are shown in Figures 3.22 and 3.23.

For the analysis of the host halos, we have normalised by the highest velocity (V_{max}) of the hosts at $z = 0$. We can see that there is a larger population of low-velocity halos (compared to V_{max}) for ΛCDM as compared to model C, with or

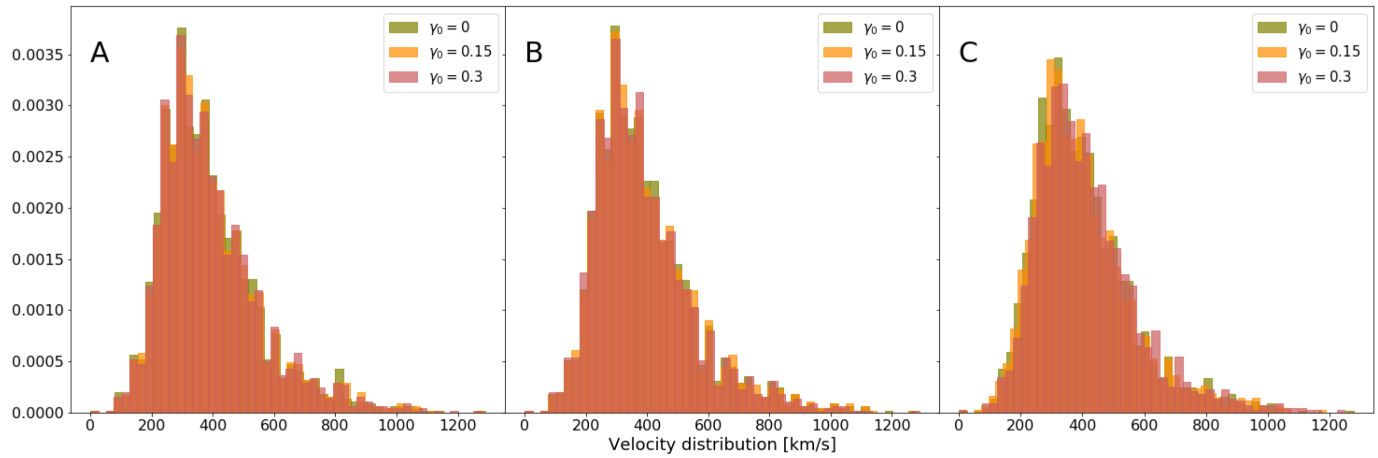

Figure 3.20: Velocity distribution of the host halos.

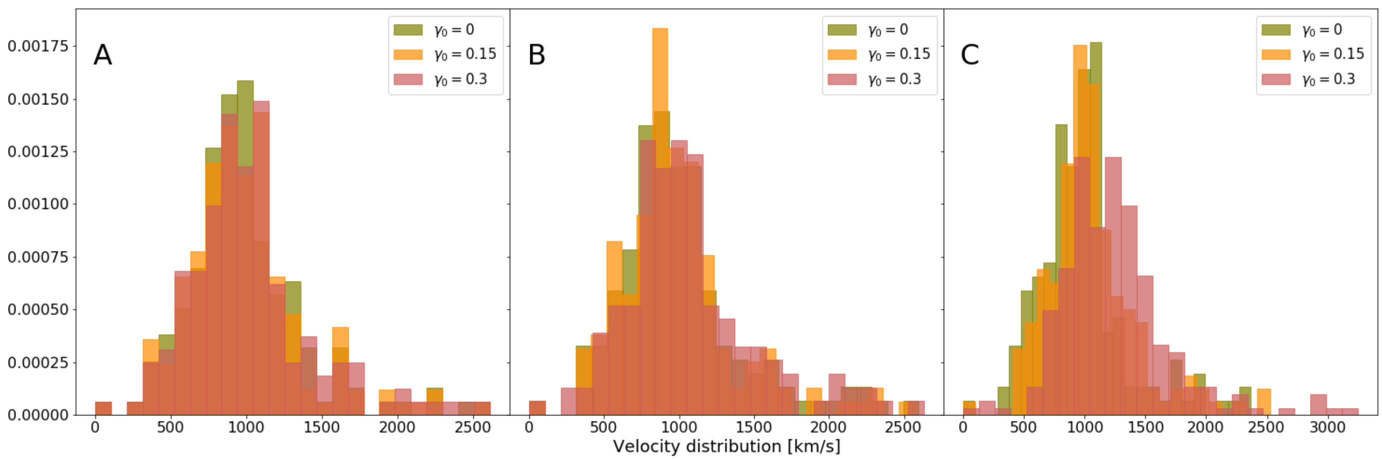

Figure 3.21: Velocity distribution of the subhalos within the most massive host.

without coupling, due to the differing background evolution. For different values of the coupling, however, there is no significant difference in the cumulative distributions, consistent with the result shown in Figure 3.20. For the subhalos of the most massive host the velocity population for the uncoupled model is comparable to that of ΛCDM, despite the differing background evolution. This is expected given that

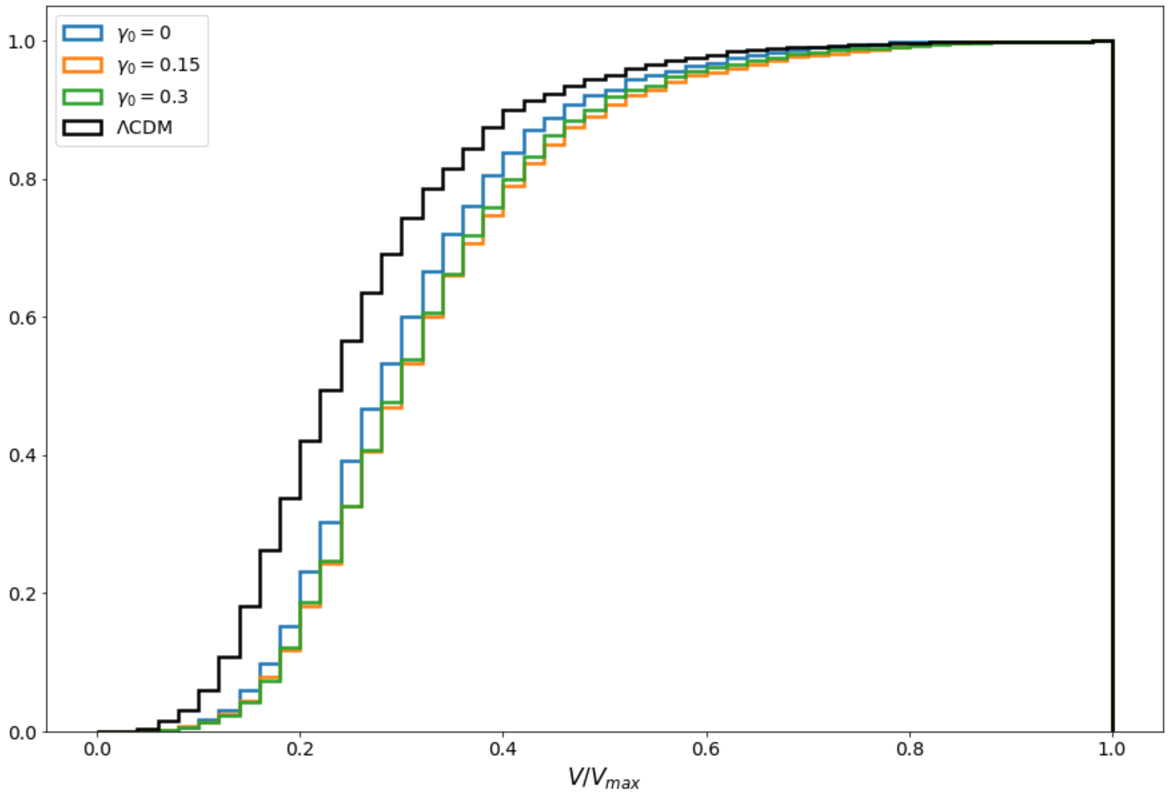

Figure 3.22: Cumulative velocity for all host halos for the model C at $z \sim 0$.

the background evolution is less relevant for the halos within a virialised structure. Increasing the coupling, however, leads to larger fractions of medium- to high-velocity halos, due to the influence of the modified effective gravitational force. Again, this is consistent with the result shown in Figure 3.21.

3.8 Halo velocity field

We have considered the full sample of halos with their respective substructures for each model and determined their velocity vector field, to analyse the motion of the matter flow within each model. Figures 3.24, 3.25 and 3.26 show the flow behaviour

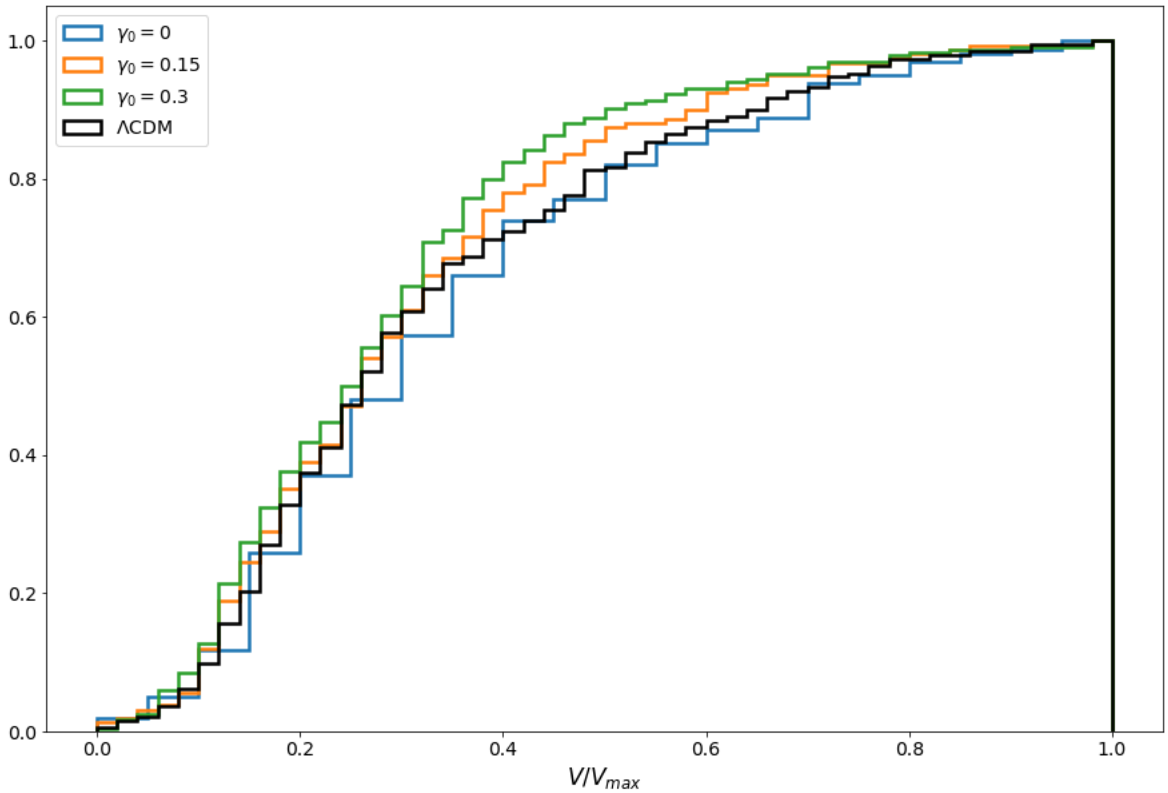

Figure 3.23: Cumulative velocity for the most massive host halo for the model C at $z \sim 0$.

for $\gamma_0 = 0$, 0.15 and 0.3 of model C respectively, together with the velocity flow in a small region around the most massive halo identified in the simulations (given in the right panel of each figure). As we can see, there is a convergence towards the zones with structures and a divergence away from the voids, as expected from the gravitational clustering experienced by the dark matter. We can also see that regions of higher concentration show higher velocities, which we attribute to the presence of halos with higher masses, as well as, to the increase of the gravitational force present in our models, which becomes more noticeable when $\gamma_0 = 0.3$ (Fig. 3.26). In the case of the more massive halo for each value of γ_0, we can notice how the presence of

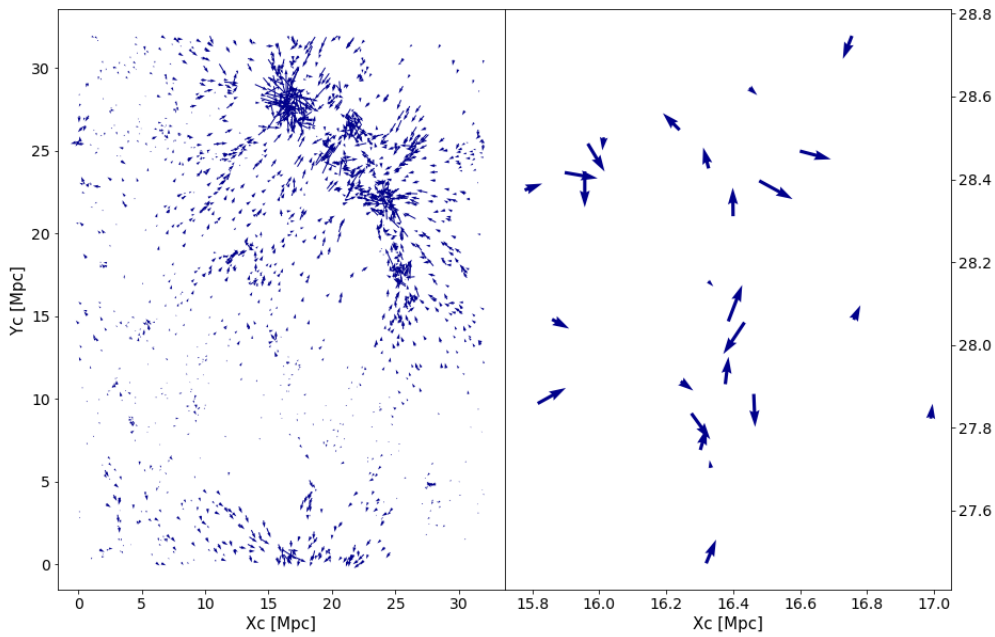

Figure 3.24: Vector field for $\gamma_0 = 0$ of model C.

stronger coupling leads to higher velocities, as well as more concentrated structures, compared to the uncoupled case. It is also worth noting that the *direction* of the matter flow at larger scales is not affected by the coupling.

3.9 Phase space diagrams

The modified effective gravitational force in our models will have consequences for the strength of dynamical friction experienced by massive halos as they orbit within their hosts. Specifically, given that the effective gravitational force is larger in the presence of the coupling, we would expect increased velocities for the dark matter particles (as we will shown in Section 3.6) leading to an enhanced dynamical friction in the coupled case. Our expectation is that this could lead to a change in the cluster build-up history, at least for very massive halos. One way to examine this history is with the use of so-called phase space diagrams, where we consider the host-centric radius (normalised by the host virial radius) and the host-centric velocity (normalised by

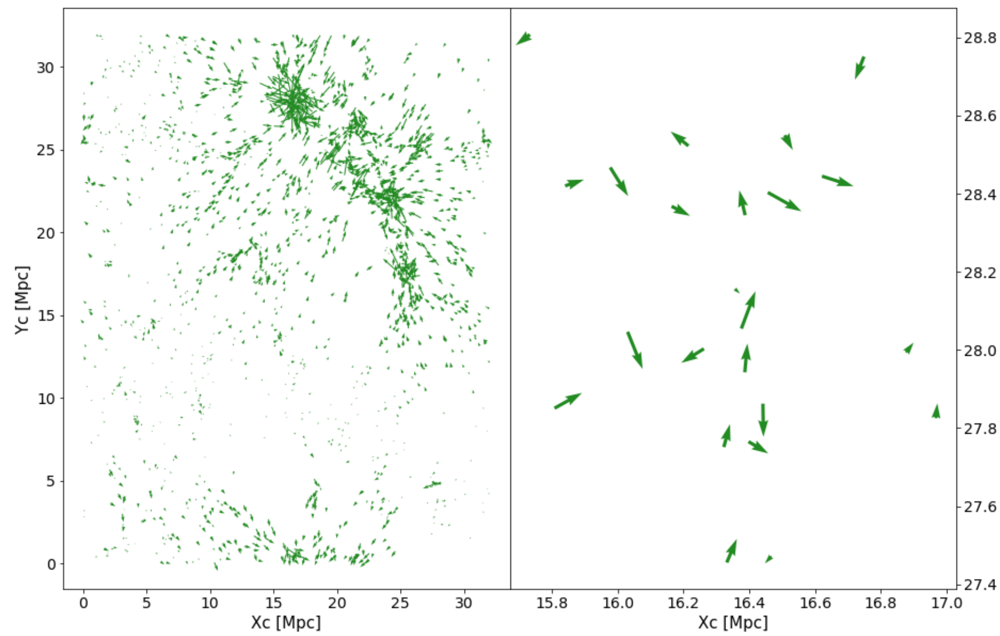

Figure 3.25: Vector field for $\gamma_0 = 0.15$ of model C.

the host velocity dispersion) for all the substructures within a host. These diagrams have proven very useful in various studies of galaxy evolution ([58]). To study this, we have made phase space diagrams, and then used the kernel density estimation (KDE) method, which allows us to represent the continuous variable data as probability density curves. Thus, the algorithm (3.3) takes the number of data n and represents them by means of a Kernel, whose function defines the shape and distribution of the data that allow us to visualize the phase space of the substructures for models A, B and C. For our data, we have used a Gaussian kernel, $K(x; h) \propto \exp(-\frac{x^2}{2h^2})$, with a standard deviation equivalent to the smoothing parameter h.

$$f(x) = \frac{1}{n}\sum_{i=1}^{n} K_h(x - x_i) = \frac{1}{nh}\sum_{i=1}^{n} K(\frac{x - x_i}{h}) \tag{3.3}$$

All of our plots are at $z = 0$. For this purpose, we have considered the 12 most massive substructures with their respective hosts taking the values of $\gamma_0 = 0.15$ and $\gamma_0 = 0.3$, which have been compared with the uncoupled case. The combination of

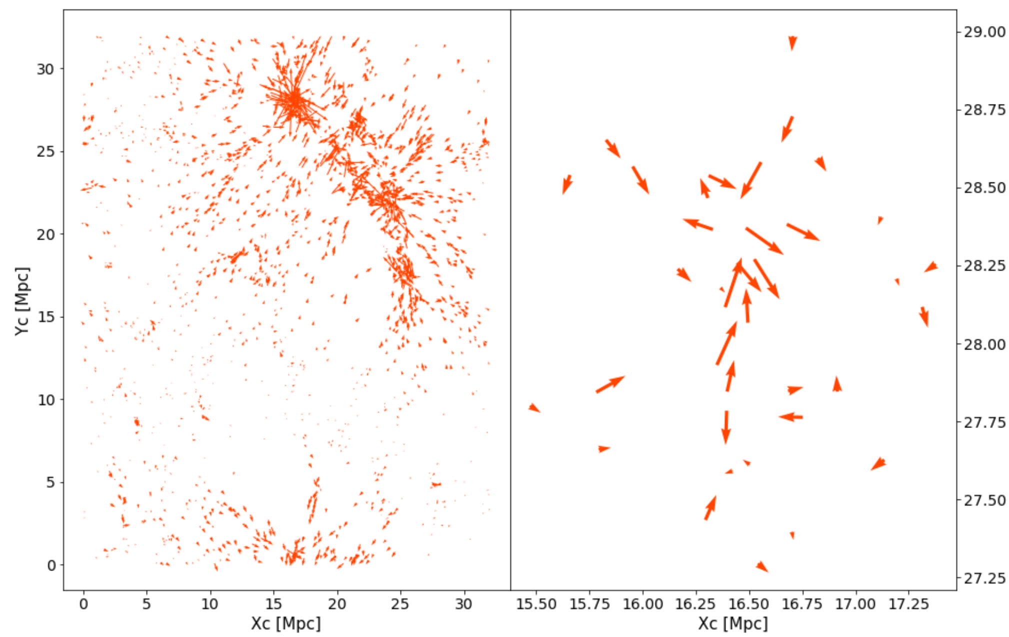

Figure 3.26: Vector field for $\gamma_0 = 0.3$ of model C.

various hosts in the same phase space diagram is possible thanks to the normalisation with respect to the virial radius and the velocity dispersion. This also helps us to extract any systematic difference between our models. Figures 3.27, 3.28, 3.29 show the evolution of these substructures at different redshifts, having a total of 9 snapshots for each model, comparing $\gamma_0 = 0$ with $\gamma_0 = 0.15$, and the same for Figures 3.30, 3.31, 3.32 where we compare $\gamma_0 = 0$ with $\gamma_0 = 0.3$.

It is interesting to note that, for all models, we can see a similar averaged evolution of our host halos. There is some evidence of an early accretion of massive subhalos into the host, around $z \approx 2$, shown by the diagonal distribution of the contours, and their tendency towards higher velocities. This would correspond to infalling material being accelerated by the host potential well. The "flattening" of the distribution at $z \approx 1$ is an artefact of rescaling the velocity axis to accommodate the higher velocities in the following plots. The presence of protrusions or "blobs" beyond the main central density for all remaining redshifts suggests the presence of additional infall of material into an already well-established host. We must remember, however,

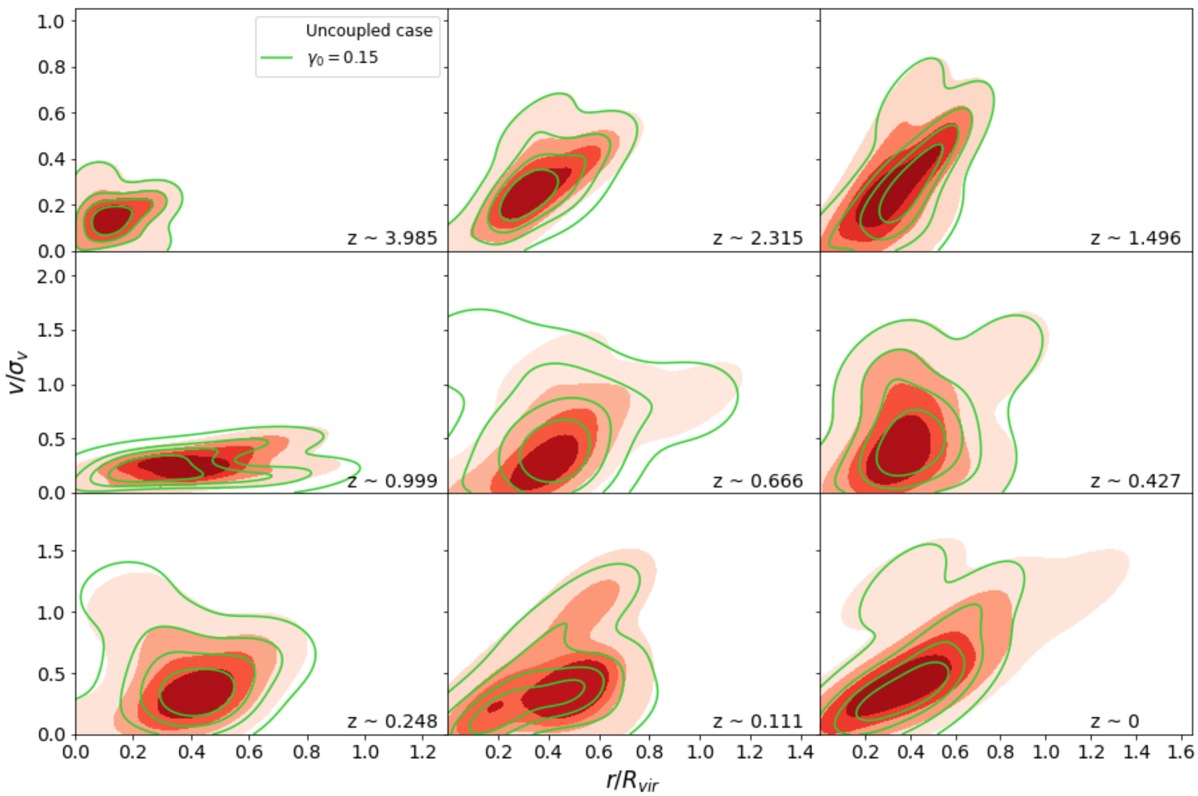

Figure 3.27: Comparison between $\gamma_0 = 0$ and 0.15 in phase space diagram for model A.

that here we consider only massive subhalos. For the cases comparing $\gamma_0 = 0.15$ with the uncoupled case we can see how the density contours of the substructures do not show significant variations at $z \sim 0$, with any differences generally being confined to the outer contours, where the number of halos is low and thus the statistical noise is likely to be higher. In particular, for models A and B we see very little systematic difference in the inner contours either, suggesting a very similar history of host build-up in these models when compared to the uncoupled cases. For model C, we note that there is a more significant deviation from the uncoupled case at all redshifts, but especially for $z \approx 0.2$ and $z \approx 0.1$, where the differences extend

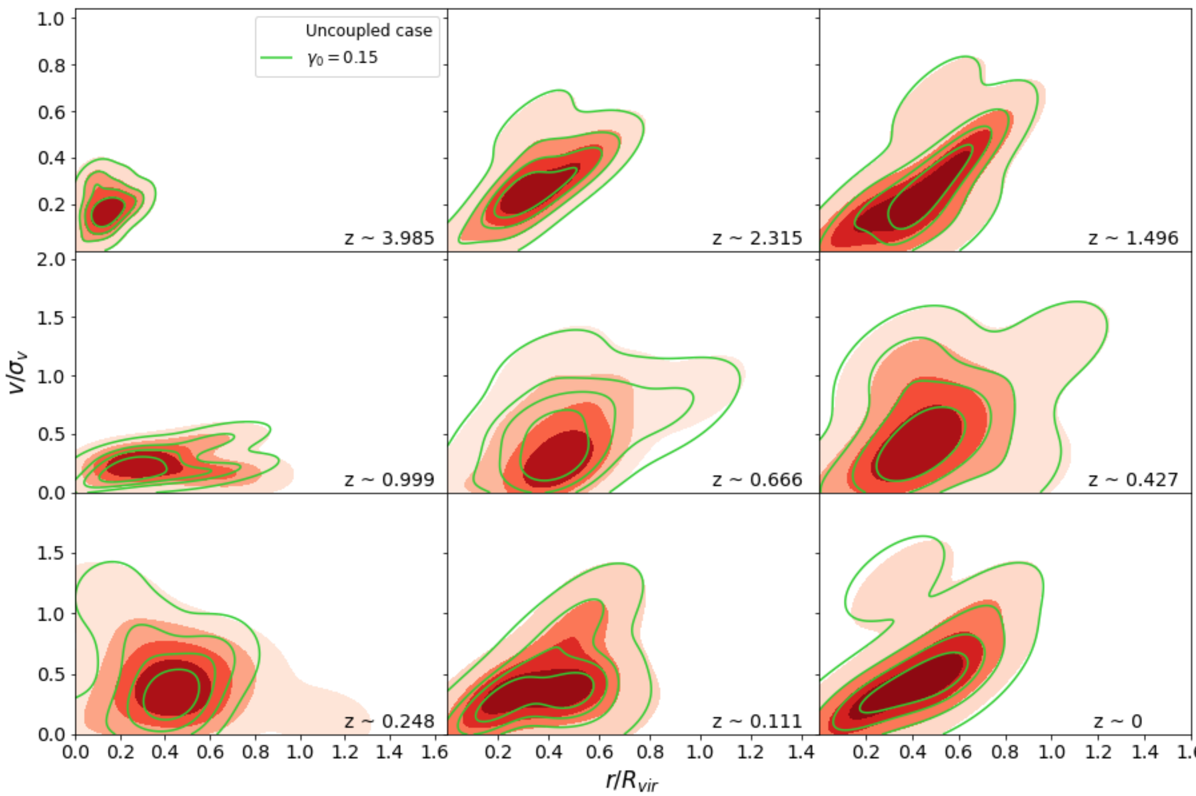

Figure 3.28: Comparison between $\gamma_0 = 0$ and 0.15 in phase space diagram for model B.

to the inner contours. We have seen in our previous results that the difference in the background evolution between the coupled and uncoupled cases is minimal and the contribution of the modified cosmological friction term is negligible, thus we attribute the differences in the phase spaces to the modified gravitational force term. We see that the contours for the coupled model are offset from those of the uncoupled case for $z \approx 0.4$, $z \approx 0.2$ and $z \approx 0.1$. Furthermore, in the uncoupled model the density peak shows larger movements between these two redshifts than for the coupled case. This suggests a possible time-delay between the two models in the process of virialisation after the accretion of new material and a damping of the

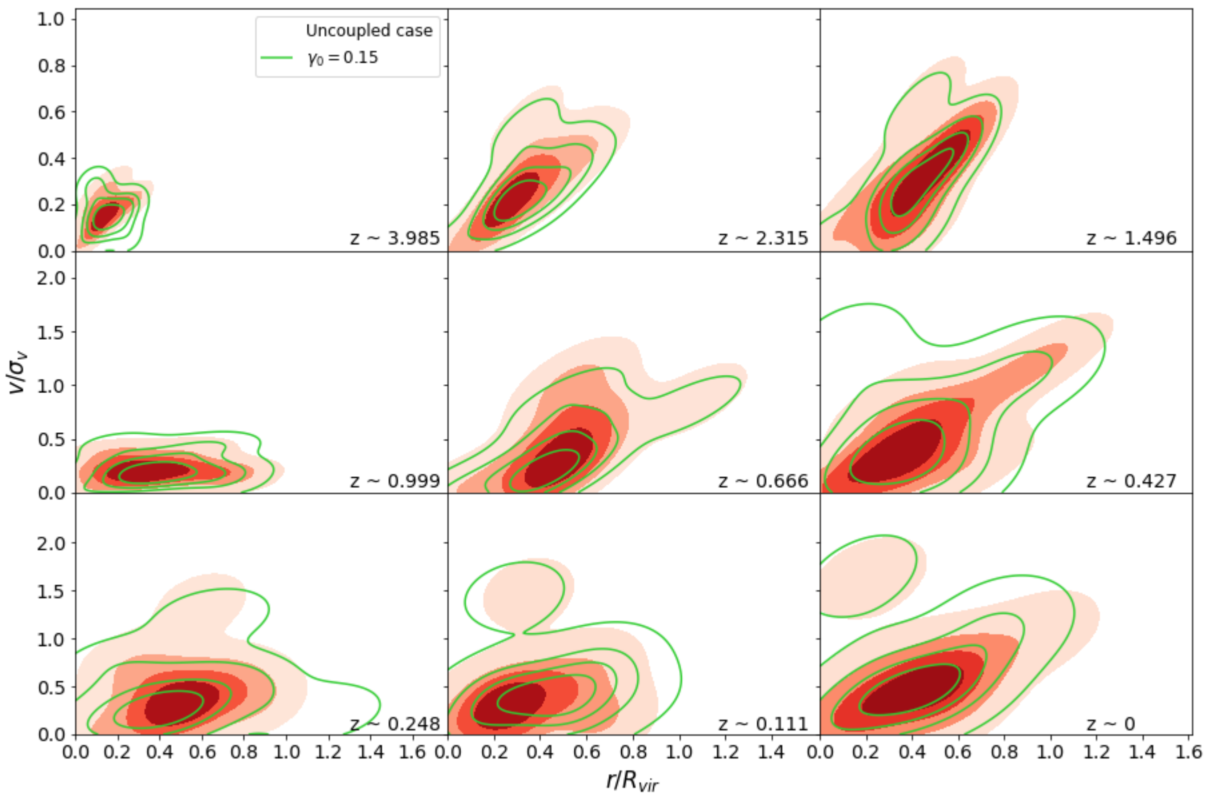

Figure 3.29: Comparison between $\gamma_0 = 0$ and 0.15 in phase space diagram for model C.

amplitude of density "oscillations" resulting from this accretion. These correspond to indirect weak evidence for a difference in the effect of dynamical friction between the two models.

For models with $\gamma_0 = 0.3$, we can see that again there are no clear variations due to the coupling in models A and B. However, for model C we can see that the contours are shifted with respect to the uncoupled case, for $z \approx 0.2$ and $z \approx 0.1$, in a manner similar to that seen for $\gamma_0 = 0.15$. Furthermore, with a stronger coupling, the final density peak is closer to the (combined) host centre, further suggesting an enhancement of dynamical friction.

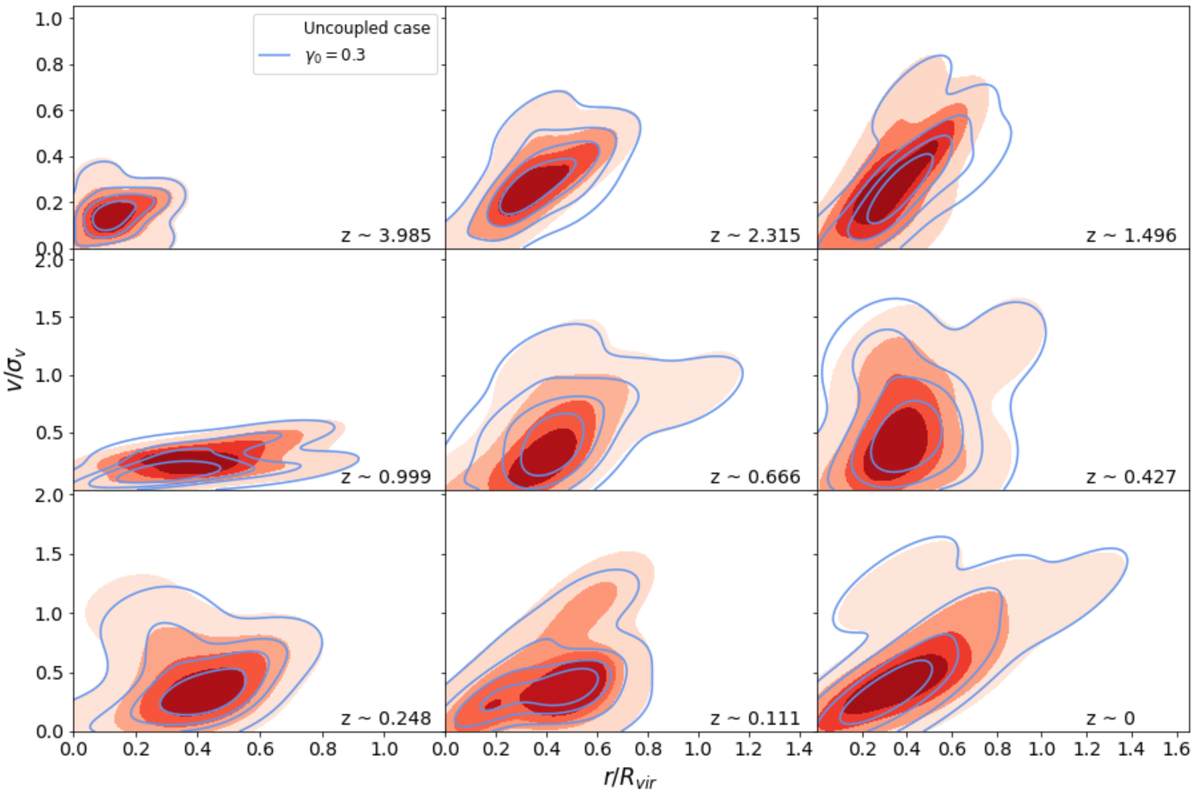

Figure 3.30: Comparison between $\gamma_0 = 0$ and 0.3 in phase space diagram for model A.

We must reiterate that the sample size is very small, which has been limited mainly by the low resolution of our simulations. A set of new high-resolution simulations could help us to better determine, statistically, the effects of the coupling on the evolution of dark matter halos and their substructures.

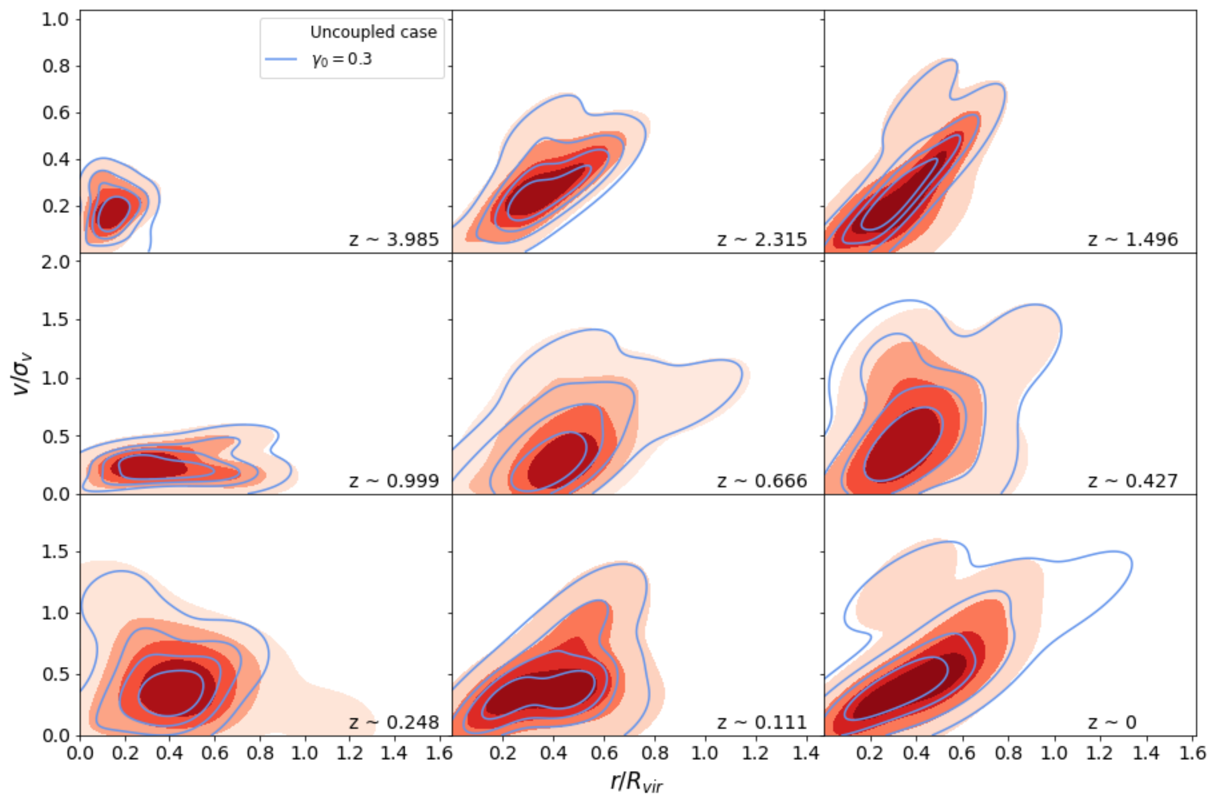

Figure 3.31: Comparison between $\gamma_0 = 0$ and 0.3 in phase space diagram for model B.

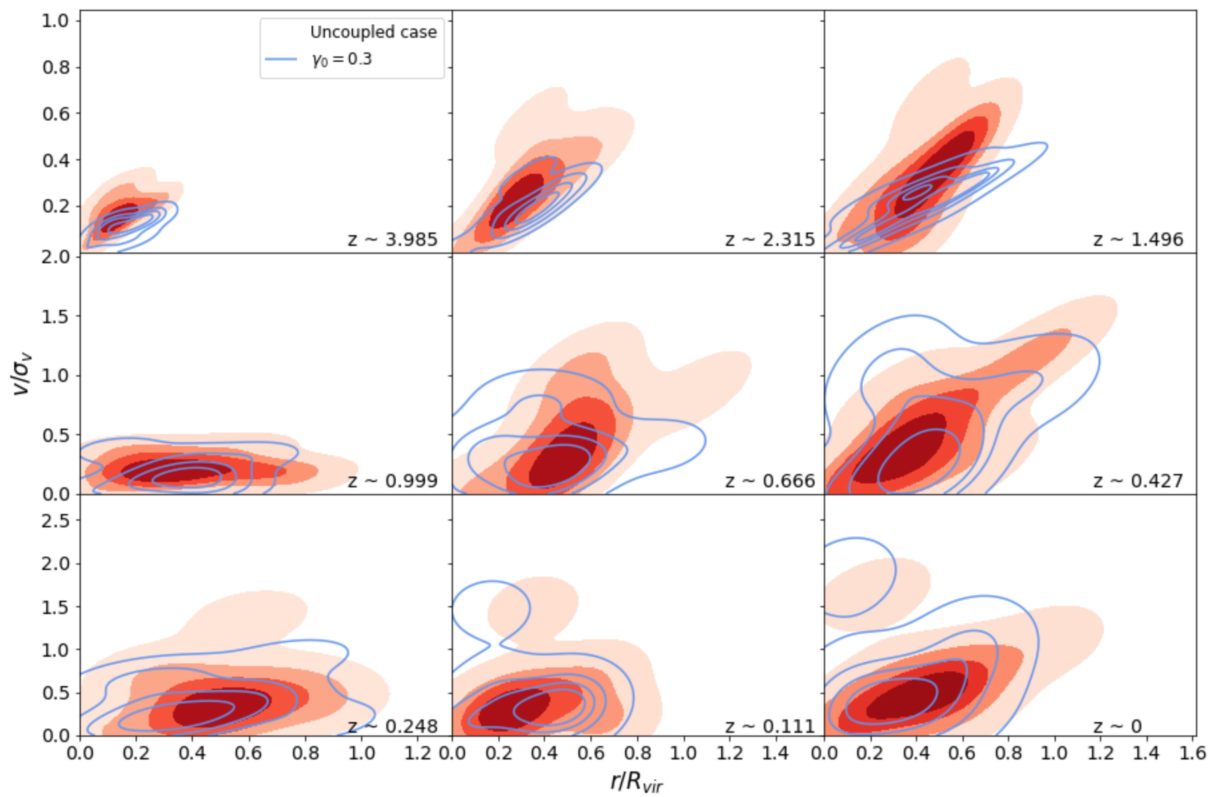

Figure 3.32: Comparison between $\gamma_0 = 0$ and 0.3 in phase space diagram for model C.

Chapter 4

Discussion and conclusions

In this thesis we have analysed structure formation in a coupled DM/DE model, where dark energy arises from a quintessence field, and the coupling is purely at the level of a momentum transfer. Our analysis has been based on numerical N-body simulations using a modified version of the RAMSES cosmological simulations code. We have determined the form of the modified Euler equation in the Newtonian gauge, and then considered the small-scale Newtonian limit. We have shown that the coefficients of the cosmological friction and gravitational force terms in the resulting Euler equation are time-dependent, being functions of the coupling parameter γ_0, the time derivative of the background quintessence field $\dot{\bar{\phi}}$, the derivative of the potential V_ϕ and the background dark matter density ρ. We have considered exclusively the case where $\gamma_0 > 0$, resulting in a suppression of the cosmological friction term (relative to the standard case) and an enhancement of the effective gravitational force.

After implementation of the modified Euler equation into the numerical code, we have then investigated the consequences for structure formation at recent times, as well as the consequences at the level of individual dark matter halos, for three choices of scalar field potential. For two of these potentials the background evolution is very similar to that of ΛCDM, with only a small deviation from -1 at very late times in the value of the dark energy equation of state parameter w. In one of our models, referred to as model C, we have a more pronounced deviation in the background evolution, corresponding to a larger deviation from $w = -1$. This corresponds to a large contribution from the scalar field kinetic term, leading to non-negligible deviations from unity in the Euler equation coefficients.

Our results demonstrate that, for these models, the modification of the cosmological friction term is effectively irrelevant for the dynamics of structure formation in all of our models. The modification of the effective gravitational force, however, leads to significant differences, at least for model C, when compared to the uncoupled case. Our specific results are:

- The power spectrum is substantially enhanced in model C (with large coupling), especially at smaller scales. For our other models, with a background evolution closer to that of ΛCDM, we see much less enhancement.

- The host halo velocity distribution, and therefore the bulk flow, is not significantly changed in any model, but the subhalo velocities are shown to be larger in model C with large coupling. Thus material within a large overdensity is moving faster, due to the modified effective gravitational force.

- For the same reason, the particle velocities within the massive halos are also substantially higher with the coupling (in model C) than without. Again, the modified gravitational force is responsible.

- The enhanced gravitational force also apparently leads to steeper (cuspier) inner density profiles in at least our most massive halos. Our limited spatial resolution, however, does not allow us to meaningfully examine the innermost regions of the halos.

- Using phase-space diagrams we have inferred a possible modification in the nature of cluster build-up in our model C, beyond that to be expected from the presence of a stronger effective gravity. This is presumably due to a modification in the effect of the dynamical friction within these halos due to the increased particle velocities.

It is worth noting that our study differs considerably from previous work done on simulations of a momentum transfer coupling between dark matter and dark energy ([13],[14]). In those works an elastic scattering model was studied, with dark energy being given by a homogeneous fluid. This model differs in two important ways from the models discussed in this thesis: our models include a quintessence scalar field for the dark energy, not a fluid; and the modified gravitational force term in our models is non-existent in the elastic scattering model. It is the modification of this term in the Euler equation that leads to the most significant effects in our results. Physically, we may interpret this effect as coming from a clustering of the dark energy component, which is not present in the elastic scattering models.

In summary, our results, although based on the specific choices made for the quintessence potential, point to the conclusion that, as far as non-linear structure formation is concerned, these coupled models do not, generically, differ substantially from their uncoupled cousins. It is only in the case where the DE equation of state parameter deviates from $w = -1$ that we may have a sufficient contribution from the kinetic energy of the quintessence field to generate a substantial additional force upon the dark matter, modifying the evolution of structure. The modification that results is that of more structure, with denser, cuspier halos. This implies that our models would exacerbate the small-scale problems with ΛCDM, not alleviate them.

We should reiterate that we have obtained significant effects in model C because of the similar magnitudes of the two terms in the denominators in equations 2.45. As discussed in Section 2.4.2, in cases where $\rho_0 \approx 2a\gamma_0\dot{\bar{\phi}}^2$ we expect substantial deviations, as compared to the standard case, in the coefficients of the Euler equation. If we in fact have an equality in this relationship, we will find singular behaviour in these coefficients. This strongly suggest a limitation in the physical viability of these models.

An interesting aspect of this work that would benefit from more investigation is the combination of a modified dynamics for dark matter with standard dynamics for the baryons. In particular, we have already tentatively explored the possible consequences for dynamical friction, given that the strength of this effect on an object falling into a dark matter halo depends on the velocities of the dark matter particle field. It is, in fact, possible that dynamical friction is enhanced for the dark matter, due to the enhanced gravitational force, but *reduced* for the baryons, due to the increased velocity of the dark matter particles combined with the baryons experiencing standard Newtonian gravity. It would certainly be of interest to explore the consequences of this for galaxy dynamics, such as in galaxy mergers and the evolution of bars.

A promising avenue for future research in this topic would be to repeat our analysis for $\gamma_0 < 0$. This has already been shown, at the linear level, to reduce some tensions in the standard model, specifically with σ_8 ([57]). It is straightforward to consider the evolution of the coefficients c_1 and c_2 for the case of model C with $\gamma_0 = -0.3$ (see Figure 4.1). We see that the cosmological friction is now enhanced but the effective gravitational force is reduced. The amplitudes of these variations, however, are considerably smaller than seen for the $\gamma_0 = 0.3$ model. This is because, due to the negative γ_0 in the denominators of equation 2.45, the singular behaviour discussed earlier cannot arise. For $\gamma_0 > 0$, a strong coupling problem restricts the range to $\gamma_0 < 1/2$. There is no known restriction for negative values of γ_0, thus a larger absolute value of γ_0 could potentially be considered in that case. Given that the effective gravitational force is weaker for $\gamma_0 < 0$, this is also likely to reduce the amount of structure formed as well as the slopes of the inner densities of that structure. Future studies of these models would also benefit enormously from increased spatial and mass resolution, as well as larger box sizes to explore consequences at very large scales and compare with analytic (linear) perturbation theory results.

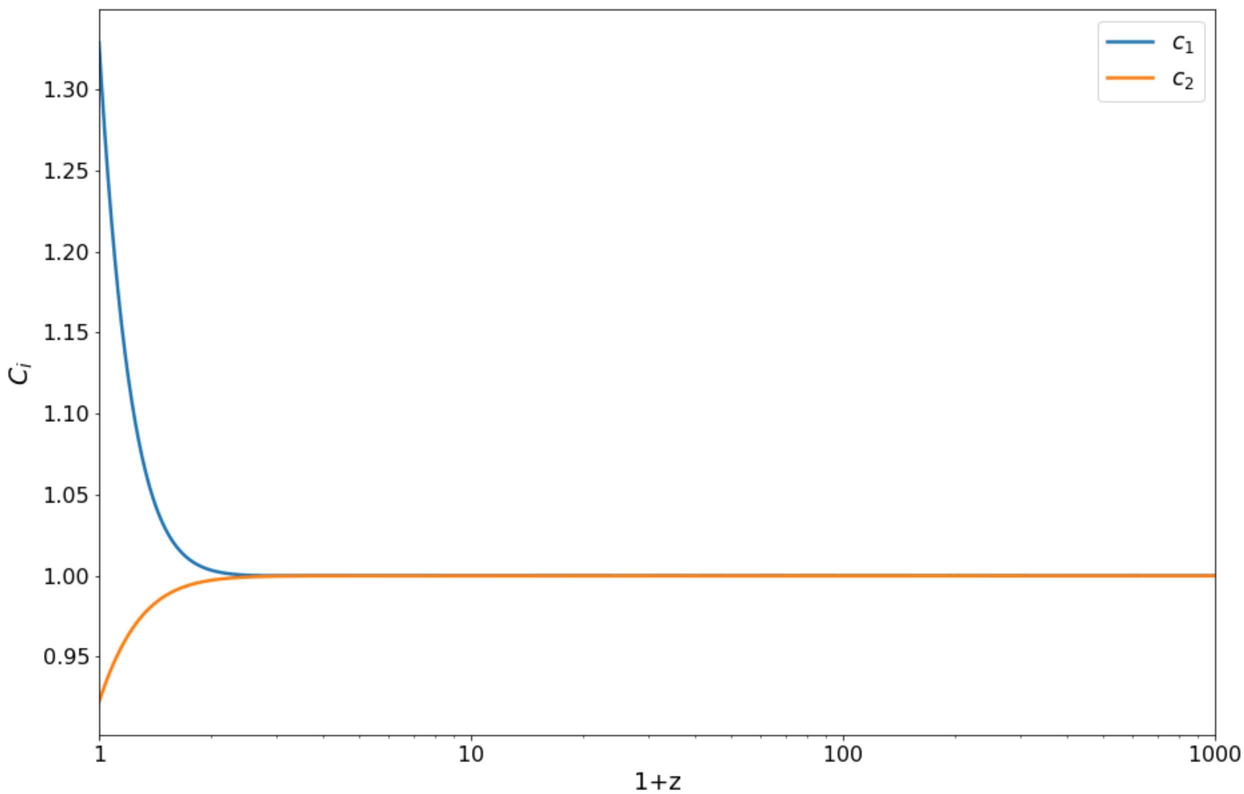

Figure 4.1: Variation of the coefficient of the cosmological friction term (c_1) and the coefficient of the gravitational force term (c_2) for model C with $\gamma_0 = -0.3$.

Bibliography

[1] P. A. R. Ade, N. Aghanim, C. Armitage-Caplan, M. Arnaud, M. Ashdown, F. Atrio-Barandela, J. Aumont, C. Baccigalupi, A. J. Banday, and et al. Planck2013 results. xvi. cosmological parameters. *Astronomy Astrophysics*, 571:A16, Oct 2014.

[2] P. A. R. Ade, N. Aghanim, C. Armitage-Caplan, M. Arnaud, M. Ashdown, F. Atrio-Barandela, J. Aumont, C. Baccigalupi, A. J. Banday, and et al. Planck2013 results. xx. cosmology from sunyaev–zeldovich cluster counts. *Astronomy Astrophysics*, 571:A20, Oct 2014.

[3] P. A. R. Ade, N. Aghanim, M. Arnaud, M. Ashdown, J. Aumont, C. Baccigalupi, A. J. Banday, R. B. Barreiro, J. G. Bartlett, and et al. Planck2015 results. *Astronomy Astrophysics*, 594:A13, Sep 2016.

[4] N. Aghanim, Y. Akrami, M. Ashdown, J. Aumont, C. Baccigalupi, M. Ballardini, A. J. Banday, R. B. Barreiro, N. Bartolo, and et al. Planck 2018 results. *Astronomy Astrophysics*, 641:A6, Sep 2020.

[5] A. Albrecht and C. Skordis. Phenomenology of a realistic accelerating universe using only planck-scale physics. *Physical Review Letters*, 84(10):2076–2079, Mar 2000.

[6] L. Amendola. Coupled quintessence. *Physical Review D*, 62(4), Jul 2000.

[7] L. Amendola and C. Quercellini. Tracking and coupled dark energy as seen by the wilkinson microwave anisotropy probe. *Physical Review D*, 68(2), Jul 2003.

[8] L. Amendola and S. Tsujikawa. Dark energy: Theory and observations. *Dark Energy : Theory and Observations by Luca Amendola and Shinji Tsujikawa. Cambridge University Press, 2010. ISBN: 9780521516006*, 01 2010.

[9] R. An, A. A. Costa, L. Xiao, J. Zhang, and B. Wang. Testing a quintessence model with yukawa interaction from cosmological observations and n-body simulations. *Monthly Notices of the Royal Astronomical Society*, 489(1):297–309, Jul 2019.

[10] C. Armendariz-Picon, V. Mukhanov, and P. J. Steinhardt. Essentials ofk-essence. *Physical Review D*, 63(10), Apr 2001.

[11] M. Baldi. Simulations of structure formation in interacting dark energy cosmologies. *Nuclear Physics B - Proceedings Supplements*, 194:178–184, Oct 2009.

[12] M. Baldi. The codecs project: a publicly available suite of cosmological n-body simulations for interacting dark energy models. *Monthly Notices of the Royal Astronomical Society*, 422(2):1028–1044, Mar 2012.

[13] M. Baldi and F. Simpson. Simulating momentum exchange in the dark sector. *MNRAS*, 449(3):2239–2249, May 2015.

[14] M. Baldi and F. Simpson. Structure formation simulations with momentum exchange: alleviating tensions between high-redshift and low-redshift cosmological probes. *MNRAS*, 465(1):653–666, Feb. 2017.

[15] N. Bartolo and M. Pietroni. Scalar-tensor gravity and quintessence. *Physical Review D*, 61(2), Dec 1999.

[16] M. R. Blanton, M. A. Bershady, B. Abolfathi, F. D. Albareti, C. Allende Prieto, A. Almeida, J. Alonso-García, F. Anders, S. F. Anderson, B. Andrews, and et al. Sloan Digital Sky Survey IV: Mapping the Milky Way, Nearby Galaxies, and the Distant Universe. *AJ*, 154:28, July 2017.

[17] B. Bose, M. Baldi, and A. Pourtsidou. Modelling non-linear effects of dark energy. *Journal of Cosmology and Astroparticle Physics*, 2018(04):032–032, Apr 2018.

[18] A. M. Brooks, M. Kuhlen, A. Zolotov, and D. Hooper. A baryonic solution to the missing satellites problem. *The Astrophysical Journal*, 765(1):22, Feb 2013.

[19] J. S. Bullock and M. Boylan-Kolchin. Small-scale challenges to the cdm paradigm. *Annual Review of Astronomy and Astrophysics*, 55(1):343–387, Aug 2017.

[20] J. S. Bullock, A. V. Kravtsov, and D. H. Weinberg. Reionization and the abundance of galactic satellites. *The Astrophysical Journal*, 539(2):517–521, Aug 2000.

[21] A. Burkert. The Structure of Dark Matter Halos in Dwarf Galaxies. *APJ*, 447:L25–L28, July 1995.

[22] R. R. Caldwell, R. Dave, and P. J. Steinhardt. Cosmological imprint of an energy component with general equation of state. *Physical Review Letters*, 80(8):1582–1585, Feb 1998.

[23] G. N. Candlish. The velocity field in MOND cosmology. *MNRAS*, 460(3):2571–2585, Aug. 2016.

[24] S. CAPOZZIELLO. Curvature quintessence. *International Journal of Modern Physics D*, 11(04):483–491, Apr 2002.

[25] S. Colombi, A. Jaffe, D. Novikov, and C. Pichon. Accurate estimators of power spectra in N-body simulations. *MNRAS*, 393(2):511–526, Feb. 2009.

[26] B. Diemer. Colossus: A python toolkit for cosmology, large-scale structure, and dark matter halos. *The Astrophysical Journal Supplement Series*, 239(2):35, Dec 2018.

[27] A. Einstein. Die Feldgleichungen der Gravitation. *Sitzungsberichte der Königlich Preußischen Akademie der Wissenschaften (Berlin*, pages 844–847, Jan 1915.

[28] A. Einstein. Kosmologische Betrachtungen zur allgemeinen Relativitätstheorie. *Sitzungsberichte der Königlich Preußischen Akademie der Wissenschaften (Berlin*, pages 142–152, Jan 1917.

[29] D. J. Eisenstein and D. H. e. Weinberg. SDSS-III: Massive Spectroscopic Surveys of the Distant Universe, the Milky Way, and Extra-Solar Planetary Systems. *AJ*, 142(3):72, Sep 2011.

[30] A. Fitts, M. Boylan-Kolchin, O. D. Elbert, J. S. Bullock, P. F. Hopkins, J. Oñorbe, A. Wetzel, C. Wheeler, C.-A. Faucher-Giguère, D. Kereš, and et al. fire in the field: simulating the threshold of galaxy formation. *Monthly Notices of the Royal Astronomical Society*, 471(3):3547–3562, Jul 2017.

[31] R. A. Flores and J. R. Primack. Observational and Theoretical Constraints on Singular Dark Matter Halos. *APJ*, 427:L1, May 1994.

[32] C. Frenk and S. White. Dark matter and cosmic structure. *Annalen der Physik*, 524(9-10):507–534, Sep 2012.

[33] S. Genel, M. Vogelsberger, V. Springel, D. Sijacki, D. Nelson, G. Snyder, V. Rodriguez-Gomez, P. Torrey, and L. Hernquist. Introducing the illustris project: the evolution of galaxy populations across cosmic time. *Monthly Notices of the Royal Astronomical Society*, 445(1):175–200, Sep 2014.

[34] S. P. D. Gill, A. Knebe, and B. K. Gibson. The evolution of substructure - I. A new identification method. *MNRAS*, 351(2):399–409, June 2004.

[35] O. Hahn and T. Abel. Multi-scale initial conditions for cosmological simulations. *Monthly Notices of the Royal Astronomical Society*, 415(3):2101–2121, Jul 2011.

[36] E. Hubble. A Relation between Distance and Radial Velocity among Extra-Galactic Nebulae. *Proceedings of the National Academy of Science*, 15(3):168–173, Mar 1929.

[37] A. Kamenshchik, U. Moschella, and V. Pasquier. An alternative to quintessence. *Physics Letters B*, 511(2-4):265–268, Jul 2001.

[38] S. R. Knollmann and A. Knebe. Ahf: Amiga's halo finder. *The Astrophysical Journal Supplement Series*, 182(2):608–624, May 2009.

[39] A. Koch and E. K. Grebel. The anisotropic distribution of m31 satellite galaxies: A polar great plane of early-type companions. *The Astronomical Journal*, 131(3):1405–1415, Mar 2006.

[40] J. Lesgourgues. The cosmic linear anisotropy solving system (class) i: Overview, 2011.

[41] A. Lewis and A. Challinor. CAMB: Code for Anisotropies in the Microwave Background, Feb. 2011.

[42] B. Li and J. D. Barrow. N-body simulations for coupled scalar-field cosmology. *Physical Review D*, 83(2), Jan 2011.

[43] B. Li and J. D. Barrow. On the effects of coupled scalar fields on structure formation. *Monthly Notices of the Royal Astronomical Society*, 413(1):262–270, Feb 2011.

[44] A. Macciò, C. Quercellini, R. Mainini, L. Amendola, and S. Bonometto. Coupled dark energy: Parameter constraints fromn-body simulations. *Physical Review D*, 69(12), Jun 2004.

[45] H. Martel and P. R. Shapiro. A convenient set of comoving cosmological variables and their application. *Monthly Notices of the Royal Astronomical Society*, 297(2):467–485, Jun 1998.

[46] B. e. a. Moore. Dark Matter Substructure within Galactic Halos. *APJ*, 524(1):L19–L22, Oct. 1999.

[47] O. Müller, M. S. Pawlowski, H. Jerjen, and F. Lelli. A whirling plane of satellite galaxies around centaurus a challenges cold dark matter cosmology. *Science*, 359(6375):534–537, Feb 2018.

[48] J. F. Navarro, C. S. Frenk, and S. D. M. White. The Structure of Cold Dark Matter Halos. *ApJ*, 462:563, May 1996.

[49] S.-H. Oh et al. High-resolution mass models of dwarf galaxies from LITTLE THINGS. *Astron. J.*, 149:180, 2015.

[50] G. Pantazis, S. Nesseris, and L. Perivolaropoulos. Comparison of thawing and freezing dark energy parametrizations. *Physical Review D*, 93(10), May 2016.

[51] M. S. Pawlowski, P. Kroupa, and H. Jerjen. Dwarf galaxy planes: the discovery of symmetric structures in the local group. *Monthly Notices of the Royal Astronomical Society*, 435(3):1928–1957, Sep 2013.

[52] A. A. Penzias and R. W. Wilson. A Measurement of Excess Antenna Temperature at 4080 Mc/s. *ApJ*, 142:419–421, Jul 1965.

[53] L. Perivolaropoulos and F. Skara. Challenges for λcdm: An update, 2021.

[54] S. Perlmutter, G. Aldering, G. Goldhaber, R. A. Knop, P. Nugent, P. G. Castro, S. Deustua, S. Fabbro, A. Goobar, D. E. Groom, I. M. Hook, A. G. Kim, M. Y. Kim, J. C. Lee, N. J. Nunes, R. Pain, C. R. Pennypacker, R. Quimby, C. Lidman, R. S. Ellis, M. Irwin, R. G. McMahon, P. Ruiz-Lapuente, N. Walton, B. Schaefer, B. J. Boyle, A. V. Filippenko, T. Matheson, A. S. Fruchter, N. Panagia, H. J. M. Newberg, W. J. Couch, and T. S. C. Project. Measurements of Ω and Λ from 42 High-Redshift Supernovae. *ApJ*, 517(2):565–586, Jun 1999.

[55] J. I. Phillips, M. C. Cooper, J. S. Bullock, and M. Boylan-Kolchin. Are rotating planes of satellite galaxies ubiquitous? *MNRAS*, 453(4):3839–3847, Nov. 2015.

[56] A. Pourtsidou, C. Skordis, and E. J. Copeland. Models of dark matter coupled to dark energy. *Physical Review D*, 88(8), Oct 2013.

[57] A. Pourtsidou and T. Tram. Reconciling cmb and structure growth measurements with dark energy interactions. *Physical Review D*, 94(4), Aug 2016.

[58] J. Rhee, R. Smith, H. Choi, S. K. Yi, Y. Jaffé, G. Candlish, and R. Sánchez-Jánssen. Phase-space Analysis in the Group and Cluster Environment: Time Since Infall and Tidal Mass Loss. *ApJ*, 843(2):128, July 2017.

[59] A. G. Riess, A. V. Filippenko, P. Challis, A. Clocchiatti, A. Diercks, P. M. Garnavich, R. L. Gilliland, C. J. Hogan, S. Jha, R. P. Kirshner, B. Leibundgut, M. M. Phillips, D. Reiss, B. P. Schmidt, R. A. Schommer, R. C. Smith, J. Spyromilio, C. Stubbs, N. B. Suntzeff, and J. Tonry. Observational Evidence from Supernovae for an Accelerating Universe and a Cosmological Constant. *AJ*, 116(3):1009–1038, Sep 1998.

[60] A. G. Riess, L. M. Macri, S. L. Hoffmann, D. Scolnic, S. Casertano, A. V. Filippenko, B. E. Tucker, M. J. Reid, D. O. Jones, J. M. Silverman, and et al. A 2.4 *The Astrophysical Journal*, 826(1):56, Jul 2016.

[61] V. Sahni and Y. Shtanov. Braneworld models of dark energy. *Journal of Cosmology and Astroparticle Physics*, 2003(11):014–014, Nov 2003.

[62] V. Salvatelli, N. Said, M. Bruni, A. Melchiorri, and D. Wands. Indications of a late-time interaction in the dark sector. *Physical Review Letters*, 113(18), Oct 2014.

[63] F. Simpson. Scattering of dark matter and dark energy. , 82(8):083505, Oct. 2010.

[64] C. Skordis, A. Pourtsidou, and E. Copeland. Parametrized post-friedmannian framework for interacting dark energy theories. *Physical Review D*, 91(8), Apr 2015.

[65] A. Smith, S. Cole, C. Baugh, Z. Zheng, R. Angulo, P. Norberg, and I. Zehavi. A lightcone catalogue from the millennium-xxl simulation. *Monthly Notices of the Royal Astronomical Society*, 470(4):4646–4661, Jun 2017.

[66] R. Splinter, A. Melott, S. Shandarin, and Y. Suto. Fundamental discreteness limitations of cosmological n-body clustering simulations. *The Astrophysical Journal*, 497, 06 1997.

[67] V. Springel, S. D. M. White, A. Jenkins, C. S. Frenk, N. Yoshida, L. Gao, J. Navarro, R. Thacker, D. Croton, J. Helly, J. A. Peacock, S. Cole, P. Thomas, H. Couchman, A. Evrard, J. Colberg, and F. Pearce. Simulations of the formation, evolution and clustering of galaxies and quasars. *Nature*, 435(7042):629–636, Jun 2005.

[68] R. Teyssier. Cosmological hydrodynamics with adaptive mesh refinement. A new high resolution code called RAMSES. *A&A*, 385:337–364, Apr. 2002.

[69] J. Tinker, A. V. Kravtsov, A. Klypin, K. Abazajian, M. Warren, G. Yepes, S. Gottlöber, and D. E. Holz. Toward a Halo Mass Function for Precision Cosmology: The Limits of Universality. *ApJ*, 688(2):709–728, Dec. 2008.

[70] A. Y. Toukmaji and J. Board. Ewald summation techniques in perspective: a survey. *Computer Physics Communications*, 95:73–92, 1996.

[71] S. Tsujikawa. Quintessence: a review. *Classical and Quantum Gravity*, 30(21):214003, Oct 2013.

[72] O. Valenzuela, G. Rhee, A. Klypin, F. Governato, G. Stinson, T. Quinn, and J. Wadsley. Is there evidence for flat cores in the halos of dwarf galaxies? the case of ngc 3109 and ngc 6822. *The Astrophysical Journal*, 657(2):773–789, Mar 2007.

[73] L. Verde, T. Treu, and A. G. Riess. Tensions between the early and late universe. *Nature Astronomy*, 3(10):891–895, Sep 2019.

[74] M. Vogelsberger, F. Marinacci, P. Torrey, and E. Puchwein. Cosmological simulations of galaxy formation, 2019.

[75] J. Väliviita, E. Majerotto, and R. Maartens. Large-scale instability in interacting dark energy and dark matter fluids. *Journal of Cosmology and Astroparticle Physics*, 2008(07):020, Jul 2008.

[76] B. Wang, E. Abdalla, F. Atrio-Barandela, and D. Pavón. Dark matter and dark energy interactions: theoretical challenges, cosmological implications and observational signatures. *Reports on Progress in Physics*, 79(9):096901, Aug 2016.

[77] R. H. Wechsler and J. L. Tinker. The connection between galaxies and their dark matter halos. *Annual Review of Astronomy and Astrophysics*, 56(1):435–487, Sep 2018.

[78] S. Weinberg. The cosmological constant problem. *Reviews of Modern Physics*, 61(1):1–23, Jan 1989.

[79] S. D. M. White and M. J. Rees. Core condensation in heavy halos: a two-stage theory for galaxy formation and clustering. *MNRAS*, 183:341–358, May 1978.

[80] J. Yoo and Y. Watanabe. Theoretical Models of Dark Energy. *International Journal of Modern Physics D*, 21(12):1230002, Dec. 2012.

[81] A. R. Zentner, A. V. Kravtsov, O. Y. Gnedin, and A. A. Klypin. The anisotropic distribution of galactic satellites. *The Astrophysical Journal*, 629(1):219–232, Aug 2005.

[82] F. Zwicky. Die Rotverschiebung von extragalaktischen Nebeln. *Helvetica Physica Acta*, 6:110–127, Jan 1933.